

Multi-Wavelength Observations of an Active Region Filament

Masterarbeit
in der Wissenschaftsdisziplin Physik

eingereicht an der
Mathematisch-Naturwissenschaftlichen Fakultät
der Universität Potsdam

Erstgutachter und Betreuer: apl. Prof. Dr. Carsten Denker
Zweitgutachter: apl. Prof. Dr. Gottfried Mann

Andrea Diercke

18. November 2016



Leibniz-Institut für Astrophysik Potsdam
An der Sternwarte 16
14482 Potsdam



Universität Potsdam
Institut für Physik und Astronomie
Karl-Liebknecht-Straße 24/25
14476 Potsdam-Golm

Table of Contents

Abstract	1
Zusammenfassung	3
1 Introduction	5
1.1 Solar Activity	7
1.2 Solar Atmosphere	9
1.3 Filaments	13
1.4 Two-Dimensional Spectroscopy	17
1.5 Limitation of Solar Images	19
2 Observation and Instruments	21
2.1 Dunn Solar Telescope	23
2.2 Data Set	29
3 Data Reduction and Methods	31
3.1 Data Reduction and Reconstruction of ROSA Images	33
3.2 Data Reduction of IBIS Images	38
3.3 Measuring Flows in Filaments	43
3.4 Error Estimation	45
4 Results	47
4.1 Motivation	49
4.2 Results from the ROSA Data Set	49
4.3 Results from the IBIS Data Set	57
5 Discussion	71
6 Conclusion and Outlook	75
Bibliography	77
Acknowledgments	85
Appendix A – List of Acronyms	87

Abstract

Solar filaments are fascinating objects which occur in many different shapes on the solar surface. These objects are clouds of dense cold plasma in the solar atmosphere. Due to absorption of photospheric radiation and the temperature difference between the filament and the surrounding plasma, filaments appear as dark structures on the solar disk. As erupting events they have influence on the technical society in which we live by damaging satellites, disturbing GPS signals or causing geomagnetically induced currents, which damage power grids. To understand the origin and causes of these space-weather events will help us to predict them. In this thesis, I will present a multi-wavelength study of an active region filament, located close to an axisymmetric sunspot.

To analyze the active region filament, I use data of the Dunn Solar Telescope (DST), which was operated in service mode. The DST provides observations with three different instruments, i.e, the camera system Rapid Oscillations in the Solar Atmosphere (ROSA), the Interferometric Bidimensional Spectrometer (IBIS), and the Facility Infrared Spectropolarimeter (FIRS). In the scope of this thesis we used the data of the first two instruments, ROSA and IBIS. The ROSA data contains images, which show different layers of the solar atmosphere. The photosphere is shown with G-band images, the upper photosphere and lower chromosphere is visible in the Ca II K line-core images, and the chromosphere is displayed in the H β images. In addition to ROSA images, IBIS contains spectroscopic data from H α and spectropolarimetric data from the near-infrared (NIR) Ca II λ 8542 Å line, which both display the chromosphere. Spectroscopic data contain spectral line scans and the spectropolarimetric data further contains information about the polarization of the light.

The active region filament is not a classical elongated filament but a clumpy filament. Examining the temporal evolution of the filament shows that the clumpy filament and an elongated part of the filament separate during observations. Furthermore, a third filament forms in the same location. All three filamentary structures possibly root in bright regions, which are typically associated with footpoints of the magnetic flux loops. The magnetic configuration will also be examined in the thesis.

I analyze both data sets revealing the dynamics of the active region filament. Therefore, we will calculate the horizontal and line-of-sight (LOS) velocities of the plasma. The imaging data of ROSA was subjected to Local Correlation Tracking (LCT), which calculates the cross-correlation between two consecutive images and yields localized displacement vectors, which can be averaged over the time-series and converted into velocity vectors representing the persistent horizontal flow field. The results show flows, which are typical for the respective atmospheric layer such as mesogranular motions in the photosphere or motions along the threads of the filament in the chromosphere. Using IBIS data I analyze LOS velocities from the spectral information with different methods. The results show the up- and down-streaming flows within the filament. Especially, towards the end of observations, down-streaming flows in the lower part of the filament increased to supersonic flow speeds.

Finally, I started with the analysis of the spectropolarimetric data of the NIR Ca II line. For this purpose, I inspected the Stokes V profiles, which contain information about the circular polarized light. To decrease the noise in the signal, I averaged all maps of the time-series. Quantitatively, I compared the resulting magnetogram with magnetograms of the Helioseismic and Magnetic Imager (HMI) onboard the Solar Dynamics Observatory (SDO) and with extreme ultra-violet images of the Atmospheric Imaging Assembly (AIA) onboard SDO. The comparison shows that the filamentary structures connect positive polarities in the upper half with the dominating negative polarity in the lower half of the FOV. The clumpy structure lies in lower heights than the other elongated filamentary structures and connects the positive polarity in the middle of the FOV with a strong negative polarity in the upper part of the region. Furthermore, the G-band bright points are located at the border of strong small scale flux elements and represent areas of strong magnetic field.

Zusammenfassung

Filamente auf der Sonne sind faszinierende Objekte, welche in vielen verschiedenen Formen auf der Sonnenoberfläche zu finden sind. Diese Objekte sind Wolken aus kühlem Plasma in der Sonnenatmosphäre. Aufgrund der Absorption photosphärischer Strahlung und dem Temperaturunterschied zwischen dem Plasma des Filaments und dem Plasma in der Umgebung, erscheinen Filamente auf der Sonnenoberfläche als dunkle Strukturen. Als Eruptionen haben sie Einfluss auf die technologische Gesellschaft in der wir leben, in dem sie Satelliten beschädigen, GPS Signale stören oder geomagnetische Stürme verursachen, welche wiederum elektrische Leitungen beschädigen können. Um diese Weltraumwetterereignisse vorherzusagen, müssen wir deren Ursprung und Ursachen verstehen. In der vorliegenden Arbeit präsentiere ich eine Studie eines Filaments in einem aktiven Gebiet in der Nähe eines achsensymmetrischen Sonnenflecks in verschiedenen Wellenlängen.

Um das Filament des aktiven Gebiets zu analysieren, nutze ich Daten vom Dunn Solar Telescope (DST), welches im Service-Modus betrieben wurde. Das DST ermöglicht Beobachtungen mit drei verschiedenen Instrumenten: dem Kamerasystem Rapid Oscillations in the Solar Atmosphere (ROSA), dem Interferometric Bidimensional Spectrometer (IBIS) und dem Facility Infrared Spectropolarimeter (FIRS). Im Rahmen dieser Arbeit werden die Daten der ersten beiden Instrumente ROSA und IBIS ausgewertet. Die ROSA Daten beinhalten Bilder, welche verschiedene Atmosphärenschichten der Sonne zeigen. Die Photosphäre wird in den G-Band Bildern gezeigt, die obere Photosphäre und untere Chromosphäre in den Bildern des Linienkerns der Ca II Linie und die Chromosphäre in den H β Bildern. Zusätzlich zu den ROSA Bildern, stellt IBIS spektroskopische Beobachtungen der Chromosphäre in H α und spektropolarimetrische Beobachtungen in der Ca II λ 8542 Å Linie im nahen Infrarot zur Verfügung. Die spektroskopischen Daten beinhalten Scans der Spektrallinie und die spektropolarimetrischen Daten enthalten zusätzlich noch Informationen über die Polarisation des Lichts.

Das untersuchte Filament hat keine klassische langgestreckte Form, sondern besitzt eine klumpige Struktur. Beim Betrachten der zeitlichen Entwicklung des Filaments zeigt sich, dass sich von der klumpigen Struktur der benachbarte langgestreckte Teil abspaltet. Weiterhin bildete sich eine dritte filamentartige Struktur. Alle drei Filamentstrukturen sind möglicherweise in hellen Bereichen in H α verankert, welche mit magnetischen Fußpunkten assoziiert werden. Die magnetische Konfiguration des Gebiets wird ebenfalls in der Arbeit untersucht.

Der Datensatz wird hinsichtlich der Dynamik des Filaments untersucht. Dazu werden die horizontalen Geschwindigkeiten, wie auch die Geschwindigkeit entlang der Sichtlinie bestimmt. Die Bilddaten von ROSA werden verwendet um die horizontalen Geschwindigkeiten im Filament zu berechnen, wozu Local Correlation Tracking (LCT) verwendet wird. Dieses Verfahren berechnet lokale Kreuzkorrelationen zwischen zwei aufeinander folgenden Bildern und gibt den Verschiebungsvektor an, welcher über die Zeitserie gemittelt ist und anschließend in Geschwindigkeitsvektoren umgewandelt wird, welche langlebige horizontale Strömungen widerspiegeln. Die Ergebnisse zeigen Strömungen, welche typisch für die jeweiligen Atmosphärenschichten sind, wie mesogranulare Bewegungen in der Photosphäre oder Bewegungen entlang der fadenförmigen Feinstruktur der Filamente in der Chromosphäre. Die IBIS-Daten werden verwendet, um Geschwindigkeiten entlang der Sichtlinie aus der Linienkernposition zu bestimmen. Die Ergebnisse zeigen auf- und absteigende Strömungen innerhalb des Filaments. Insbesondere am Ende der Zeitserie erkennt man starke, nach unten gerichtete Strömungen im unteren Teils des Filaments, wobei Geschwindigkeiten im Überschallbereich erreicht werden.

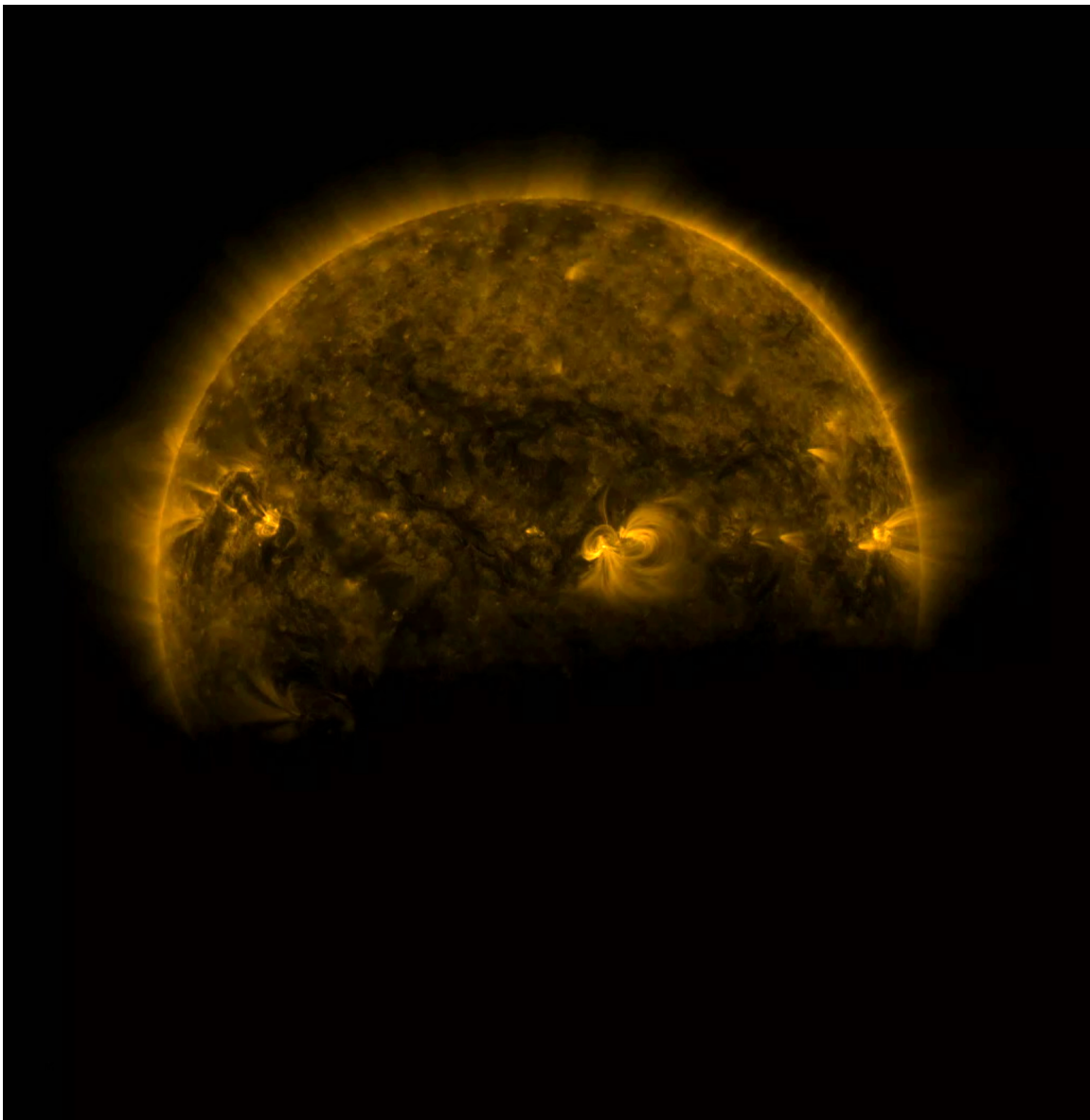
Im letzten Teil der Arbeit, untersuche ich die spektropolarimetrischen Daten der Ca II Linie im nahen Infrarot. Zu diesem Zweck nutze ich die Stokes-V Profile, welche Informationen über das zirkularpolarisierte Licht enthalten. Um das Rauschen in den Profilen zu verringern, werden alle Magnetfeldkarten der Zeitserie gemittelt. Wir vergleichen das gemittelte IBIS Magnetogramm mit den Magnetogrammen vom Helioseismic and Magnetic Imager (HMI) und mit den Bildern im extrem Ultraviolet des Atmospheric Imaging Assembly (AIA), die sich auf dem Solar Dynamics Observatory (SDO) befinden. Beim Vergleich der Daten sehen wir, dass die filamentartigen Strukturen die positiven Polaritäten in der oberen Hälfte des Bildausschnitts mit den negativen Polaritäten in der unteren Hälfte des Bildausschnitts verbinden. Weiterhin liegt die klumpige Filamentstruktur in einer geringeren Höhe und verbindet die positive Polarität in der Mitte des Bildfelds mit der negativen Polarität im oberen Bildabschnitt. Zum Schluss erkennen wir, dass die hellen Punkte im G-Band am Rand starker Magnetfeldstrukturen zu finden sind.

Chapter 1

Introduction

*Solar prominences are
beautiful and mysterious creatures
whose basic properties are far from understood*

Priest, van Ballegooijen, and Mackay (1996)



Front: Solar eclipse observed from Solar Dynamics Observatory. Due to the orbital path of the SDO satellite, the Earth blocks the Sun for about an hour on several days in August 2016. Still we can see filamentary structures and active regions on the Sun. In addition a prominence is recognizable at the eastern limb.¹

¹Pick of the Week: It's Eclipse Season for SDO, accessed 2016 September 5, available from <http://sdo.gsfc.nasa.gov/gallery/potw/item/733>

The Sun fascinates humanity since ancient times. Especially, solar eclipses were frightening experiences and the people have seen them as precursor of the Apocalypse. Still they are intriguing and mysterious phenomena. In later times, it was possible to understand the appearance of solar eclipses. They were used to gain new knowledge about the Sun and the universe. Different atmospheric layers were discovered, loops at the edge of the Sun were studied and even predictions from the general theory of relativity were proven thanks to a solar eclipse in 1919 (Seymour, 1976). Polar lights are impressive events as well, directly influenced by the solar wind. In 1859 Richard Carrington observed an enormous bright region in a sunspot group, which later turned out to be a white-light flare (Muller, 2014). Two days later the same event induced a geomagnetic storm, which caused polar lights in tropical regions as Havana or Hawaii. The storm even massively damaged the telegraph system in Europe and North America. Still, the Carrington event is one of the largest events ever observed on the Sun and experienced on Earth. The Sun is a very dynamic star, and also in 2012 a solar event of the same magnitude just missed the Earth. The Sun as the nearest and only star we can resolve spatially is still not completely understood and there are still many unsolved questions, which have to be answered by ongoing research.

1.1 Solar Activity

The Sun directly influences our daily life. Continuously the Sun expels the solar wind into the space towards the Earth containing charged particles. The solar wind interacts with Earth's magnetic field, which we can see on Earth in higher latitudes as aurorae. Explosive events can occur as well. We distinguish between two main types: flares and coronal mass ejections. A flare is a sudden release of energy in the form of electrons or ions accompanied with an increase in brightness. A coronal mass ejection (CME) releases an enormous amount of plasma into space with energies of up to $E = 10^{25}$ J stored in the mass and magnetic field of the precursor structure on the Sun (Stix, 2004). It is often shaped as a bubble. Both events can be ejected in any direction and can also hit the Earth whereby particles released by flares can reach the Earth after few hours and those of CMEs after several days. It can happen that a filament eruption already starts, when the magnetic loops are still tied in the photosphere. Reconnection processes of the magnetic field would then trigger a flare. Maybe also the Carrington event was caused in a similar way. On average coronagraphs, which are artificial eclipses blocking the high intensity of the solar surface, count three CMEs per day, and five or more during maximum activity. In the near-Earth environment we detect a CME in-situ only about once or twice a month (Lugaz, 2015). Nevertheless, these solar eruptions can cause damage to satellites, disturbances of the GPS signal, or geomagnetic storms. The influence on humans is relatively minor because Earth is shielded by its magnetic field, except for astronauts in space or flight personal on polar routes. It is important to understand the CME itself as well as the cause of these phenomena to validate their influence on Earth. Whether a CME can have larger effects on Earth also depends on the magnetic configuration of the plasma cloud approaching Earth. Thereby, reconnection can occur, when the solar magnetic field component $B_{z,\odot}$ of the plasma cloud is in the opposite direction to the magnetic field component of the Earth $B_{z,\oplus}$ (Lugaz, 2015). The reconnection occurs on the day-side of Earth's magnetosphere, whereby the solar wind particles can enter the magnetosphere. A current system through ionosphere and upper atmosphere is created, and as a result the newly open field lines cause aurorae. Strong solar magnetic field components from explosive events can also result in aurorae in lower latitude regions (Lugaz, 2015).

But where do solar eruptions originate? To answer this question, we first have to introduce solar activity in general. In 1844, S.H. Schwabe observed that every ten years the number of sunspots reaches a maximum and discovered the cyclic behavior of sunspot appearance (Schwabe cycle, Stix, 2004). Nowadays the average time between maxima of the sunspot cycle is corrected to 11 years. In 1919, G.E. Hale published his rules for the magnetic field in sunspots, which include that the magnetic orientation of the leading and following spots in sunspot groups is the same on each hemisphere over the 11-year cycle. Thereby, the bipolar groups in both hemispheres have opposite polarities and in the following cycle the magnetic orientation is reversed. Hale introduced with this rules the 22-year magnetic cycle of the Sun (Hale cycle, Stix, 2004), which includes the 11-year Schwabe cycle. The polarity of the hemispheres changes at around the time of the maximum. After a whole period of 22 years, the polarity is back to its initial configuration. Sunspots are an important measure for the activity of the Sun. They emerge at strong

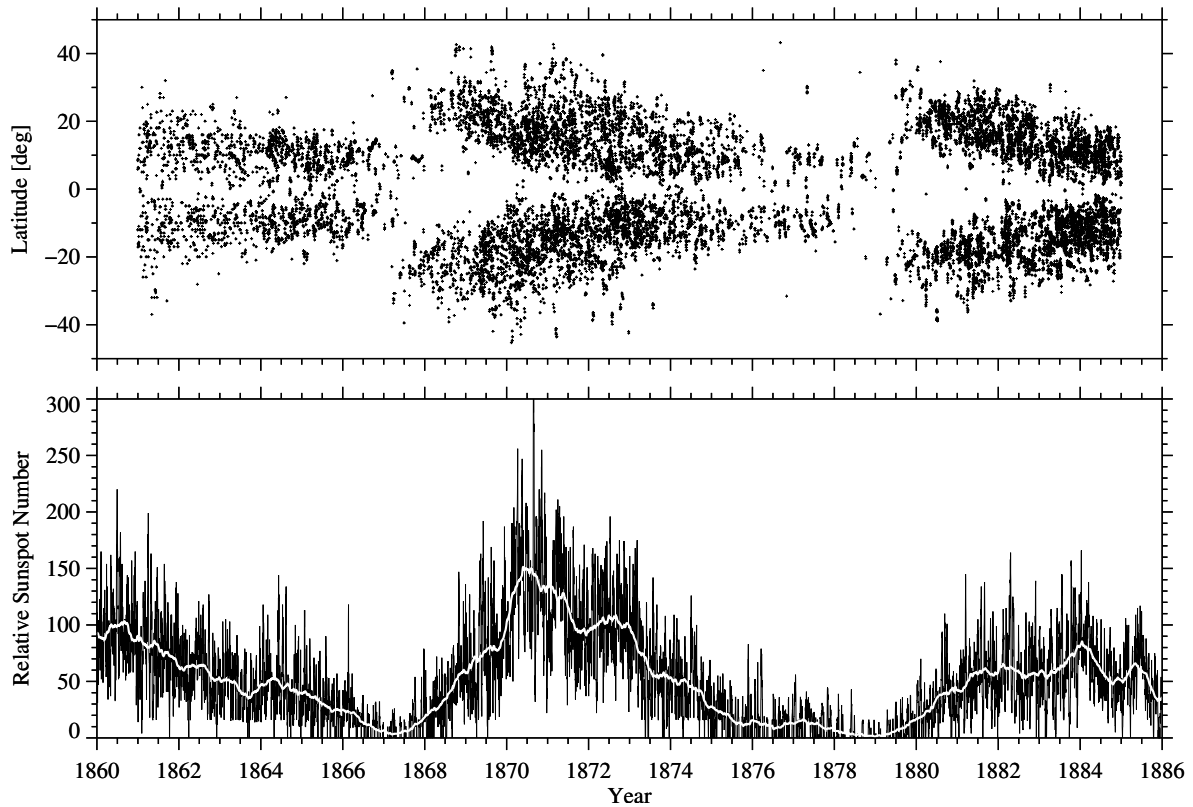


Figure 1.1: Butterfly diagram for the years 1861 to 1885 with observations of Gustav Spörer. (*top*) Sunspot appearance on the solar disk plotted over time. Spörer calculated the position of the sunspots and sunspot groups of the meridian passage. (*bottom*) SIDC daily relative sunspot numbers from 1860 to 1886 are depicted for the daily values (*black*) and a 200-day, sliding average (*white*), see Fig. 5 in [Diercke, Arlt, and Denker \(2015\)](#).

magnetic field concentrations. At the beginning of the 11-year cycle, during the minimum, sunspots and groups of sunspots appear at latitudes of around $\pm 40^\circ$ ([Cliver, 2014](#)). As the solar cycle progresses the sunspots form closer to the equator. At the beginning of the new cycle, there is a temporal overlap in which sunspots are present close to the equator and at $\pm 40^\circ$ latitude. The propagation towards the equator is described by Spörer’s law and the resulting diagram of sunspot positions plotted over time is named, due to its shape, butterfly diagram, see top panel of Fig. 1.1. With the increase of activity of the cycle the number of sunspots also increases. During the maximum a larger number of sunspots are present on the solar surface than in the minimum. The sunspot number is directly correlated to the solar activity which is shown in the bottom panel of Fig. 1.1.

Another cyclic behavior is known from prominences, which are plasma clouds in the chromosphere and corona with a loop-like structure observed at the limb of the Sun. We distinguish between quiescent, active region, and polar crown prominences, which will be introduced later in more detail (see Sect. 1.3). The prominences have two main branches of migration (see Fig. 1.2). The first branch, including quiescent and active region prominences, has a similar migration behavior as sunspots. They move from latitudes at around $\pm 35^\circ$ towards the equator, starting at around the minimum of activity. The second branch, containing polar crown prominences, shows a different behavior. They start to appear at latitudes at around $\pm 40^\circ$ near the maximum of activity and migrate towards the pole, which is also called ”dash to the poles” or ”rush to the poles” ([Cliver, 2014](#)). The behavior of the polar crown prominences can be explained with the appearance of new polarity flux when the magnetic field changes its polarity at around the maximum of the cycle. At the border of the new and old polarity flux, the polar crown prominences are formed, which is also the reason for the high stability of these kind of prominences. Polar crown prominences disappear around the next maximum, which signifies the reversal of the polarity at the poles.

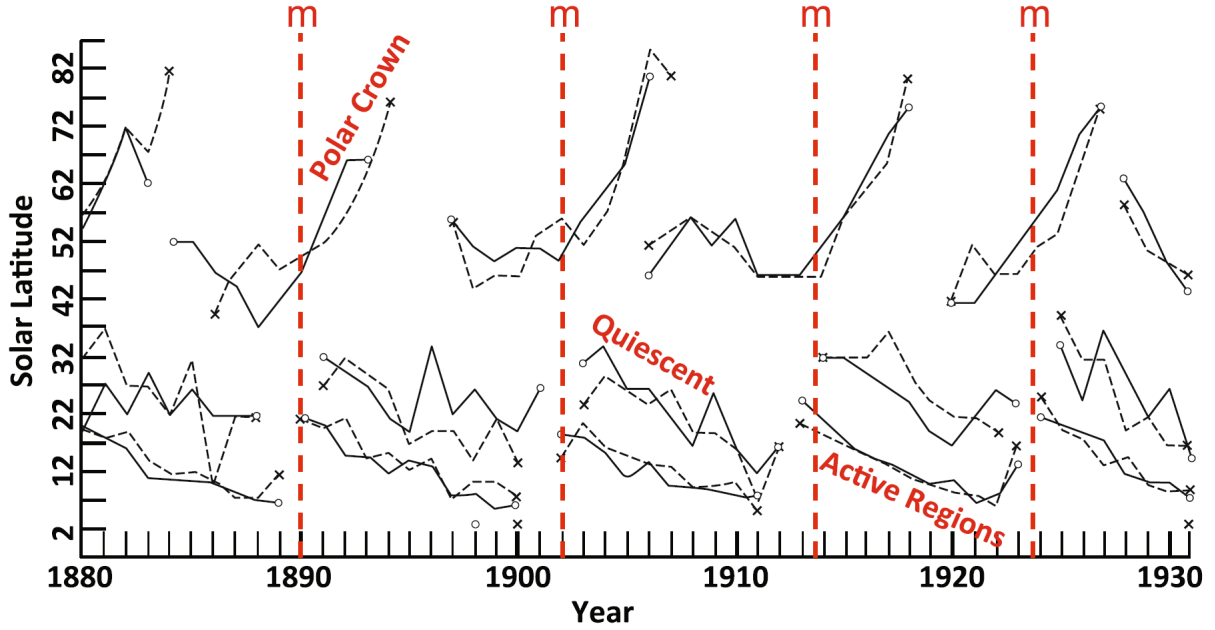


Figure 1.2: Migration of solar prominences from 1880 to 1930 for the southern and northern hemisphere. Here, the tracks for polar crown, quiescent, and active region prominences are shown. In addition, the solar minimum is shown (vertical red dashed line) (see Fig. 6 in Cliver, 2014).

1.2 Solar Atmosphere

When we observe the Sun, we can not look into its interior, but we can observe the surface and atmosphere of the Sun. To understand this we have to introduce the concept of optical depth τ_λ (Spruit, 2001)

$$\tau_\lambda = \int_{-\infty}^{z_p} a_\lambda(z) dz, \quad (1.1)$$

where $a_\lambda(z)$ is the absorption coefficient at a certain wavelength λ and z is a depth coordinate in the Sun. The probability that a photon can escape from the Sun without being absorbed or scattered is $e^{-\tau}$ (Spruit, 2001). In the deeper solar layers this probability is very small, because τ is large, so that direct observations are not possible. The photosphere is defined as the region, where most of the solar photons are emitted, with values for the optical depth of $\tau_\lambda = 0.1$ to $\tau_\lambda = 3$ (Spruit, 2001). Herewith the surface of the Sun is defined as the photosphere. During solar eclipses, also higher layers were discovered, i.e., the chromosphere and the corona. Nowadays we can observe these higher layers with filters from Earth or from space.

1.2.1 Photosphere

By observing the Sun in white-light we see a sharp edge as if all the light is coming from just one layer of the Sun (Spruit, 2001). This light originates in the photosphere, where almost all light is emitted. The photosphere is a narrow atmospheric layer only a few hundred kilometers in height. In observations of the entire disk (see left panel in Fig. 1.3), two main objects are visible on the photosphere: sunspots or pores and faculae regions. Sunspots or pores appear at locations of strong and dense magnetic fields, and they appear dark because they are cooler than the surrounding photospheric plasma. A sunspot has, unlike the much smaller pore, a penumbra surrounding the dark umbra (Stix, 2004; Weiss, 2001). The lifetime of a pore is approximately one day, whereas sunspots can remain for several days to weeks, in rare cases sunspot groups can remain on the Sun even for several rotation periods. As mentioned in Sect. 1.1, the number of sunspots is a reliable tracer of solar activity. Sunspots are known for several thousand years, because larger spots are visible with the naked eye. Later systematic sunspot observations were carried out, for example, by Gustav Spörer (see Fig. 1.1). The other objects are faculae regions, which are bright regions and can be observed especially good at the limb, because of their high contrasts. In the chromosphere faculae are called plage. Often they accompany groups of sunspots. Furthermore, the



Figure 1.3: The Sun in different atmospheric layers: (*left*) Continuum image of the photosphere² from the Helioseismic and Magnetic Imager (HMI, Schou *et al.*, 2012) on board the Solar Dynamics Observatory (SDO, Pesnell, Thompson, and Chamberlin, 2012), whereby limb-darkening is subtracted. (*middle*) The chromosphere observed in H α λ 6563 Å from the Kanzelhöhe Solar Observatory³. (*right*) The corona² observed in Fe IX λ 171 Å with the Atmospheric Imaging Assembly (AIA, Lemen *et al.*, 2012) on board SDO. The images are from 2013 January 20.

number of faculae is increased at high solar activity. Both, faculae and sunspots have influence on the solar irradiance, but because faculae regions are about 15 times larger than sunspots, the solar irradiance is increasing during high solar activity (Chapman, 2001). Observing the Sun in high resolution we see that the photosphere is composed of granules. The boundaries of granules form a polygonal pattern with bright elements which are separated by dark borders (Brandt, 2001). First they were described by Herschel (1801). Granules are very dynamic objects with a mean lifetime for a single granule of 6 min (Stix, 2004). They originate from hot gas in the convection zone which rises to the surface and cools down due to radiation. At the dark lanes surrounding granules the hot plasma sinks back into deeper layers. The width is varying between 150 km for fragments of granules up to 2500 km. The plasma moves in such granules with a horizontal and vertical velocity in the order of 2 km s^{-1} (Brandt, 2001). Averaging the granular horizontal flow patterns over about one hour, larger flow patterns become visible: the mesogranulation (Stein, 2001) with a diameter of about 5–10 Mm. An even larger pattern is the supergranulation with a diameter of about 20 Mm, which becomes visible in Dopplergrams (Simon, 2001).

At the boundary of granules we can sometimes observe bright points in high-resolution images, i.e., in the Fraunhofer G-band with a central wavelength of $\lambda_G = 4305.5 \text{ Å}$ (see Fig. 1.4). Bright points collected in strings are named filigrée (Muller, 2001). They are present in the quiet-Sun at borders of supergranular cells or in active regions, where they are related to faculae. Quiet-Sun refers to the regions on the Sun outside of active regions. In active regions bright points surround individual or ensembles of granules. Here, these rings have a diameter of $2\text{--}3''$. These bright points are strongly related to magnetic flux concentrations. Only in G-band it is possible to observe in the photosphere both, the convective motions of the continuum plasma and the magnetic flux (Schüssler *et al.*, 2003). But the question arises: Why are bright points bright? With simulations of the conditions in the photosphere observed in G-band, Steiner, Hauschildt, and Bruls (2001) and Schüssler *et al.* (2003) have found an answer. In the photosphere, there are CH molecules. The absorption lines of the CH molecules are weaker at the location of the flux tube due to higher temperature and the resulting depletion through molecular dissociation. As consequence, the continuum shines through the weakened CH spectral line and this locations appear brighter in the G-band images. At the same time other molecule lines and neutral metal lines contribute to this process. These bright points are thought to be the footpoints of magnetic loops which can extend up into the corona (Rimmele, 2004).

²SDO – Data, *AIA/HMI Browse Data*, accessed 2016 October 7, available from <http://sdo.gsfc.nasa.gov/data/aiahmi/>.

³Kanzelhöhe Solar Observatory – Synoptic Archives, *Synoptic Calendar*, accessed 2016 October 7, available from <http://cesar.kso.ac.at/>.

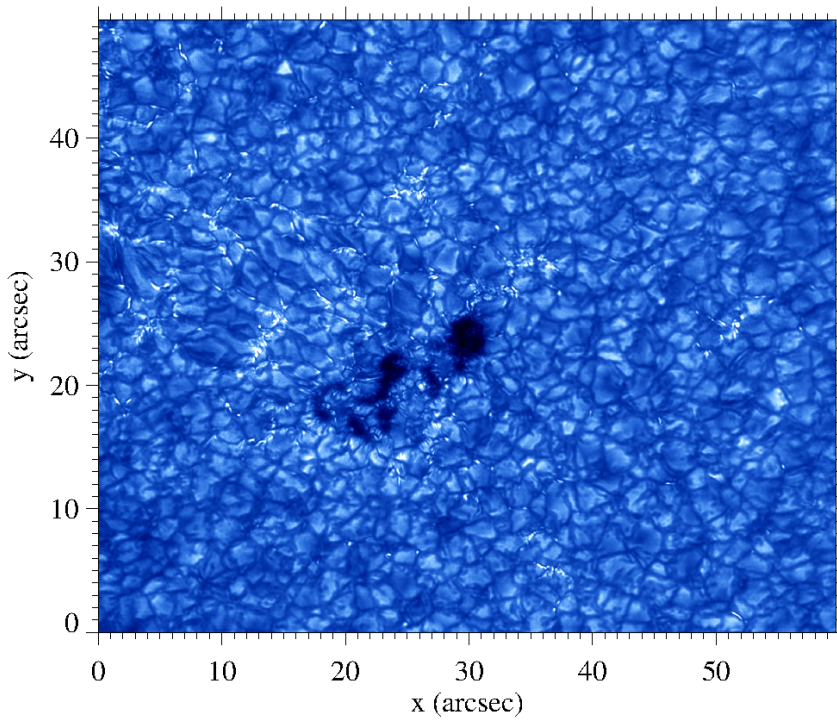


Figure 1.4: The photosphere observed in the Fraunhofer G-band with the High-resolution Fast Imager (HiFI) at GREGOR telescope on Tenerife, Spain, at 08:19 UT on 2016 April 11. An emerging sunspot is surrounded by photospheric granulation. At the borders of the granules we see bright points and filigree.

1.2.2 Chromosphere

The chromosphere was discovered during solar eclipses, where at the beginning and at the end of total eclipses a bright most colorful view is granted by the Sun. Therefore, the name chromosphere was given to this layer, which means colorful sphere. One of the strongest and most prominent lines which originates in the chromosphere is the $H\alpha$ line with a central wavelength at $\lambda_{H\alpha} = 6563 \text{ \AA}$ (see middle panel of Fig. 1.3 and Fig. 1.6). In high-resolution images we see that the chromosphere in $H\alpha$ has a very different appearance as the photosphere in continuum images. We see instead of the granular structures of the photosphere, a filamentary structure, the so-called fibrils, which cover the entire surface. Fibrils are aligned to the magnetic field (Spruit, 2001). In observations at the limb, we can observe other tiny chromospheric structures, i.e., the spicules. These are small, jet-like structures extending to a height of about 5 Mm to 10 Mm above the photosphere. At any time there are between 5000 and 30 000 spicules present on the disk. The lifetime of a single spicule is of about 5–10 min (Schmieder, 2001; Stix, 2004). They have an upward velocity of $10\text{--}25 \text{ km s}^{-1}$. Considering the number and the velocity of the spicules the upward mass flux is two orders higher than required for sustaining the solar wind (Stix, 2004). An open question remains, how the mass is transported back to the chromosphere. One controversially discussed theory is that spicules and mottles are the same phenomenon (Schmieder, 2001; Stix, 2004). Mottles are related to the chromospheric network. They are observed as small bushes in the wings of $H\alpha$. These structures, strongly related to the magnetic field, are rooted in the photosphere at the borders of supergranular cells. Therefore, they are also related to bright points and filigree in the photosphere. For mottles a downward flow at their base is observed, which potentially explains the downward motion of mass from spicules if they have the same nature which is still under discussion (Schmieder, 2001; Stix, 2004). The most prominent structures in the chromosphere are filaments (or bright prominences in limb observations), which are dark elongated structures clearly visible on $H\alpha$ filtergrams (see middle panel in Fig. 1.3) and Fig. 1.6). They appear with different length and in different locations on the Sun (see Sect. 1.3). Furthermore, the extension of the chromosphere is difficult to define (Stix, 2004). Some definitions refer to the region between the temperature minimum at $T = 4200 \text{ K}$ and a temperature of $T = 25\,000 \text{ K}$, which corresponds to a height of about 2 Mm. Others consider the height of spicules as a definition for the chromospheric height, because they still have chromospheric temperatures, which increases the height of the chromosphere to 5 Mm or 10 Mm.

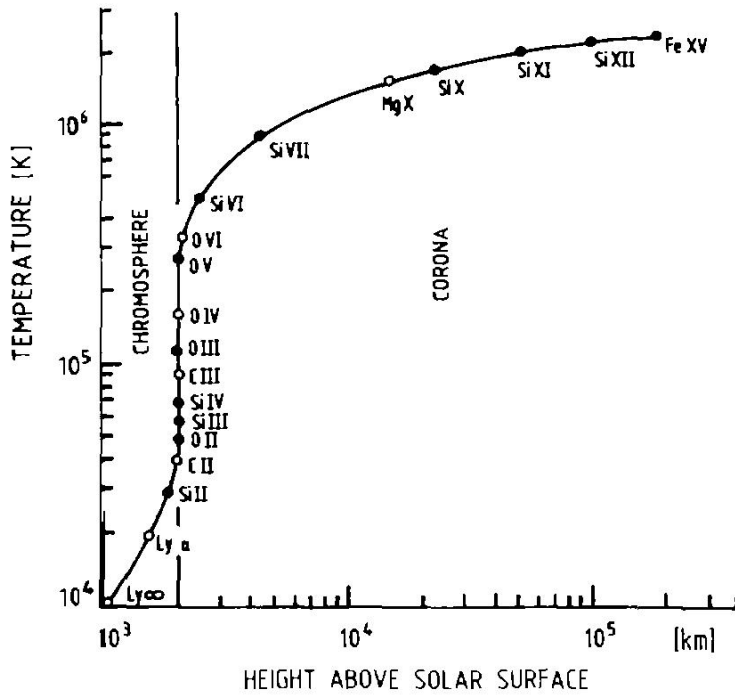


Figure 1.5: Solar temperature as a function of height above the solar surface for chromosphere and corona. Along the curve we see the formation temperature and height marked of some spectral lines (see Fig. 9.6 in [Stix, 2004](#)).

1.2.3 Transition Region and Corona

The transition region is a layer between chromosphere and corona defined by temperatures of 10^4 K to 10^6 K ([Stix, 2004](#)). [Zirker \(2002\)](#) describes the transition region more as an interface, which appears wherever there is a jump in temperature from chromospheric values to coronal temperature values larger than 10^6 K. Several spectral lines with wavelength between 500 \AA and 1600 \AA originate in this temperature regime (see Fig. 1.5). These wavelengths are only observable from space, because the Earth's atmosphere is absorbing the ultraviolet (UV) radiation of the Sun. Furthermore, we see in Fig. 1.5 a very steep rise of temperature between chromosphere and corona. One concept of explaining the coronal heating is the following. Unlike the heating of the chromosphere with acoustic waves, the corona is heated with magneto-hydrodynamic waves such as transverse Alfvén waves ([Stix, 2004](#)). They can be generated at the footpoints of flux tubes by fast photospheric motions or by magnetic instabilities due to magnetic field-line reconnections, i.e., nanoflares. These waves travel along magnetic field lines. The transverse nature of the waves means that there are no variations of density and pressure. Other theories concerning coronal heating propose electric currents.

As seen in Fig. 1.5, the temperature curve flattens in the corona with a temperature of about $T \approx 10^6$ K. At different wavelengths, the corona appears very different. First observations of the corona were made during solar eclipses, where we can observe the corona in white-light. In the visible wavelength regime we can observe the corona via emission lines of the forbidden transitions Fe X and Fe XI using a coronagraph together with a narrow-band filter. However, here only limb observations are possible. Nowadays, another way to observe the corona are space observations in the extreme UV (EUV) or in X-rays. More than 200 emission lines are identified between 13.7 \AA and 1058.7 \AA ([Stix, 2004](#)). They originate from highly ionized elements such as N VII, O VIII, or Fe XVII ([Stix, 2004](#)). In the right panel of Fig. 1.3 we see the solar corona in the spectral line of Fe IX $\lambda 171 \text{ \AA}$. The bright features originate from active regions or at the limb from coronal loops or prominences. The dark features belong to the relatively cool plasma of filaments. The Sun observed in X-rays shows other structures. Here, we see dark features, which can cover during the activity maximum the entire polar regions, i.e., the coronal holes ([Stix, 2004](#)). In the declining phase of the solar cycle coronal holes can reach all the way to the equator. They are part of the so-called open corona, because the magnetic field lines are open into interplanetary space. At these regions we look down to the photosphere ([Mullan, 2001](#)).

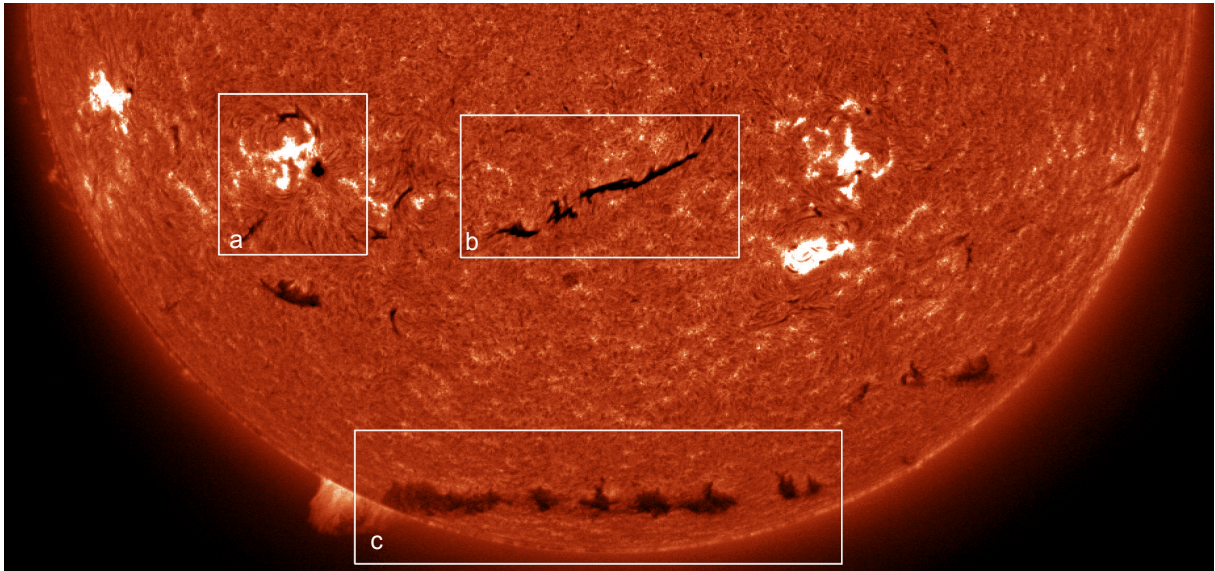


Figure 1.6: Observations in $H\alpha$ of the Sun with (a) active region with sunspot and active region filament, (b) an intermediate filament, and (c) a quiet-Sun polar crown filament on the southern hemisphere. The image was taken at the Big Bear Solar Observatory on 1999 June 12.⁴

1.3 Filaments

Filaments are the most common objects in the solar atmosphere (for reviews see [Martin, 1998a](#); [Mackay et al., 2010](#); [Parenti, 2014](#); [Engvold, 2015](#)). We see them on the solar disk in absorption as elongated, dark plasma clouds or as bright loops in emission at the solar limb, where they are called prominences. Physically both filaments and prominences, are the same objects. They are clouds containing cold plasma in the chromosphere and corona stabilized by the magnetic field. These objects form above the separation line between positive and negative magnetic fields, which is called the polarity inversion line (PIL, [Mackay et al., 2010](#)).

The region, which surrounds the PIL and where chromospheric fibrils are aligned to the PIL, is called the filament channel. The fibrils on each side of the channel are anti-parallel to each other, which is indicative of a strong magnetic shear ([Mackay, 2015](#)). The magnetic field lines are crossing the PIL from one polarity into the other forming an arcade system of closed loops ([Gaizauskas, 2001](#)). The magnetic field extends to some height of the corona. The filament is thought to be embedded in this magnetic field ([Mackay et al., 2010](#)). A filament always forms in a filament channel, but the filament channels exist also without filaments ([Parenti, 2014](#)). After a filament disappeared in a channel, new filaments can form in the same channel. Not all filament channels are clearly seen. The visibility depends on the strength of the magnetic field. Around weak magnetic fields, the fibrils are not aligned properly and the visibility is reduced. We can classify the filament channels by introducing the concept of chirality ([Martin, 1998b](#)). The channel is either dextral or sinistral depending on the direction of the fibrils viewed from the positive polarity side. If the fibrils emanate to the right/left direction, the channel is dextral/sinistral. Dextral/sinistral channels are mainly found on the northern/southern hemisphere.

Filaments are built up of three main parts: the spine, the barbs, and the extreme ends or legs ([Mackay et al., 2010](#)). The spine is the main body, the elongated black structure in absorption, containing cool plasma. The barbs are diverted from the spine and reaching down to the chromosphere. The spine is ending into the extreme ends, which are also reaching down to the chromosphere. The core temperature of the electron plasma in a filament is about $T_e = 6000\text{--}8000\text{ K}$, which is much lower than the 10^4 K to 10^6 K of the surrounding layers ([Engvold, 1998](#)). The electron density of filaments is $N_e = 10^{10} - 10^{11}\text{ cm}^{-3}$, which is much denser compared to the electron density of $N_e = 10^9\text{ cm}^{-3}$ of the corona ([Malherbe, 1989](#)).

As introduced in Sect. 1.1, we can differentiate three types of filaments ([Mackay et al., 2010](#); [Martin, 1998a](#)): active region, quiescent or quiet-Sun, and intermediate filaments (see Fig. 1.6). The quiet-Sun

⁴BBSO FTP Data Archive – 19990612, *Daily Images from Global $H\alpha$ Network*, accessed 2015 December 23, available from <http://www.bbsso.njit.edu/>

filaments can appear everywhere on the solar disk, whereby the active region filaments appear only near active regions in the activity belt. Intermediate filaments have typically parts resembling quiet-Sun filaments and other parts similar to active region filaments. They form close to decaying active regions or at the border between the weak unipolar background field and active regions. The characteristic values concerning length, height, or width lay between values for active region and quiet-Sun filaments. On one hand, the difference between the three kinds of filaments is not due to different physical properties, but due to different scale and activity of the underlying magnetic structure (Engvold, 2015). On the other hand, the formation mechanism of quiet-Sun and intermediate filaments differs compared to active region filaments (Mackay *et al.*, 2010).

1.3.1 Quiet-Sun Filaments

Quiet-Sun filaments are found at any location on the solar disk. Many quiet-Sun filaments form at the border between polar magnetic fields and the newly appearing magnetic field of opposite polarity at latitudes $\geq 50^\circ$ (Engvold, 2015). These filaments belong to the subcategory of polar crown filaments. Their filament channels can exist for many month to years and several filaments can form in these locations. In general, quiet-Sun filaments are more stable than active region filaments and live for several weeks, which is also supported by the weak magnetic field in which they develop. Recent studies with data from space telescopes, i.e., the Solar and Heliospheric Observatory (SoHO, Domingo, Fleck, and Poland, 1995) or the SDO, show that quiet-Sun filaments develop also at lower latitudes and reach into the activity belt ($\leq 40^\circ$), where they can be destabilized by nearby active regions (see e.g., Diercke, 2014). Quiet-Sun filaments have larger dimensions as active region filaments. Typically, they have a width of up to 5 Mm, reach heights of 30 Mm above the photosphere, and have a length of 50 Mm to 200 Mm, but also larger quiet-Sun filaments are reported with up to 1000 Mm (Engvold, 1998, 2015; Diercke, 2014). Quiet-Sun filaments have low magnetic field strength of 3–15 G (Mackay *et al.*, 2010). The dominating structure are barbs, and the filament spine is clearly formed out of individual threads (Engvold, 2015).

1.3.2 Active Region Filaments

Active region filaments appear close to sunspots in the sunspot latitude belt. They have a relatively thin spine and a small number of barbs. Because of the dynamic and active environment they are relatively short-lived with a lifetime of several hours up to a few days. In some cases, they end-up in eruptive events and in other cases they just fade away or split up into fragments. The number of active region filaments is closely related to the activity of the solar cycle (Engvold, 2015). The magnetic field is much stronger in active region filaments compared to quiet-Sun filaments and can reach values of up to 600–700 G (Kuckein *et al.*, 2009). Active region filaments are small with lengths of 10–100 Mm (Tandberg-Hanssen, 2001) and reach only heights of 10 Mm which is approximately the height of the spicule forest (Mackay *et al.*, 2010). The strong magnetic fields along the spine of the filaments support continuous mass motions in active region filaments. The disappearance of these filaments occurs either by increasing internal motions of up to 30 km s^{-1} , or by activation (Tandberg-Hanssen, 2001). In the latter case, different phenomena related to flares can occur. First, the spray, which are flare-associated ejections of plasma, can reach velocities of $500\text{--}1200 \text{ km s}^{-1}$ in a few minutes. Second, the surges, which are prominence eruptions shot out of active regions in a long straight or curved trajectory. The material falls back the same way and may trigger a new surge. They can reach heights of up to several megameter and reach velocities of several hundred km s^{-1} . The third phenomenon that leads to a vanishing of active region filaments are loop prominences and coronal rain. They are also referred to as post-flare loops because they appear in the late phase of flares. Here, reconnection happens and new loops are formed, whereby the new loops are formed in higher layers (up to 50 Mm above the photosphere) while the lower loops fade away (Tandberg-Hanssen, 2001).

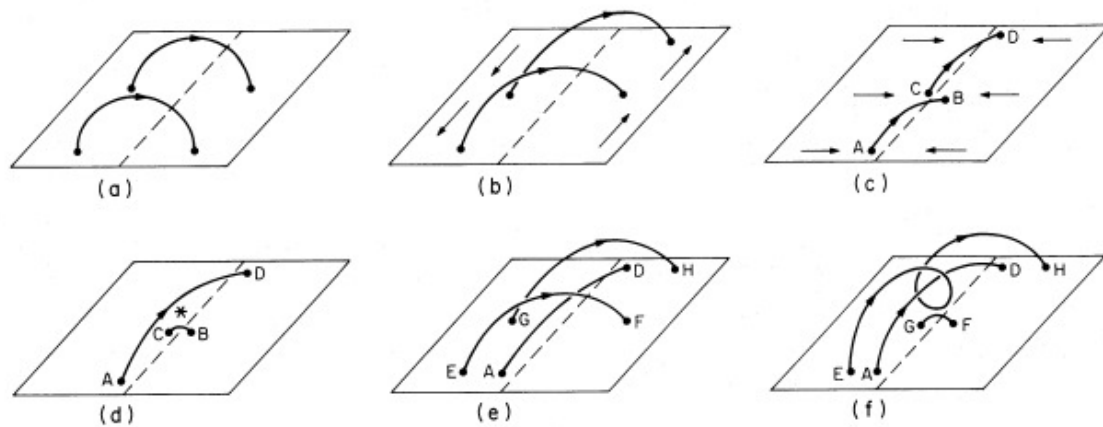


Figure 1.7: Formation of filaments according to the model of [van Ballegoijen and Martens \(1989\)](#). We see the photosphere connected by magnetic field lines. The dashed line denotes the PIL. (a) The initial potential field. (b) Adding shear flows on both sides of the PIL. (c) Adding converging flows, the magnetic footpoints are pushed toward the PIL. (d) Magnetic reconnection produces the shorter loop CB and the longer loop AD. (e) The loops EF and GH start with an initial potential field configuration, as seen in (a), and then shear flows start again. (f) After reconnection the loops EH and GF appear. The loop GF submerges below the photosphere. The loop EH wraps around the loop AD and forms a twisted field, which is called flux rope (see Fig. 1 in [van Ballegoijen and Martens, 1989](#)).

1.3.3 Formation of Filaments

Two questions are important to understand the formation of filaments: where and how do filaments form? To answer the first question [Tang \(1987\)](#) introduced two categories and [Mackay, Gaizauskas, and Yeates \(2008\)](#) extended them to four. The categories describe the magnetic configuration at the location where filaments form. The first category is called the Internal Bipole Region (IBR), where the filaments form above the PIL in a single bipole region. In the second category, the filaments form above the PIL between two separated magnetic bipoles, which is called an External Bipolar Region (EBR). The next category, the Internal/External Bipolar Region (I/EBR), describes filaments which lie above both, an internal PIL of a bipole and an external PIL which surrounds the bipole. The filaments, which form in flux configurations resulting from many independent flux emergences, belong to the last category. This category is named Diffuse Bipolar Region (DBR). In an extensive study including over 600 filaments [Mackay, Gaizauskas, and Yeates \(2008\)](#) categorized the filaments with respect to the above scheme and found that 92% of all filaments belong to categories involving multiple bipoles, whereby 62% belong to EBR, 17% to DBR, and 13% to I/EBR. The other 8% of the filaments are formed within single bipolar regions and belong to the category of IBR filaments. Furthermore, the number of EBR filaments is related to the 11-year solar cycle, whereby more filaments occur in the maximum. [Mackay \(2015\)](#) concludes that EBR filaments are strongly related to the amount of magnetic flux on the Sun, which rises in times of enhanced activity.

To answer the question how a filament is formed there are many theoretical model groups, which can be divided according to two basic assumptions: surface models and subsurface models ([Mackay, 2015](#)). Both models are subdivided into single bipole and multiple bipole models. We will present here one surface and one subsurface model. Basically, the subsurface mechanisms are summarized with subsurface motion, followed by magnetic subsurface reconnection, flux emergence in U-loops, and magnetic helicity. A detailed prominent surface model is described by [Low \(1994\)](#) and [Rust and Kumar \(1994\)](#). The authors start with a horizontal twisted magnetic flux tube in the convection zone, which emerges through the photosphere due to buoyancy up into the corona. Thereby, cool dense material from the photosphere is pulled within the tube into coronal heights. According to simulations, where buoyancy and magnetic buoyancy instabilities are considered, the axis of the flux tube does not reach coronal heights. Alternatively, coronal loops can form by reconnection of the emerging sheared field lines, which lie above the flux rope.

The surface models include the following mechanisms: differential rotation (shear flow), converging flows, magnetic reconnection in the atmosphere, flux emergence of the bipoles, magnetic helicity, and flux cancellation or diffusion. An early and prominent surface model describing the formation in a single bipolar region (see Fig. 1.7) was proposed by [van Ballegoijen and Martens \(1989\)](#). The authors start with

an initial condition of a potential field where the magnetic field lines connect the two polarities separated by the PIL (see dashed line in Fig. 1.7a). By adding shear flows due to differential rotation or other shear flows, the footpoints are moved in different directions (see Fig. 1.7b). Furthermore, converging flows are added to the model and the footpoints move toward the PIL (see Fig. 1.7c). The loops reconnect and the small loop CB and the long axial field line AD along the PIL arise (see Fig. 1.7d). The small loop submerges through the surface. The whole process is repeated, whereby a new loop EH is wrapped around loop AD (see Fig. 1.7e and f). This newly developed twisted field is called a flux rope. By repeating the process, the axis of the helical field rises. The cool plasma is trapped inside the helical field (van Ballegooijen and Martens, 1989). The possible processes of how the plasma is transported into the helical field are described in Sect. 1.3.4.

Observations indicate that most intermediate and quiet-Sun filaments form in magnetic configurations of multiple bipoles. No filament was observed so far forming during the emergence of flux, but later after convergence and cancellation of individual bipoles (Mackay, 2015). In conclusion, reconnection and cancellation of flux are the main mechanisms for the formation of large stable filaments. The formation of small-scale more unstable filaments in and around active regions differs. They are a result of flux rope emergence, which drags the photospheric plasma into coronal heights. After the flux rope emerges, magnetic reconnection occurs, and it may trigger the appearance of a second coronal flux rope. The reconnection during the submerging process may lift the cool dense material into the corona (Mackay, 2015). As a conclusion, we see that we have to distinguish between intermediate and quiet-Sun filaments as compared to active region filaments because of the different formation mechanisms.

1.3.4 Flows in Filaments

The detailed process how plasma is transported into the filaments spine is still an open question. Although there are different models giving possible explanations to the observational properties, there is no model explaining all processes. A sufficient model should explain the following processes among others: the mass motion in filaments of all ranges in time and space, as well as the highly dynamic plasma motions with velocities between $10 - 100 \text{ km s}^{-1}$ and the low temperatures of the plasma within the filament compared to the surrounding plasma. Furthermore, there are not only the large-scale structures, but also the small-scale structures such as threads and knots, which have to be explained in a comprehensive model. There are four main models, which shall be briefly introduced: injection, levitation, evaporation-condensation, and magneto-thermal convection (Karpen, 2015). In the injection model the photospheric or chromospheric mass is driven into the corona with visible upward jets or up-flows (Karpen, 2015). This is possible due to reconnection of flux cancellation as described in the model of van Ballegooijen and Martens (1989). The mass rises into the corona retaining its cool temperature. Only few observations of active region filaments show up-flows, which support this model. In quiet-Sun filaments such up-flows are not directly observed, yet. The levitation model on the other hand proposes that the cool plasma rises together with the magnetic field along the PIL (Karpen, 2015). Thereby, a necessary assumption is that the flux rope is highly twisted and carries the plasma with it by rising in higher atmospheric layers. These concave-upward formations have been observed for non-erupting filaments and fit to lower lying filaments of active regions, but not to quiet-Sun filaments. In the evaporation-condensation model, the plasma is heated at the footpoints, whereby the chromospheric plasma is evaporated, generating hot up-flows into the corona (Karpen, 2015). Here the plasma condenses and forms cool prominence threads. A thermal non-equilibrium condition at the footpoints is necessary, which does not fit to short active region filaments if the length is smaller than 80 Mm. In addition, observations of polar crown or hedgerow prominences with their vertical structures do not fit into this model. The last and most recent model is based on magneto-thermal convection (Karpen, 2015). The concept was introduced by Berger *et al.* (2011) based on observations of quiet-Sun prominences with SDO. The process starts with twisted magnetic flux, which emerges from subsurface regions into the chromosphere below a prominence, whereby a bubble forms (Karpen, 2015). The plasma in the bubble is heated by internal reconnection or Alfvén wave dissipation. Due to buoyancy, the bubble is carried up to coronal heights, where Rayleigh-Taylor instabilities (RTI, Müller, 2000) occur. RTI occur, when two fluids with different densities accelerated towards each other. The instability causes a turbulent transport mechanism, whereby hot plasma and magnetic flux is carried into the corona by plumes (Karpen, 2015). This process is supported by direct observations of bubbles

and plumes filled with hot plasma rising to coronal heights. It explains the formation and evolution of polar crown and hedgerow prominences.

Filaments are very dynamic objects, and we observe flows everywhere in the filament. In the spine the flows can appear in only one direction, but we observe also oppositely directed flows, the so-called counter-streaming flows, which were first observed by [Zirker, Engvold, and Martin \(1998\)](#). In $H\alpha$ the flows are of the order $10-20 \text{ km s}^{-1}$. In the transition region in $\text{He II } \lambda 304 \text{ \AA}$ also higher flows with horizontal velocities up to 75 km s^{-1} are observed ([Kucera, 2015](#)). In active region filaments, [Chae \(2003\)](#) reports horizontal forming velocities of up to 250 km s^{-1} in the UV and EUV and [Alexander et al. \(2013\)](#) observed horizontal flows along the spine of nearly 100 km s^{-1} . Furthermore, also in barbs we have flows, but here the flows are observed as swaying motions which are interpreted as oscillating material. Even in the main body oscillations with periods of less than one hour are observed ([Engvold, 1998](#)).

1.4 Two-Dimensional Spectroscopy

There are many different methods to observe the Sun and to gain new knowledge about our nearest star. The Sun is the only star which we can resolve spatially. We can use images of the whole disk or of a small region in high resolution for the analysis of different features. With the new fast-imaging cameras, as for instance the High-resolution Fast Imager (HiFI) operated by AIP at the GREGOR telescope ([Schmidt et al., 2012](#)) on Tenerife, Spain, observations with a high spatial and temporal resolution are possible. Furthermore, the solar spectrum is full of information which can be used for analysis of solar features. Each absorption line seen in the solar spectrum contains information about, i.e., the chemical composition, magnetic field, Doppler velocities of solar features, etc. The spectral lines are formed at different heights in the solar atmosphere, which means, that with the help of these spectral lines, we obtain more information about the different solar atmospheric layers (as described in Sect. 1.2). There are two typical methods to gather the spectral information of the Sun. The first is to scan a solar region with a long-slit spectrograph, where the information at each slit position can be used to create maps, e.g., intensity or velocity, of the observed region. The different parts of the maps are taken at different time steps making it difficult to track single structures on the Sun over extended periods of time ([Bendlin, 1993](#)). Examples for spectrographs are the GREGOR Infrared Spectrograph (GRIS, [Collados et al., 2012](#)) or the Facility Infrared Spectropolarimeter (FIRS, [Jaeggli et al., 2010](#)). In the second method, we take two-dimensional narrow-band images at different wavelength steps to reconstruct in the following the spectral line. The resolution of this two-dimensional spectroscopy in the form of interferometer is comparable to grating spectrographs ([Bendlin, 1993](#)). Examples for interferometers are the GREGOR Fabry-Pérot interferometer (GFPI, [Denker et al., 2010](#); [Puschmann et al., 2012](#)) or the Interferometric Bidimensional Spectrometer (IBIS, [Cavallini, 2006](#); [Reardon and Cavallini, 2008](#)). We will focus in the following on the description of two-dimensional spectroscopy, namely on the Fabry-Pérot interferometer.

The Fabry-Pérot interferometer uses multiple beam interference. A classical setup of a Fabry-Pérot interferometer (FPI) is shown in the left panel of Fig. 1.8. The main elements in the setup are the two parallel surfaces ([Zinth and Zinth, 2011](#)), which can be in vacuum to avoid influence on the light due to changes in the refractive index n_F between the plates. The light is coming from the source, in our case the Sun, to a lens L_1 to collimate the light beam. The light is then approaching the parallel plates. Here the light is reflected and transmitted at the parallel plates with a separation d and the reflection angle θ_F (see right panel of Fig. 1.8). The transmitted electro-magnetic waves interfere in the outgoing beam. Behind the interferometer the multiple beams pass through lens L_2 and are projected on the focal plane or a CCD camera, where the interference pattern is displayed or recorded. A more detailed description and discussion of the equations for transmission and reflection is given in [Stix \(2004\)](#) and [Zinth and Zinth \(2011\)](#). We assume an ideal interferometer without dispersion or absorption. For the transmission and reflection coefficients we define the amplitude transmission coefficient t outside the plates and t' inside the plates, as well as the amplitude reflection coefficient r outside and r' inside the medium of the plates. Thereby, $t \cdot t' = 1 - r^2$ and $r' = -r$. The optical path difference is given by

$$\Delta = 2 n_F d \cos \theta_F \quad (1.2)$$

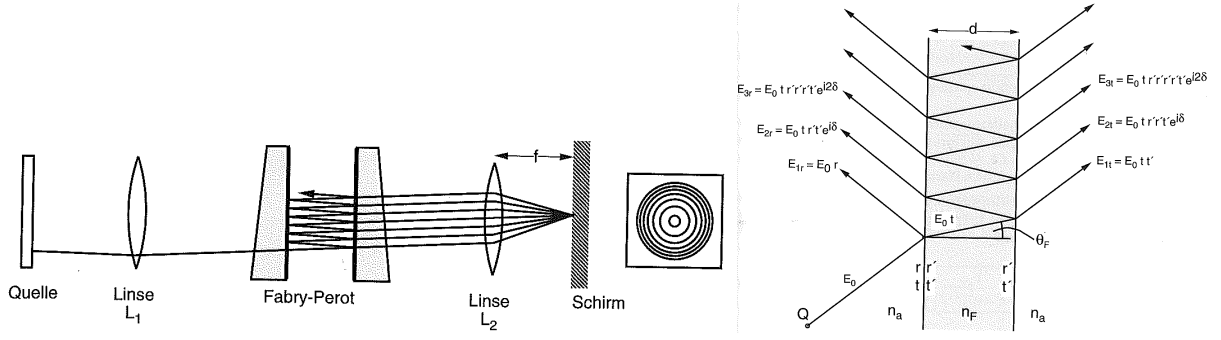


Figure 1.8: (left) Typical setup of a Fabry-Pérot interferometer. The light impinges from the source (*Quelle*) on lens L_1 , where it is collimated and passes through the interferometer with its two parallel plates. Afterwards, the multiple beams impinge on lens L_2 and are projected on the focal plane (*Schirm*) or a CCD camera (see Fig. 4.46 in Zinth and Zinth, 2011). (right) The path of the light of source Q through the interferometer with refractive index n_F and width d . The light wave is transmitted and reflected several times and multiple light beams are created. The wave has a reflection angle of θ_F . The reflective and transmitted electro-magnetic wave components are given (see Fig. 4.47 in Zinth and Zinth, 2011).

and the phase difference is

$$\delta = \frac{4\pi n_F d}{\lambda} \cos \theta_F. \quad (1.3)$$

First, we will calculate the reflected field component E_r , whereby all reflected parts are

$$E_r = E_{1r} + E_{2r} + E_{3r} + \dots \quad (1.4)$$

$$= E_0 r + E_0 t r' t' e^{i\delta} + E_0 t r' r' t' e^{2i\delta} + \dots, \quad (1.5)$$

with $|r'^2 e^{i\delta}| < 1$, this can be summed up as a geometrical series

$$E_r = E_0 \left(r + \frac{r' t t' e^{i\delta}}{1 - r'^2 e^{i\delta}} \right) \quad (1.6)$$

$$= E_0 \frac{r(1 - e^{i\delta})}{1 - r'^2 e^{i\delta}}, \quad (1.7)$$

where we used the already defined requirements for t , t' , r , and r' . The reflected intensity I_R of an FPI is then

$$I_R = I_0 \frac{2 r^2 (1 - \cos \delta)}{(1 + r^4) - 2 r^2 \cos \delta} \quad (1.8)$$

$$= I_0 \frac{F \sin^2(\delta/2)}{1 + F \sin^2(\delta/2)} \quad (1.9)$$

$$\text{with } F = \frac{4R}{(1-R)^2} \text{ and } R = r^2. \quad (1.10)$$

With our assumption, that we have no absorption, we have: $I_0 = I_R + I_T$, and the transmitted intensity I_T of an FPI is then:

$$I_T = I_0 \frac{1}{1 + F \sin^2(\delta/2)}. \quad (1.11)$$

This result was first obtained by G. B. Airy in 1831, so this function is called the Airy function. Now, we want to derive the position of the maxima for transmission, which is periodic. The maximum is obtained for $I_T = 1$, so when $\sin(\delta/2) = 0$. The m th maximum is at $\delta = 2 m \pi$, at wavelength

$$m\lambda = 2 n_F d \cos \theta_F. \quad (1.12)$$

Furthermore, we define the Free Spectral Range (FSR), which is the distance between two maxima

$$\text{FSR} = \frac{\lambda}{m} = \frac{\lambda^2}{2 n_F d \cos \theta_F}. \quad (1.13)$$

Close to the interference maxima the transmission curve I_T has a Lorentzian shape with a Full-Width-at-Half-Maximum (FWHM):

$$\Delta\delta = \frac{4}{\sqrt{F}}. \quad (1.14)$$

In addition, we define the finesse \mathcal{F} of the interferometer as the distance of neighboring maxima divided by the width of a maxima.

$$\mathcal{F} = \frac{2\pi \sqrt{F}}{4} = \frac{\pi\sqrt{R}}{(1-R)}. \quad (1.15)$$

Furthermore, the finesse can be defined as the ratio of the free spectral range and the spectral resolution $\Delta\lambda$, i.e., $\mathcal{F} = \text{FSR}/\Delta\lambda$. The resolution of a Fabry-Pérot interferometer is given with

$$\frac{\lambda}{\Delta\lambda} = \frac{\delta}{\Delta\delta} = \frac{4\pi n_F d \sqrt{F} \cos \theta_F}{\lambda \cdot 4} = m \frac{2\pi\sqrt{F}}{4} = m\mathcal{F}. \quad (1.16)$$

The resolution of the FPI directly depends on the finesse and the order number of the maximum. This interferometer is capable to achieve a very high spectral resolution.

The problem of an FPI is its small FSR. Therefore, a typical solution is to use the FPI not as one instrument but to have two or more FPIs in a row. With a series of FPIs it is important to achieve a high parallelism of the two etalons, which is technically very challenging. Furthermore, a prefilter is used to select a certain spectral range for analysis. In the end, it is possible to obtain two-dimensional images of the Sun at different wavelength positions with a high spatial, spectral, and temporal resolution. The concept of FPIs is also implemented in interference filters. These interference filters have a static separation d . We will have a more detailed look at interference filters in Sect. 2.1.2.

1.5 Limitation of Solar Images

We are able to observe the Sun with high spectral, spatial, and temporal resolution. Still, there are some limitations in the quality of the observed images mainly because of Earth's atmosphere and the instruments themselves. Compared to other stars, the radiation flux from the Sun is intense so that the number of photons is in general no problem for solar observations, but by observing objects, which are much darker than the surrounding quiet-Sun, i.e., umbra of a sunspot, the core of a strong spectral line, or both, the intensity decreases by an order of magnitude. In these cases, larger apertures are required, which collect even more photons. Another limitation regarding the image quality is Earth's turbulent atmosphere (Stix, 2004). The fluctuation of the refractive index and the resulting degradation of the images is called seeing. For the reflective index n one has

$$n - 1 = 2.79 \times 10^{-4} \frac{P/P_0}{T/T_0}, \quad (1.17)$$

where the pressure $P_0 = 1$ bar and the temperature $T_0 = 273$ K. The pressure variations, mainly associated with the wind, are nearly at equilibrium and are not effecting the atmospheric turbulence (Bely, 2003). Temperature changes are the main driver of turbulence. In solar physics the heating of the ground around the telescope building significantly effects the seeing of the images. A method to escape ground heating is to place the mirrors of the telescope on top of a tower. Other methods to reduce these effects are the evacuation of the telescope's tube. But still, seeing effects the images. Regarding the effects on the images, we divide between three main effects on the images: blurring, image motion, and image distortion (Stix, 2004). An image is blurred when there are defocused parts in the image caused by variations in the refraction index. The image motions refer to the movement of the whole image but the image is still sharp. If the image is distorted, parts of the image are moved in respect to other parts. In general, there is a combination of these effects. Effects of the seeing can be removed with image reconstruction methods, which will be introduced in the Sect. 3.1.2.

Chapter 2

Observation and Instruments



Front: Dunn Solar Telescope at Sacramento Peak Observatory.¹

¹Sunset over the Dunn Solar Telescope in Sunspot, NM. Part of the National Solar Observatory at Sacramento Peak, accessed 2016 April 12, available from commons.wikimedia.org

2.1 Dunn Solar Telescope

This thesis is based on data from the Dunn Solar Telescope (DST, [Bhatnagar and Livingston, 2005](#)). This telescope is situated in the Sacramento Peak Mountains at an altitude of 2800 m above sea level and belongs to the National Solar Observatory in Sunspot, New Mexico, USA. The DST is a vacuum tower telescope which was built in 1969. It has a total length of about 109 m, whereby 68 m are below ground level. First, the solar light impinges on the entrance window with a diameter of 0.76 m. Because it is placed at a height of 41 m, image distortion caused by ground turbulence are reduced. Furthermore, the entire light path behind the entrance window is evacuated (see Fig. 2.1). Afterwards, the light is reflected towards two plane mirrors with diameters of 1.1 m. They are mounted in a turret, which is a special alt-azimuth arrangement and minimizes local turbulence ([Stix, 2004](#)). The mirrors guide the light into the vertical vacuum tank with a diameter of 1.2 m. At the end of the tank, another mirror with a diameter of 1.6 m reflects the light back into the observing room. In this 12-meter diameter room the light is splitted and transferred into various instruments. Here, the image of the Sun has a diameter of 0.51 m. The adaptive optics (AO) achieves a spatial resolution approaching the telescope's diffraction limit ([Bhatnagar and Livingston, 2005](#); [Rimmele, 2004](#); [Rimmele and Marino, 2011](#)).

Three of the instruments at DST can be used in the service mode, which means, that the observations are performed by the local staff of the observatory. The observations are selected depending on the science case of the submitted proposals and the prevailing observing conditions, like seeing and activity of the Sun. We have data from three service mode campaigns at DST from three different instruments: Rapid Oscillations in the Solar Atmosphere (ROSA, [Jess et al., 2010](#)), Facility Infrared Spectropolarimeter (FIRS, [Jaeggli et al., 2010](#)), and Interferometric Bidimensional Spectropolarimeter (IBIS, [Cavallini, 2006](#); [Reardon and Cavallini, 2008](#)). With these three instruments we have access to the data of one imager in different spectral ranges and two spectropolarimeters. In the following I will concentrate on the data reduction and analysis of the data from ROSA and IBIS of the first service mode campaign on 2013 January 20. Therefore, we will introduce these two instruments and the reduction of the data. The polarimeter of FIRS incurred some problems on this day so that it was not modulating correctly. In principle, these data can still be used in spectroscopic mode but this will require a major modification of the FIRS data pipeline. This was not possible given the time frame for a master thesis but will be performed for a forthcoming peer-reviewed article.

2.1.1 Adaptive Optic System at the Dunn Solar Telescope

Adaptive optics (AO, [Bely, 2003](#)) systems were developed to correct the high-frequency wavefront disturbances which are evoked by Earth's atmospheric turbulence. In particular, in solar physics this is a very challenging task as compared to night-time observations. During daytime the heating of the ground which causes near-ground turbulence layers, is much greater than during night time observations. Furthermore, the seeing is more time varying. Solar AO systems have to lock on solar features such as sunspots, or pores, but also on low contrast and fast time-varying objects such as solar granulation ([Rimmele, 2004](#)). In general, AO is a necessary tool to achieve high spatial resolution of $0''.1$ or better to

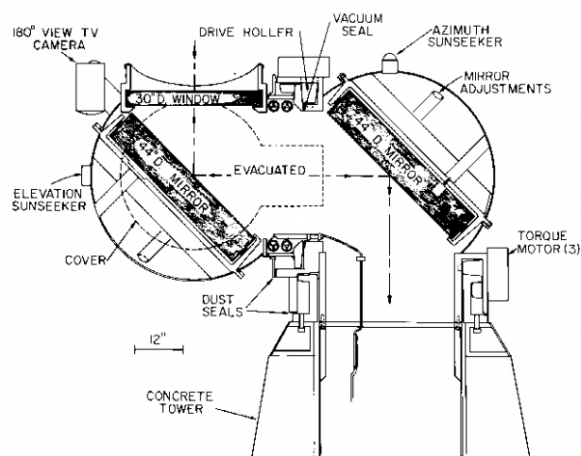


Figure 2.1: Schematic view on the entrance window and the evacuated two-mirror system in the turret of DST. The light is reflected into the telescope's evacuated tube.²

²Richard B. Dunn Solar Telescope – Tower Window, accessed 2016 Oktober 16, available from nsosp.nso.edu

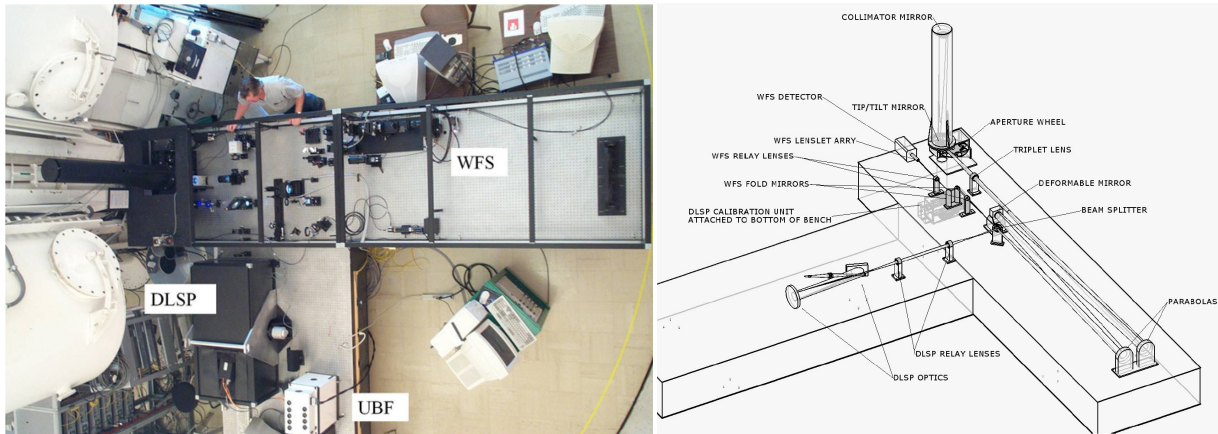


Figure 2.2: (left): AO system at the DST (see Fig. 16 in [Rimmele and Marino, 2011](#)). (right): Optical design of the AO system showing the light path, the tip-tilt mirror, the deformable mirror, the collimator and camera parabolas, and the wavefront sensor (see Fig. 7 in [Rimmele et al., 2003](#)).

study and understand small-scale solar structures. With AO systems, a diffraction-limited resolution can be achieved.

The first AO system with a 19-element segmented mirror and a Shack-Hartmann wavefront sensor from Lockheed was tested at the DST. Since 2004, the DST has two High-Order Adaptive Optics (HOAO, [Rimmele, 2004](#)) systems, developed by the National Solar Observatory (NSO) and the New Jersey Institute of Technology (NJIT). The system is used during medium seeing conditions to increase the image quality. Due to the telescope design, an integration of the AO system into the telescopes optics is not possible. The AO system had to be inserted between prime focus and the instruments. At DST there are two benches for instruments, thus two AO systems are necessary. One bench hosts the permanent instrument setup, and the other bench is used for experimental setups as well as for temporal used instruments. The light enters the HOAO system directly after the primary focus through a collimator mirror in the vertical direction (see Fig. 2.2). On the 30 mm tip-tilt mirror a pupil image is formed. The mount of the tip-tilt mirror at an angle of 45° allows the light to be guided into the horizontal axis continuing its path to one of the two parabolas serving as a collimator where the light is directed onto the Deformable Mirror (DM). At the DM the light is reflected to the second parabolic mirror that again focuses the light beam. From their the light passes a cube beam splitter, which transmits 5% of the light to the wavefront sensor, the rest is guided to the scientific instruments. Another 5% of the light is splitted by a second beam splitter for a video camera, which is used for visual performance control and selection of a target. The Shack-Hartmann Wavefront Sensor (SHWFS) contains 76 subaperture images with selectable Regions-Of-Interests (ROIs) between 16×16 and 20×20 pixels ([Rimmele, 2004](#)). The more pixels the larger the noise, here the photon noise in the subaperture images is about 0.5%. Just a factor of two to four below the signal of solar granulation. The SHWFS is connected to a high frame-rate CMOS camera, which is custom-built for a wavefront sensor. The camera has a Photobit Inc. PB-MV13 CMOS sensor with a pixel size of 1024×1024 pixels. The relatively high read noise of $60 e^-$ is insignificant compared to the shot noise of the wavefront sensor. The camera takes $2500 \text{ frames s}^{-1}$ for a ROI of 200×200 pixels, which is sufficiently large to cover all apertures of the wavefront sensor. The 76 subapertures of the wavefront sensor are processed by 40 Digital Signal Processors (DSPs, [Rimmele, 2004](#)). This system is sensing and reconstructing the wavefront, whereby correlation functions for two subapertures are computed per DSP unit. The units are organized in clusters of four. Here, the read-time for 200×200 pixels is $400 \mu\text{s}$. Including updating the voltage after the last pixel received by the DSP, the time is $650 \mu\text{s}$. In the DSP units, the real-time processing includes dark- and flat-field correction, cross-correlation of the two subapertures and a randomly chosen reference subaperture, calculating the shift in x - and y -direction and sending the displacement vectors to the deformable mirror ([Rimmele and Marino, 2011](#)). This mirror is composed of 97 subapertures manufactured by Xinetics. The mirror can be flatten to $1/50^{\text{th}}$ of a wave at 6280 \AA . Until today the DST provides very high resolution solar images thanks to the AO system ([Bhatnagar and Livingston, 2005](#)). Nevertheless, the spatial and temporal bandwidth of the system is limited. Therefore, post-processing of the images is required.

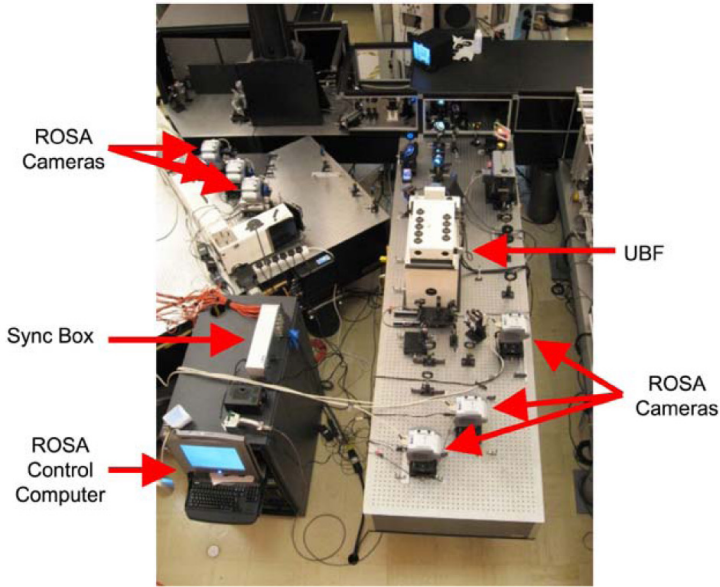


Figure 2.3: ROSA instrument at the DST. The two optical benches have three cameras each, the Sync-Box, which triggers all cameras, and the computer controlling the instrument, as well as the Universal Birefringence Filter (UBF). This image was taken during the commissioning run in August 2008. Three cameras are observing in the red spectral range and three in the blue one (see Fig. 1 in [Jess et al., 2010](#)).

2.1.2 The Camera System Rapid Oscillations in the Solar Atmosphere

First, we will introduce the instrument Rapid Oscillations in the Solar Atmosphere (ROSA, [Jess et al., 2010](#)), which is a camera system with six synchronized high-speed cameras (see Fig. 2.3). We can observe high-resolution solar images in six different wavelength at the same time with this instrument. It is built to study oscillations in the solar atmosphere in high-temporal resolution. The CCD camera takes up to 30 images per second. Each of the Andor iXon+ DU-885K-VP cameras has 1004×1002 pixels and is cooled down to 100 K below room temperature with a Peltier cooling element. This lowers and stabilizes the thermal current, i.e., the dark current. Each pixel on the CCD chip has a maximum capacity of charged particles, the full well capacity. In the case of the Andor cameras, the full well capacity is $40\,000\ e^-$. The electrons in the CCD have to be converted into digital signals, which are measured in the analog-to-digital unit (ADU). These cameras have a 16-bit analog-to-digital (A/D) converter, which corresponds to a maximum pixel value of $(2^{16} - 1) = 65536$ ADU ([Norton and Cooper, 2004](#); [Howell, 2006](#)). The pixel size of the cameras is $8\ \mu\text{m} \times 8\ \mu\text{m}$. Furthermore, the read-out-noise of the camera is only $15\ e^- \text{ s}^{-1} \text{ pixel}^{-1}$. With its high frame rate of $30\ \text{frames s}^{-1}$ we record in one hour 1.3 TB data if all six cameras operate at the same time. The images are stored in the Flexible Image Transport System (FITS, [Hanisch et al., 2001](#); [Wells, Greisen, and Harten, 1981](#)) format. Each FITS file contains 256 individual images and the corresponding headers. In the header all necessary information concerning the observation are stored, e.g., date and time of observations, frame rate, exposure time, and size of the image. All six cameras cover a spectral range between $2500\ \text{\AA}$ and $11\,000\ \text{\AA}$, including the visible spectral range but also parts of the ultraviolet and infrared. The highest quantum efficiency of 65% is obtained at $6000\ \text{\AA}$, in the red part of the spectrum.

Filters are an important part of solar observations. With their help, different layers of the solar atmosphere become visible. Two types of filters will be introduced, which are used at the ROSA camera system: Lyot filters and interference filters. We will start with the description of Lyot filters, which are composed of elements with two polarizer and a birefringent crystal with a width of d in the middle ([Stix, 2004](#)). An entering light wave passes through the first polarizer and is linearly polarized. The axis of the crystal is rotated by 45° compared to the axis of the polarizer. The birefringent crystal splits the incoming light wave into an ordinary and extraordinary ray. The ordinary ray with a velocity of $v_o = c/n_o$ is perpendicular to the optical axis and the extraordinary ray with a velocity of $v_e = c/n_e$ is parallel to the optical axis. After passing through the crystal, both rays have a phase difference of $\delta = 2\pi d(n_o - n_e)/\lambda$ with the wavelength in vacuum λ and the difference between ordinary and extraordinary wave $J = n_o - n_e$, which is called the birefringence of the crystal. The superposition of both polarized waves (ordinary and extraordinary) results in general in an elliptically polarized wave ([Demtröder, 2013](#)). A phase difference of $\delta = 2\pi m$ gives a wave, which is linearly polarized with the same direction as the incoming wave. Also for $\delta = (2m + 1)\pi$ and an angle of $\alpha = 45^\circ$ to the optical axis, the wave is linearly polarized, but perpendicular

Table 2.1: The different filters of ROSA with information regarding the central wavelength, the width of the filter, and the atmospheric layer (adapted from Tab. 2 in [Jess et al., 2010](#)).

Filter name	Central Wavelength	Filter Bandpass	Atmospheric Layer
G-Band	4305.5 Å	9.2 Å	photosphere
Ca II K line core	3933.7 Å	1.0 Å	upper photosphere/lower chromosphere
UBF (H β)	4861.3 Å [†]	0.2 Å	chromosphere*

[†][Moore et al. \(1966\)](#)

*[Bray and Loughhead \(1974\)](#)

to the incoming wave. The second polarizer will filter out this wave, because it only transmits parts which are parallel to its own direction. Often, Lyot filters are composed of several sequences of polarizer and crystals ([Stix, 2004](#)). Thereby, the width d_n of the n -th crystal is increased by $d_n = 2^{n-1}d$. Thus, the incoming light wave is filtered depending on the wavelength and we can select the required wavelength in a narrow range.

Another possibility to restrict the spectral range is to use an interference filter ([Hecht, 1998](#); [Zinth and Zinth, 2011](#); [Demtröder, 2013](#)). These are spectral filters are comprised of two plane-parallel plates separated by a distance d with a high reflectivity. If the plates are equidistant, they are called etalons. If the distance is variable they are called Fabry-Pérot interferometers (see Sect. 1.4). Between the plates of the etalon, there is often a glass plate or a dielectric material. The plates itself have a silver coating. The principal is that parts of the incoming wave are either reflected or transmitted. Furthermore, we have inference at thin films which causes a wavelength dependent destructive and constructive interference. This enables the system to filter out certain wavelengths. The width of such a pass band depends on the finesse, see Eq. (1.15), thus on the reflectivity of the coating.

In Fig. 2.3 we show the setup of the ROSA camera system during the commissioning run in August 2008 ([Jess et al., 2010](#)). The system is assembled on two optical benches with three CCD cameras each. The benches observe in different wavelength ranges: the one bench in the blue spectral range and the other bench in the red spectral range. Therefore, they employ different filters. For the blue spectral range there are a Lyot filter from Halle and interference filters from Oriel. The filters cover the Ca II K line (3933.7 Å), the blue continua (4170 Å and 3501 Å), and the photosphere in the Fraunhofer G-band (4305.5 Å).

On the other bench, there is a Zeiss Universal Birefringence Filter (UBF, [Bonaccini et al., 1989](#)), which is suitable for observing in different wavelength. This filter is a Lyot filter in combination with a achromatic quarterwave plate in front of the polarizer. Both are birefringent crystals. The quarterwave plate is rotated by 45° with respect to the optical axis. By rotating the polarizer by an angle α , the intensity of the linearly polarized wave is dependent on the wavelength λ . The range across which the quarterwave plate is achromatic decides about the wavelength range of the filter. The UBF filter has a wavelength range of 4100–7000 Å ([Beckers, Dickson, and Joyce, 1975](#)), with best results in the red range of the spectrum. This filter is often used to observe the chromospheric H α line at 6562.8 Å, but it is also employed to obtain magnetograms using the magnetically sensitive spectral line Fe I at λ 6302.5 Å.

2.1.3 Interferometric BIdimensional Spectrometer

Moved in June 2003 to the DST, the Interferometric BIdimensional Spectrometer (IBIS, [Cavallini, 2006](#); [Reardon and Cavallini, 2008](#)) is producing monochromatic images with high spectral, spatial, and temporal resolution. The instrument is composed of two Fabry-Pérot interferometers in axial-mode and classical mount (see Fig. 2.5). There are two main factors, which decide about the spatial resolution: The the diameter of the telescope entrance pupil and the atmospheric seeing. With the IBIS instrument, we achieve a spatial resolution of about $0''.2$. The spectral resolving power is between 200 000 and 270 000. The high spectral resolution is comparable to those of grating spectrographs. The effective exposure time lies between 32 ms and 50 ms. Thereby, the readout takes approximately 300 ms at 5 MHz and the storing takes roughly 30 ms. In total we get a temporal resolution of about 2.5 frames s⁻¹ ([Cavallini, 2006](#)).

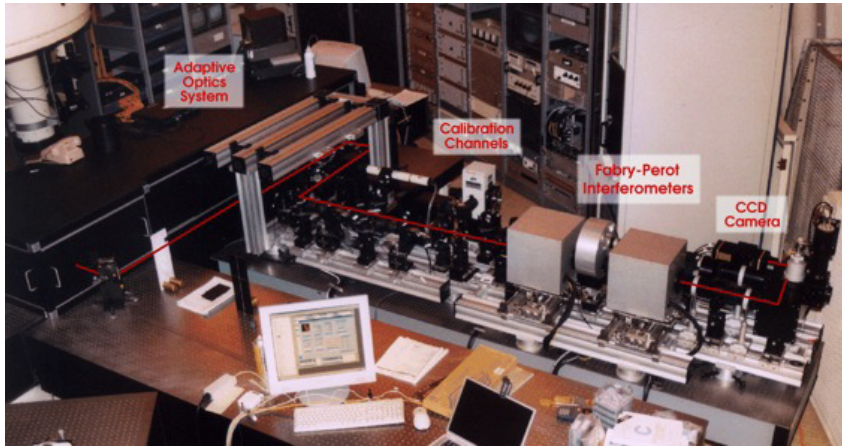


Figure 2.5: Interferometric BIdimensional Spectrometer instrument at DST. The high-lighted red text labels the main light path. The light is passing through the AO system, the two FPIs and finally illuminates the CCD camera. Furthermore, the image include the reference path and calibration channels.³

In Fig. 2.4 we see a scheme of the optical path of the IBIS instrument. The main path is shown with a solid line. After passing the AO system, the light is directed with the lens L0 and the three folding mirrors m1, m2, and m3 to the field stop FS. The diameter of the solar image is 21.3 mm, which corresponds to 80'' on the Sun. The light beam is passing the three lenses (L1, L2, and L3), which collimates the light rays. The folding mirror M1 guides the light into the two Fabry-Pérot interferometers (FPI 1 and FPI 2). The FPIs are mounted in classical mount, which means that the FPI is placed near an image of the telescope's entrance pupil, where the object is at infinity. Here, the pupil image has a size of 35 mm. In comparison, in the telecentric mount the FPI is placed near an object image, where the entrance pupil of the telescope is at infinity. The mount was chosen because of its simpler realization and because the bandpass across the Field-Of-View (FOV) is the same. In consequence, the central wavelength varies across the FOV, which is called blueshift. In the ideal multi-FPI in classical mount, the spectral resolution has a maximum. The image quality and spectral resolution is reduced because of plate defects and inhomogeneities of the coatings (Cavallini, 2006).

The ET50FS FPIs are produced by IC Optical Systems. The coatings are optimized for the wavelength range between 5800 Å and 8600 Å. The FPIs have a multilayer broadband coating. The plate spacing is for the first FPI 2.3 mm and for the second FPI 0.637 mm (Reardon and Cavallini, 2008). The interferometers are piezo-electrically tuned, and the spacing and parallelism are controlled electronically. The wavelength drift is less than 10 m s^{-1} over 10 h. To eliminate spurious reflections on the surface, both FPIs have wedged plates with an angle of $20'$. The accuracy of the adjustment of the interferometer perpendicular to the optical axis is $\pm 10''$ (Cavallini, 2006). The FPIs allow us to extract the spectral information of the observed line. Furthermore, we get a two-dimensional image for each wavelength step. The minimum wavelength step for IBIS is between 45 mÅ and 66 mÅ.

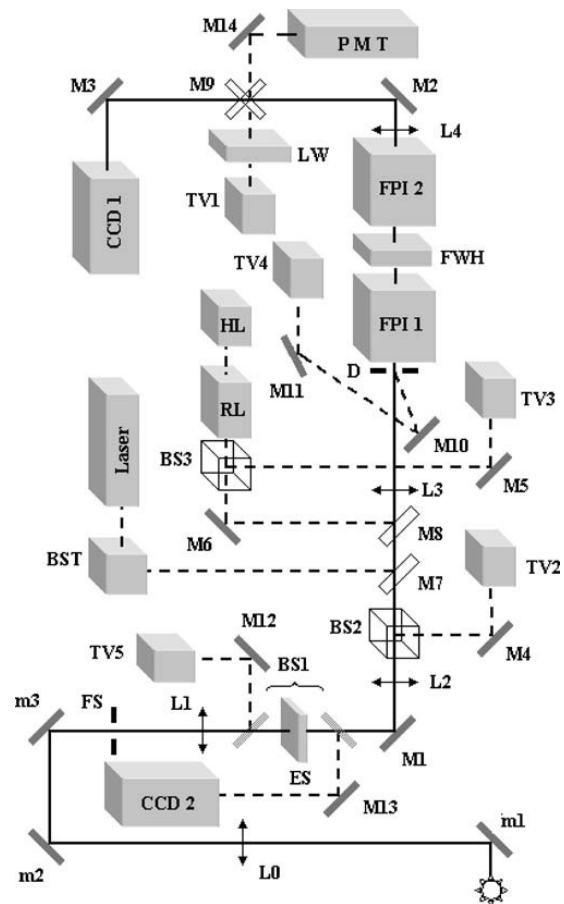


Figure 2.4: Optical path of the IBIS instrument. The main path containing FPI 1 and FPI 2 is shown as a solid line. The dashed lines delineate the reference path for broadband observations and the calibration channels (see Fig. 4 in Cavallini, 2006).

³How does IBIS work?, accessed 2016 June 3, available from arcetri.astro.it/science/solare/IBIS/IBIS_description.html

Table 2.2: The different filters and wavelengths at which IBIS observes and the corresponding atmospheric layers of the Sun. The filters are divided into narrow-band and broad-band filters. The highlighted filters are used in the following data analysis, adapted from nso.spo.nso.edu/dst/smex-setup.

Channel	Filter Name	Central Wavelength	Atmospheric Layer
Narrow-band	Fe I	5434 Å	Temperature minimum
	He D ₃	5876 Å	transition region
	Na I D ₁	5896 Å	temperature minimum
	Fe I	6173 Å	photosphere
	Hα	6563 Å	chromosphere
	Fe I [†]	7090 Å	photosphere [†]
	Ca II	8542 Å	chromosphere
Broad-band		541 nm, 621 nm, 633 nm, 661 nm, 682 nm, 721 nm , 828 nm	

[†][Asensio Ramos et al. \(2006\)](#)

Between the two FPIs, there is a filter wheel with space for five narrow-band interference filters. Depending on the science case a variety of filters is available (see Table 2.2). The filters cover different atmospheric layers: the photosphere (e.g., Fe I λ 6173 Å and λ 7090 Å), the temperature minimum (e.g., Fe I λ 5434 Å and Na I D₁ λ 5896 Å), the chromosphere (H α λ 6563 Å and Ca II λ 8542 Å), and transition region (He D₃ λ 5876 Å). Furthermore, in the filter wheel there are a pinhole and a dark slide available for calibration.

After passing the FPI-system the light is guided with two more folding mirrors (M2 and M3) and a lens L4 towards the CCD camera. Here, the solar image has a size of 6.85 mm in diameter. This CCD camera from Roper PentaMAX is taking monochromatic images. The Kodak KAF-1400 detector has a size of 1317×1035 pixels and physical dimensions of $6.8 \mu\text{m} \times 6.8 \mu\text{m}$ ([Reardon and Cavallini, 2008](#)). The dynamic range of the camera is 12 bits and the camera has a data transfer rate of 5 MHz. The signal has typical values of 15 000 down to 30 ADU with a read noise of $18 e^-$ (1.8 ADU) rms. Each recorded image is the sum of five images, which are added by the camera acquisition software. The resulting images of IBIS have a size of 1007×1007 pixels with an image scale of $0''.08 \text{ pixel}^{-1}$.

Beside the main optical path, there are three more paths. Following lens L1 in the optical path there is a beam splitter (BS1), which sends the light into the reference path. This path allows to observe simultaneously broad-band image together with the main optical path and the same FOV. Additionally to the narrowband filters in the main optical path, there are broadband filters (see Table 2.2). For the observations, there is a second CCD, which is a Dalsa CA-D7-1024T camera. The broad-band camera has 1024×1024 pixels with a pixel size of $6.8 \mu\text{m} \times 6.8 \mu\text{m}$. The dynamic range is 12 bits, and the camera has a data rate of 10 MHz. To perform the initial tuning between the two interferometers and the interference filters, the instrument has a tuning path illuminated by a halogen lamp (HL). The uniform light of the lamp is sent to the interferometers with mirror M8. Furthermore, the alignment of the interferometers is validated with the help of the laser path, in which a frequency-stabilized He-Ne laser sends a beam through the beam steering system (BST) and the mirror M7 towards the FPIs to verify if the interferometers are parallel. The laser simulates a monochromatic source.

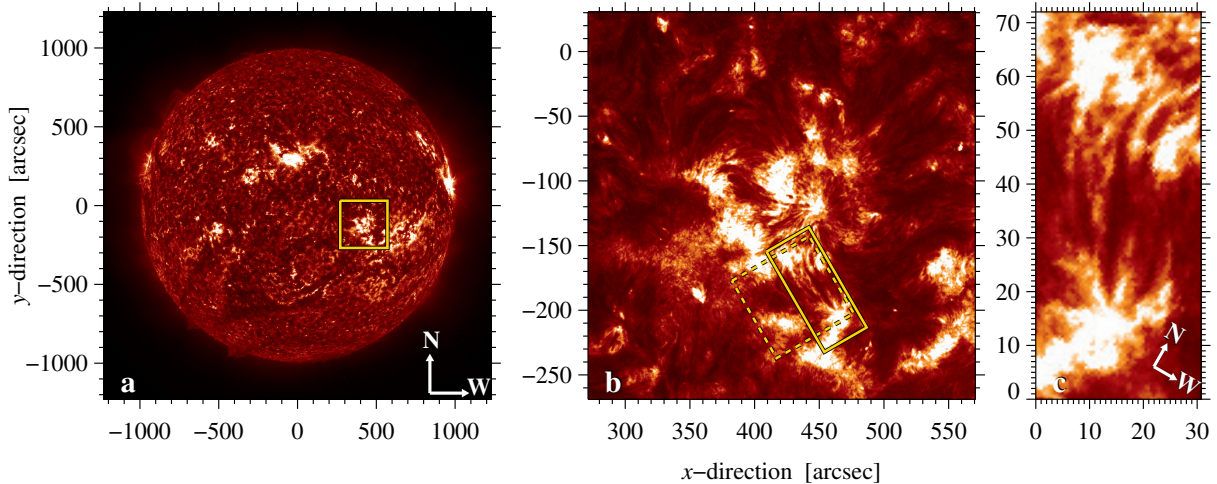


Figure 2.6: Overview of the observed target at 17:35:55 UT on 2013 January 20. (a) Full-disk image of the Sun observed with SDO AIA $\lambda 304 \text{ \AA}$. Active Region NOAA 11658 containing the sunspot and active region filaments is marked with the yellow box. (b) Detailed view on active region NOAA 11658. The sunspot is in the middle of the FOV. Several active region filaments surround the sunspot. The yellow box (solid line) indicates the FOV of IBIS and the yellow box (dashed line) indicates the FOV of ROSA. Both contain the target active region filament. (c) FOV of IBIS with the respective orientation of the IBIS images. The filament is located in the middle of this image, recognizable as a dark structure.

2.2 Data Set

The whole DST data set involves observations obtained in three service mode campaigns within two years (2013–2014). The science case in all three campaigns was to observe the evolution of an active region filament which may lead to a CME. From the first campaign we have data on the 2013 January 20 and February 5. The second campaign contains data on 2013 October 21 and 22. The third campaign was in October 2014. In this campaign our primary science case could not be addressed but there might be service mode campaigns carried out for other principle investigators (PIs), which potentially contain observations of active region filaments. Within the scope of this master thesis, the data set obtained on 2013 January 20 will be analyzed in the following. This data set focused on active region NOAA 11658 which contains an axisymmetric sunspot. The axisymmetric sunspot belongs to the group of so-called theoretician’s spots and belongs according to the McIntosh classification in class H. These spots are usually the remaining leading spots of large bipolar regions and survive after the rest of the group vanished from solar surface. They remain unchanged for several weeks (Stix, 2004). The sunspot is surrounded by filamentary structure (see white square in the left panel of Fig. 2.6). The central coordinates of the active region are 13 S and 32 W, the observed filament has the central coordinates of 15.2 S and 27.6 W at the beginning of the observations at 15:48 UT. We have observations of this region with the three instruments ROSA, FIRS, and IBIS, but we will analyze only the data of ROSA and IBIS.

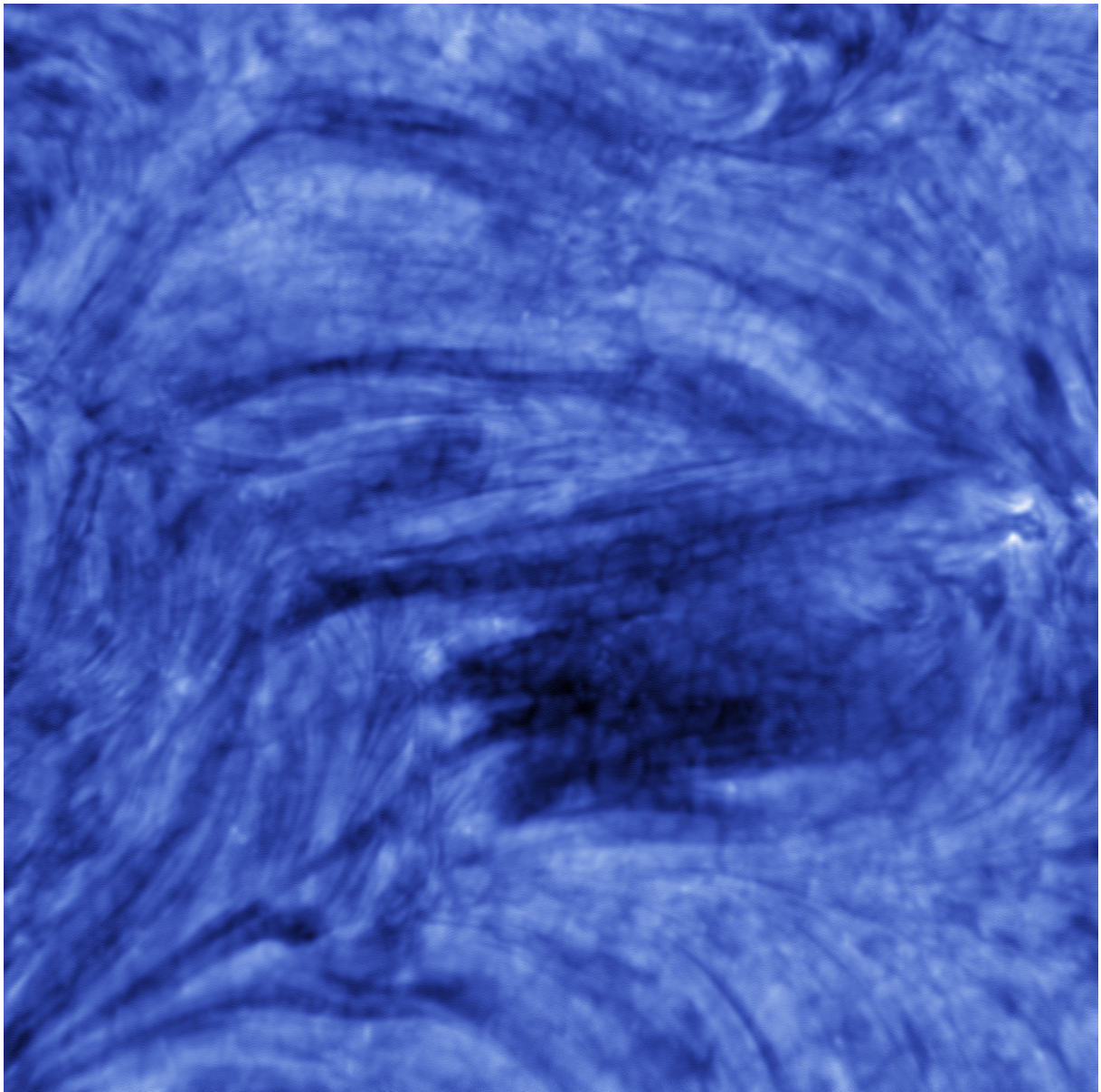
The ROSA instrument observed in three different wavelength, i.e., in $H\beta$ with the UBF filter ($\lambda = 4861.3 \text{ \AA}$), with the G-band filter ($\lambda = 4305.5 \text{ \AA}$), and in the Ca II K line ($\lambda = 3933.7 \text{ \AA}$). All three filters show different layers of the solar atmosphere. The upper photosphere is visible in G-band, the upper photosphere and lower chromosphere are seen in the Ca II K line, and the chromosphere is shown in the $H\beta$ images (see Table 2.1). The advantage of the UBF filter is the narrow bandpass of only 0.2 \AA . The images of ROSA are taken with CCD cameras with a chip size of 1004×1002 pixels. With the pixel size of $0''.069$ the spatial resolution is 100 km with FOV of $50.2 \text{ Mm} \times 50.1 \text{ Mm}$ on the solar surface. During the observations, both the Lyot filter and interference filters were used. The Lyot filter has a very low transmission of less than 10%. The interference filters instead have transmissions of 40–80%. Because of the different transmissions and bandpasses of the filters, different exposure times are needed in the observations. The G-band data have an exposure time of 0.017 s, the $H\beta$ data have an exposure time of 0.45 s, and the Ca II K data have an exposure time of 0.37 s.

The IBIS data contain spectral and white-light observations. The white-light observations are obtained with the 721 nm broad-band filter (see Table 2.2). For the spectral data we have observations of the spectral

lines $H\alpha$ $\lambda 6563 \text{ \AA}$ and $Ca II$ $\lambda 8542 \text{ \AA}$. The exposure time for each channel is 80 ms. The wavelength steps during the scans are not equidistant and vary between 0.24 \AA in the wings to a minimum wavelength step of 0.04 \AA around the line core. The $Ca II$ $\lambda 8542 \text{ \AA}$ data are spectropolarimetric observations, which contain different polarization states yielding the four components of the Stokes vectors. A measurement of the magnetic field is possible with these data. The $H\alpha$ data are spectroscopic observations and only contain measurements of the intensity. Each FITS data file contains 175 images, whereby the first 150 images are $Ca II$ $\lambda 8542 \text{ \AA}$ images with six polarization measurements at each of the 25 wavelength positions. The following 25 images are the intensity measurements in $H\alpha$, one at each position. For each image in $Ca II$ $\lambda 8542 \text{ \AA}$ and $H\alpha$ there is a corresponding broad-band image. Due to the spectropolarimetric mode of the instrument, the images were taken in dual-beam mode. The whole map, containing two images, has a size of 1000×1000 pixels, each pixel with an image scale of $0''.08 \text{ pixel}^{-1}$. Figure 2.6c shows the size and orientation of IBIS images on the Sun.

Chapter 3

Data Reduction and Methods



Front: Best image of the time-series from the active region filament observed in $H\beta$ at 17:21 UT on 2016 January 20. The best image is selected with the Median Filter-Gradient Similarity method.

3.1 Data Reduction and Reconstruction of ROSA Images

The first step before analyzing the data set is to reduce and reconstruct the data. For this purpose, flat-field frames and dark frames have been recorded. Once dark frames and flat-field frames are applied the science frames can be reconstructed with different methods such as speckle masking or multi-frame blind deconvolution.

3.1.1 Dark Frames and Flat-Field Frames

We gain dark frames by taking images with a closed shutter and the same exposure time as for the science frames, which means that each observed wavelength with different exposure time and detector characteristics has its own dark frames. With the help of the dark frames we obtain information about the thermal noise, which is produced by all materials with a temperature higher than 0 K (Howell, 2006; Janesick, 2001). The thermal electrons are raised from the valence band into the conduction band and cause a dark current. To reduce this current, we have to cool down the CCD camera, but the dark current will not disappear completely. Furthermore, the dark frames show hot and cold pixels, which are pixels with more or less electrons than the neighboring pixels which is caused by impurities in the silicon crystal itself. It is sufficient to average several hundred dark frames in order to reduce the thermal noise by the square root of the number of images. The averaged dark frame thus represents the detector characteristics. Note that in the science frame the thermal noise of a single dark frame is still present. Jess *et al.* (2010) suggest to take more than 250 dark frames. For the ROSA data in H β , 783 dark frames are provided.

The raw images contain differences in the light intensity even for uniform illumination, caused by the different sensitivity of the pixels, from contamination by dust, and from vignetting of the optical path. To compensate these effects, we use flat-field frames which are also provided in the data set. Furthermore, by observing with narrow-band filters interference patterns, so-called fringes can appear. They can also be filtered with the flat-field frames, as long they do not change in time and space. To record flat-field frames we need a uniform light source with a similar spectrum to the object of interest. In solar physics it is simply the Sun itself. By observing with high-resolution telescopes like the DST, we need a region close to the solar center with quiet-Sun, without sunspots or pores. In addition we have to take different frames around this point exploiting the fact that solar granulation is uniform and isotropic. Thus averaging a large number of images reduced the granular contrast approaching a uniform light source. Furthermore, it is important to take the flat-field frames temporally close to the science frames. Jess *et al.* (2010) propose to take at least 500 flat-field frames. For the H β data, 1291 flat-field frames are provided. In the following we use the averaged flat-field frame.

For the whole data reduction process as well as for the later analysis of the data we will use the Interactive Data Language (IDL)¹ and various user-supplied program libraries. The data is provided in compressed files written in the Flexible Image Transport System (FITS, Hanisch *et al.*, 2001; Wells, Greisen, and Harten, 1981) format. The header of each FITS file contains, among others, information about the exposure time which we have to use later. Afterwards, we remove intensity spikes in the data set which are caused by hot pixels or cosmic rays. We calculate statistical values for the frames such as mean value and standard deviation. The frames are summed and divided by the total number of frames which gives us the averaged dark frame and flat-field frame. The statistical values, the exposure time, and the averaged frames are saved for later usage to calibrate the science frames.

In Fig. 3.1 we see the resulting averaged flat-field frame (upper row) and dark frames (lower row) for all three filters. In the flat fields, we clearly see defocused dust particles, which are formed like tori (Howell, 2006). The stripes in the images result from fringes or from non-avoidable irregular manufacturing of the silicon chips. Each flat-field frame was obtained with a different camera and a different filter which explains the different appearance of the flat-field frames. The dark frames are taken with closed shutter and the same exposure time as the science frames. In the G-Band and H β frames we see two clearly separated regions, where one region appears brighter than the other (see Fig. 3.1d and 3.1f). Scrutinizing the dark frames we see a bad pixel at coordinates (720 pixel, 729 pixel) for the H β dark frame and at coordinates (90 pixel, 750 pixel) for the G-band dark frame which cause discontinuity in the dark current.

¹www.harrisgeospatial.com

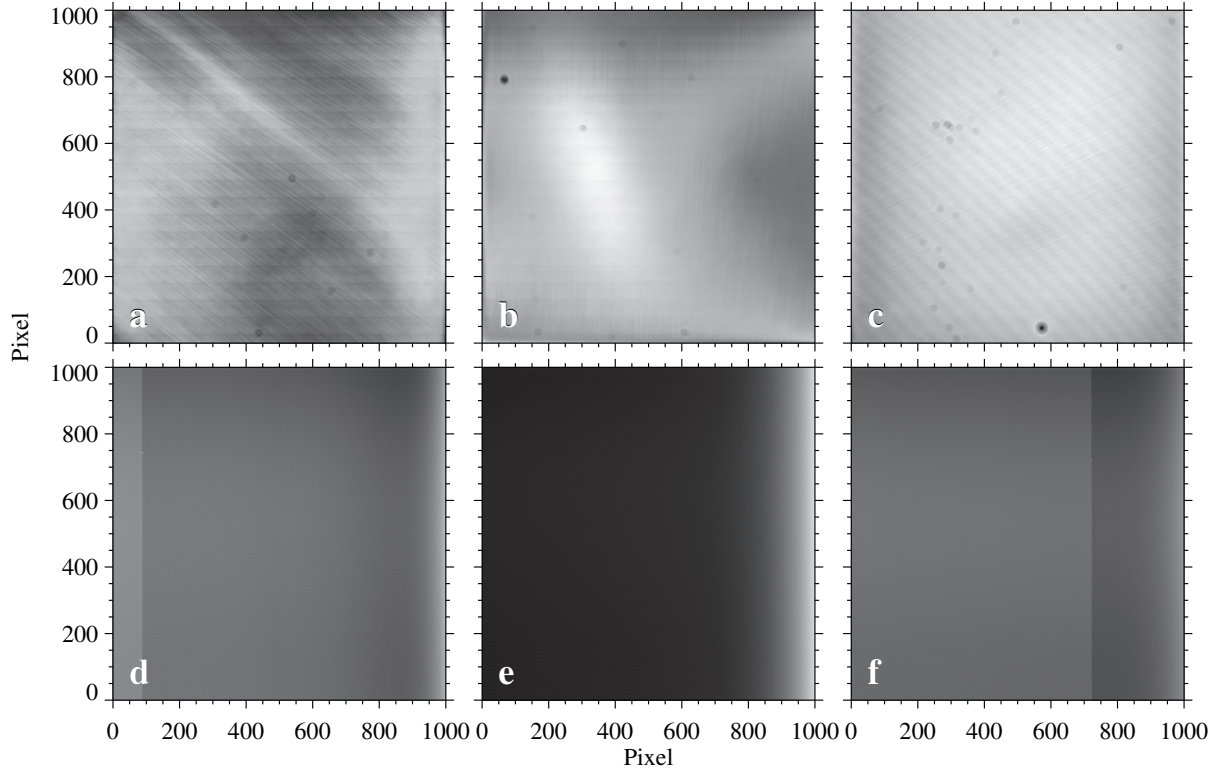


Figure 3.1: Averaged flat-field frames (upper row) and dark frames (lower row) for the ROSA data set: (a, d) G-Band, (b, e) Ca II K, and (c, f) H β .

Beyond the bad spot the intensity is increased by two counts and the frame gets brighter. The reason for the bad spot is not known. By looking at the dark frame of Ca II K (see Fig. 3.1e) we see a mainly uniform intensity distribution beside the right border of the dark frame. There we have a small bright stripe. This stripe is also visible in the other dark frames but much smaller and fainter than here. Those stripes result from the read-out register of the CCD.

3.1.2 Science Frames

We have to reduce the science frames with the averaged dark and flat field frames so that we can later analyze these frames. Therefore, we define the gain which has to be positive, for which we define a threshold $\varepsilon = 10^{-8}$. With this threshold ε we ensure that the gain is always greater than zero

$$\text{gain} = \text{flat} - \text{dark} > \varepsilon. \quad (3.1)$$

Afterwards, we extract the compressed FITS data. Each data file contains no more than 256 single science frames. Each raw image img_0 is subtracted with the dark and divided by the gain

$$\text{img} = \frac{\text{img}_0 - \text{dark}}{\text{gain}}. \quad (3.2)$$

In Fig. 3.2 we see sample images for each of the three filters before (upper row) and after (lower row) the reduction. We have seen the defocused dust particles in the flat fields (see Fig. 3.1, upper row) which we also see in the uncorrected science frames of the Ca II K line and H β (Fig. 3.2b and 3.2c). In the reduced image we have a much clearer impression without these artifacts (Fig. 3.2e and 3.2f). Furthermore, the images are despiked.

In the following, our goal is to increase the spatial resolution and the contrast of the images. Therefore, we have to reconstruct all images. We split the whole data set into sequences of 30 s and work on the sequences in the further steps. First, we have to select the best images of this sequence. For this purpose, we use the new method of Deng *et al.* (2015) which is an easy way to evaluate the image quality of a time series.

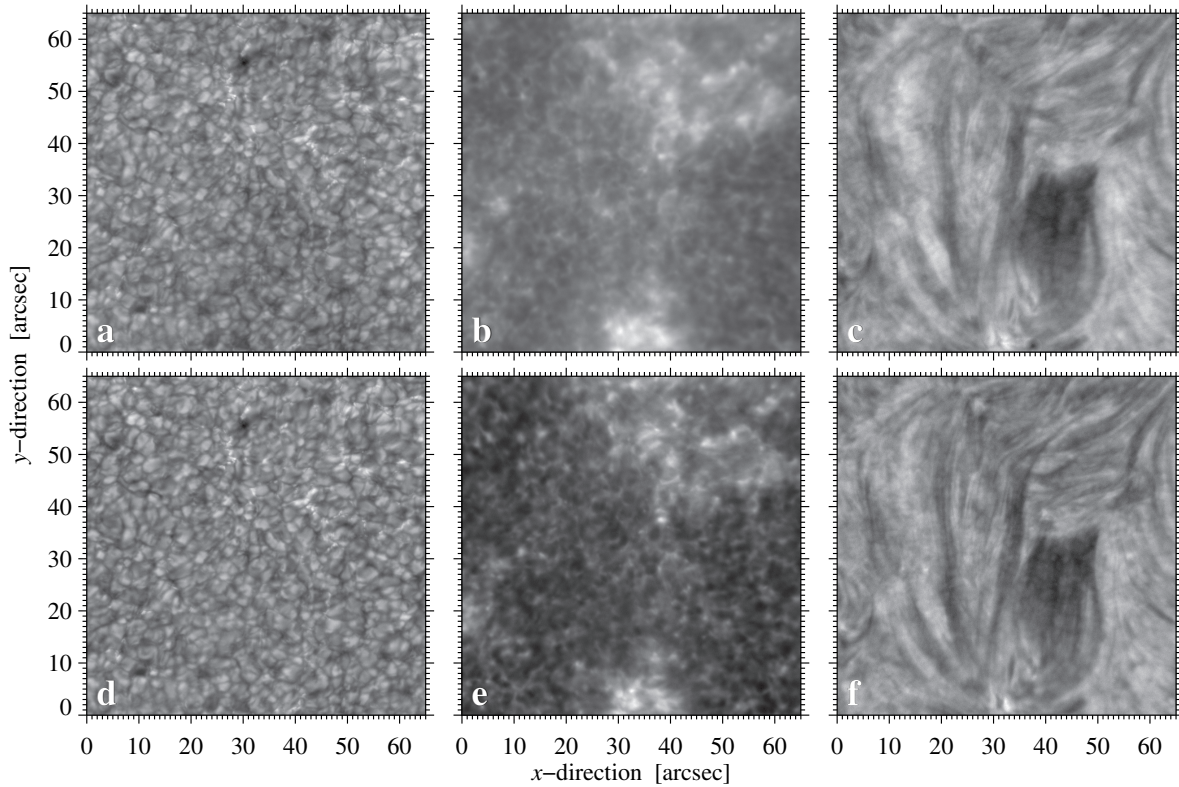


Figure 3.2: Observations before and after reduction: in the upper row we see the data before reduction in the three different filters (a) G-Band, (b) Ca II K, and (c) $H\beta$. In the lower row we see the observations after reduction with dark and flat field frames (d) G-Band, (e) Ca II K, and (f) $H\beta$.

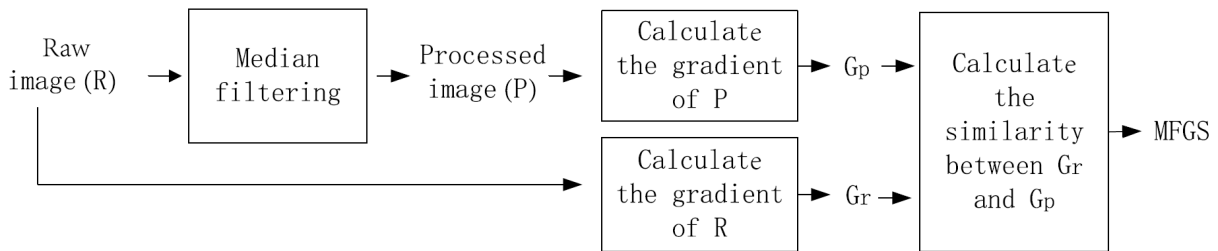


Figure 3.3: Scheme of the Median Filter-Gradient Similarity Method (see Fig. 1 in [Deng et al., 2015](#)).

Median Filter-Gradient Similarity

The Median Filter-Gradient Similarity (MFGS, [Deng et al., 2015](#)) method was recently introduced into solar physics. The scheme of the method is presented in Fig. 3.3. First, the input image R is filtered by a median filter with a size of 3×3 pixels which gives us the processed image P . We calculate in the next step the gradient of both images, R and P . For this purpose we use the [Schar \(2007\)](#) operator for both the x - and y -components and convolve them with the image. The resulting derivatives G_x and G_y are giving the gradient magnitude G with $G = \sqrt{G_x^2 + G_y^2}$. The last step is to calculate the similarity of the the gradients of the input image G_r and the processed image G_p

$$\text{MFGS} = \frac{2G_r G_p}{G_p^2 + G_r^2}. \quad (3.3)$$

This ensure values between 0 and 1. The closer the value is to 1 the better is the image quality.

We now calculate the MFGS values for the ROSA images of all three wavelength bands to get the image quality of the time-series. The results are shown in Fig. 3.4 for the three different wavelength bands. The red points are showing the MFGS values for the original images after applying dark- and flat field

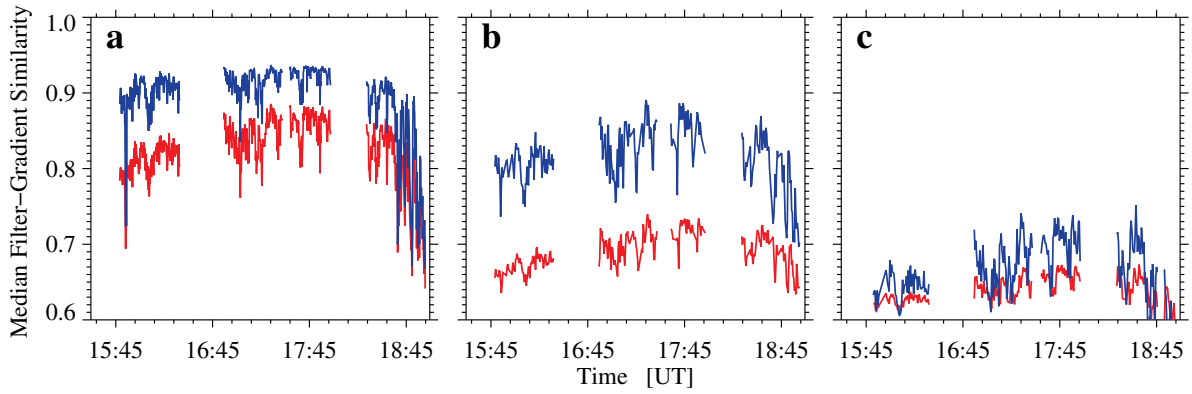


Figure 3.4: Image quality derived with the Median Filter-Gradient Similarity method by [Deng et al. \(2015\)](#): (a) G-Band, (b) Ca II K, and (c) $H\beta$. The red lines are the MFGS values for the original images after applying dark and flat field corrections. The blue lines are for the MFBD-reconstructed images. We see gaps in the time-series which are maybe caused by bad seeing during these time intervals. At around 18:21 UT the target changed from the active region filament to the sunspot of the same active region. In the observational log is noted, that during the sunspot observations there were bad seeing conditions, which is reflected in the decrease of MFGS values in this time.

correction. The blue points are showing the MFGS values of the reconstructed images after applying Multi-Frame Blind Deconvolution (MFBD, [Löfdahl, 2002](#)). We will discuss this method later. We can recognize that the image quality increased by applying the MFBD method to the images. The values of the MFGS method are increased in all cases. We can clearly see that the values for the G-band images are the highest. The average values are of about 0.85 for the non-reconstructed image and reach a mean value of about 0.9 for the reconstructed images (cf. Fig. 3.4a). We derive the maximum value for the G-band data at 17:21:39 UT on 2013 January 20 with $\text{MFGS}_{\text{max,G-band}} = 0.936$. The Ca II K line gives smaller values for the original images. These images have an average value of about 0.7. For the reconstructed images the average value is higher with about 0.8 (cf. Fig. 3.4b). The maximum value is reached at 17:21:22 UT with $\text{MFGS}_{\text{max,Ca}} = 0.891$. The MFGS values in the $H\beta$ wavelength are lower. Their average value is only about 0.65 for the original images. The reconstructed images have a slightly higher average value of about 0.7 (cf. Fig. 3.4c). The maximum value is at 17:21:34 UT with $\text{MFGS}_{\text{max,H}\beta} = 0.741$. The best image quality for all three wavelength are at around the same time, thus the seeing conditions were excellent at that time. The comparison of the MFGS values of different wavelengths is difficult, because the wavelength dependence is not known yet. Further studies analyzing the wavelength dependence and center-to-limb variation are in preparation. Other factors like the amount of fine structure of the target and the signal-to-noise ratio, which is increased by a longer exposure time, influence the MFGS value as well. However, a comparison between time-series is possible. We see in Fig. 3.4 that the seeing increased in the time-series. The best seeing was between 17:00 UT and 17:45 UT. In the later analysis we will use the data of the most stable part of the time-series with the best seeing. Furthermore, we see in Fig. 3.4 that there are gaps in the time-series, which are maybe caused by bad seeing. After the last bigger gap at around 18:21 UT the target changed to the sunspot. During this time, the MFGS values decrease in all three wavelengths. According to the observational log, the seeing conditions decreased as well towards the end of observations.

For the reconstruction of the images, we need the MFGS values which reflect the image quality of the image sequence. In addition, we calculate statistical values such as the mean, minimum, and maximum value, and the standard deviation of each image in the sequence. Afterwards, we create an image which is the sum of all images of the 30 s sequence and represents an image with a long exposure time. In addition, we identify the best image of the sequence with respect to its MFGS value. Furthermore, we determine movements in the image, seeing, and characteristic values of the correction with the AO system. These values are used later in the reconstruction. In the end, the best image of the image sequence is corrected concerning stray light and normalized to the quiet-Sun intensity.

In the beginning of the reconstruction algorithm, we can select between two different methods: (1) Frame Selection ([Scharmer and Löfdahl, 1991](#); [Law, Mackay, and Baldwin, 2006](#)), in which only the best image is selected with the MFGS method, and (2) MFBD, in which we apply the image reconstruction.

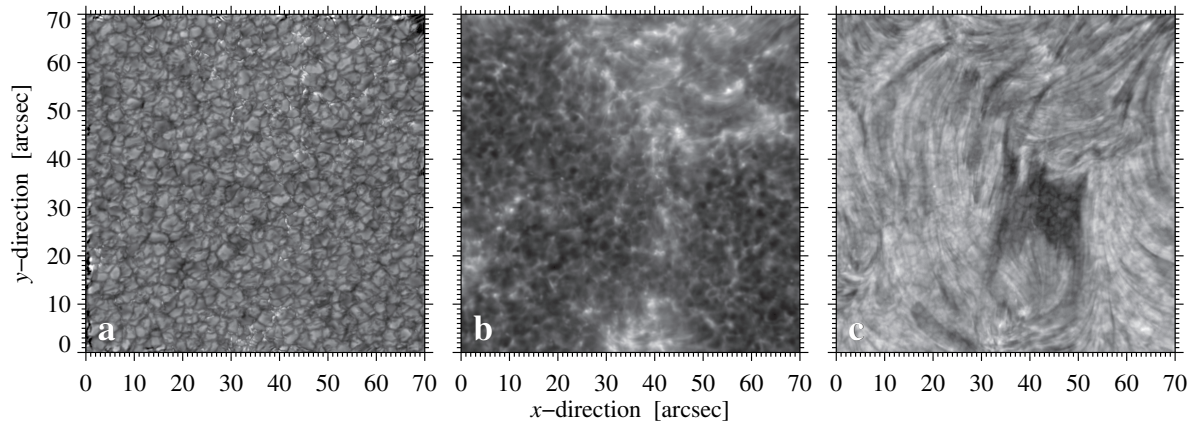


Figure 3.5: Best image after reconstruction with MFBD (a) G-Band, (b) Ca II K, and (c) H β .

By using frame selection, all necessary variables, such as the best image with and without contrast enhancement, image statistics, values for seeing and AO correction, and MFGS values, are saved and can be used in further analysis. By selecting MFBD, further processing steps are needed, which are described in the following section.

Image Reconstruction with MFBD

With the MFBD method, we first select the 16 best images of each sequence and work in the following on these 16 images. We correct the image motion between the 16 selected images, which was derived in the previous step with a cross-correlation of the images. In addition, the images are prepared for the reconstruction with a window- or apodisation function. We enlarge the image with a border of 150 pixels by mirroring the image. This reduces effects at the border of the image, which appear often due to the Fast Fourier Transformation (FFT). After apodising the image we apply the MFBD method to the 16 best image of the image sequence. With this method optical aberrations of the Earth's atmosphere and of the optical components are partly compensated. The MFBD method uses blind deconvolution, in which the Point Spread Function (PSF) is not known; this is different to other deconvolution algorithms. The PSF is found iteratively by solving an optimization problem (Gonzalez and Woods, 2002; van Noort, Rouppe van der Voort, and Löfdahl, 2005; de la Cruz Rodríguez *et al.*, 2015). In the end, we obtain a reconstructed image with higher spatial resolution and contrast. Again, we save all necessary variables for later usage.

In Fig. 3.5 we see the best images after reconstruction with the MFBD method for the three different filters. We end up with very clear and detail-rich images where we can even see solar fine structure. In the G-band image (Fig. 3.5a) we see the granulation in the photosphere clearly with some bright points, which we relate to small-scale magnetic flux tubes (Steiner, Hauschildt, and Bruls, 2001; Schüssler *et al.*, 2003; Rimmele, 2004). Furthermore, we see in the upper right corner parts of the penumbra of the sunspot. In the Ca II K image (Fig. 3.5b) we see the upper photosphere and lower chromosphere. Their bright regions are related to strong magnetic fields. In the H β image (Fig. 3.5c) we see the observed active region filament and recognize that it is not a classical elongated filament, but a clumpy structure. A detailed analysis of the time series, including the calculation of horizontal velocities and determination of footpoints, is given in Sect. 4.2.

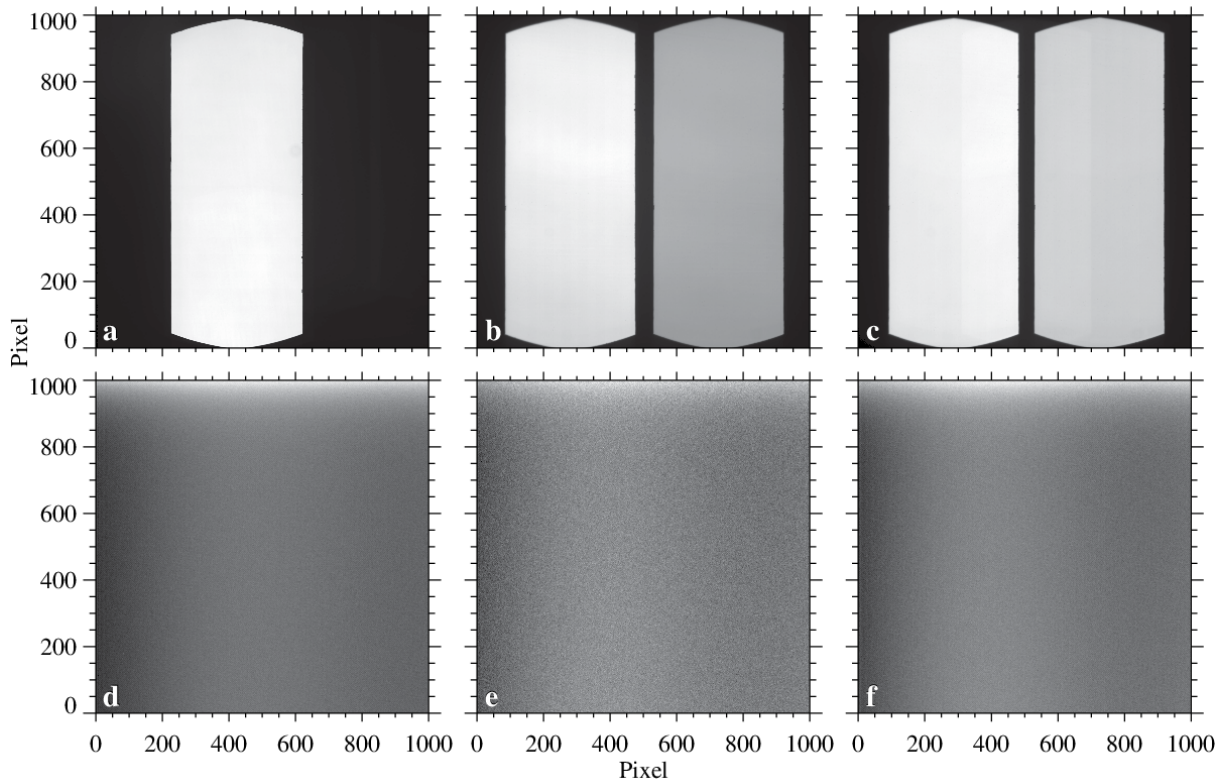


Figure 3.6: Flat-field frames (upper row) and dark frames (lower row) for the IBIS data set: (a, d) broad-band data, (b, e) narrow-band $H\alpha$ data, and (c, f) narrow-band $\text{Ca II } \lambda 8542 \text{ \AA}$ data.

3.2 Data Reduction of IBIS Images

3.2.1 Data Pipeline

For IBIS a data reduction pipeline is provided (Criscuoli and Tritschler, 2014). The reduction is carried out for each filter separately, using different steps for spectroscopic and spectropolarimetric data as well as for broad- and narrow-band data. A certain amount of user interaction is needed for the reduction process. The reduction starts with the generation of the mean dark frames and flat-field frames for both broad-band and narrow-band images. The data reduction for the narrow-band channel is performed first for the $\text{Ca II } \lambda 8542 \text{ \AA}$ data and in the following for the $H\alpha \lambda 6563 \text{ \AA}$ data. The next step is the alignment of the narrow- and broad-band channels, which differ in image scale, magnification, and rotation. The offset between the channels is determined in this step. Here, the additionally taken calibration data of a grid is needed. Each narrow-band image has a corresponding broad-band image. In the following step each narrow-band scan is calibrated with the dark- and flat-field frame as well as resized, aligned, and saved in a separate IDL save file together with additional metadata about, i.e., the wavelength position, time of observation, or light level. The pipeline continues with the determination of the systematic wavelength shift in the narrow-band data by analyzing the averaged flat-field scan. This blue shift is caused by the classical mount of the Fabry-Pérot interferometers. Two methods are used to calculate the wavelength shift. In the first method, the center-of-gravity is calculated, and in the second method a second-order polynomial is fitted to the wavelength points. In the following step the narrow-band scans are corrected for the gain. In addition the images of the broad-band channel can be reconstructed with the speckle method for which the IBIS data pipeline provides a program for preparing data. In the current state, we have not used this possibility but may use it for future analysis of the broad-band data. The next step is the main reduction step in which the narrow-band data is calibrated for dark, gain, the systematic wavelength shift, and image distortions. The resulting reduced images are saved for later analysis. The data reduction is finished with this step for the spectroscopic $H\alpha$ data. The spectropolarimetric $\text{Ca II } \lambda 8542 \text{ \AA}$ data is going through three additional reduction steps to separate the four Stokes vectors. In the first step the polarization calibration curve is generated with 112 polarization calibration measurements during the observations. In

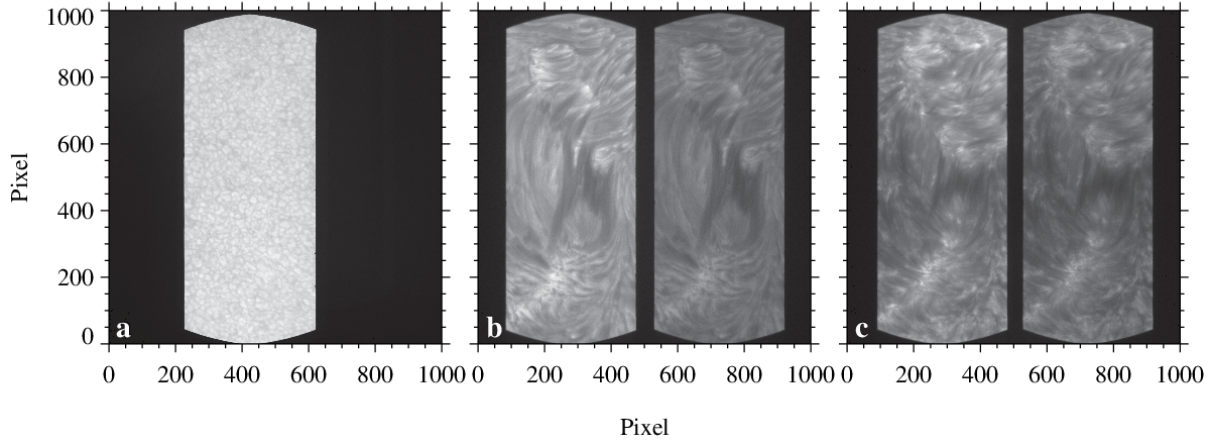


Figure 3.7: Raw data of the IBIS data set at around 17:22 UT: (a) broad-band data in single-beam mode, (b) dual-beam narrow-band line-core image in $H\alpha$, and (c) dual-beam narrow-band line-core image in $Ca II \lambda 8542 \text{ \AA}$. Note that the $Ca II \lambda 8542 \text{ \AA}$ data have different polarization states in the two parts of the map.

the second step the polarization curve is used to calculate the polarimeter response function. In the last step this function is used to demodulate and calibrate the images for different polarization states and to separate the Stokes vectors. In the end, we get a narrow-band image for each of the four Stokes vectors at each of the 25 wavelength positions.

In Fig. 3.6 we see the flat-field and dark frames for the three different IBIS data sets: 7210 \AA broad-band data (Fig. 3.6a, d), narrow-band $H\alpha \lambda 6563 \text{ \AA}$ data (Fig. 3.6b, e), and $Ca II \lambda 8542 \text{ \AA}$ data (Fig. 3.6c, f). In the flat-field frames we recognize the dual-beam mode of the narrow-band data (Fig. 3.6b, c) and the single-beam mode of the broad-band data (Fig. 3.6a). The dark frames all look similar with a brighter stripe at the lower border of the image. This results, as described for the ROSA data, probably from the read-out register of the CCD camera.

The flat-field and dark frames are used to calibrate the raw data of IBIS, which is presented in Fig. 3.7. The presented data is chosen concerning the time of the best observing conditions for the ROSA data at around 17:22 UT. The broad-band image shows the photosphere at 17:22:11 UT (Fig. 3.7a). We recognize the characteristic granulation patterns. The narrow-band $H\alpha$ image is the line-core image of the spectral scan at the same time. We see the typical filamentary structure of fibrils in the chromosphere and of course the science target, i.e., the active region filament. In addition, the narrow-band $Ca II \lambda 8542 \text{ \AA}$ image shows the line-core with a polarization state combining two Stokes vectors (I-V) at 17:22:28 UT. Even without image reduction the data is of high quality and high contrast. The narrow-band images show the filament and its footpoints. These bright regions in the $Ca II \lambda 8542 \text{ \AA}$ image (Fig. 3.7c) are associated with strong magnetic field. For comparison, the reduced data is shown later in Fig 3.9.

3.2.2 Data Products

With the reduced images we can now analyze the IBIS data. First of all, we will evaluate the image quality over the time of observations for the two narrow-band channels and the broad-band channel, see Fig. 3.8. As seen for the ROSA data (Fig. 3.4), we see a stable image quality over the whole observing period, whereas the image quality decreases towards the end of observations, when the sunspot became the science target. These observational gaps match with the interruptions in the ROSA data. The image quality of the broad-band images in 7210 \AA is shown in Fig. 3.8a. For each narrow-band image in $Ca II \lambda 8542 \text{ \AA}$ or $H\alpha$ exists a broad-band image. In total, all MFGS values in broad-band are higher than a minimum value of $MFGS_{\min, BB} = 0.82$. The maximum value for the broad-band images is $MFGS_{\max, BB} = 0.98$ at the end of the time-series covering the filament at 16:18:16 UT. The mean value is $MFGS_{\text{mean}, BB} = 0.96$. Most of the broad-band images have values larger than 0.9. We have also seen for the photospheric G-Band data that high MFGS values are obtained. The $H\alpha$ values differ more from each other (see Fig. 3.8b). The mean value here is $MFGS_{\text{mean}, H\alpha} = 0.87$. The maximum value is reached at 17:22:08 UT with a

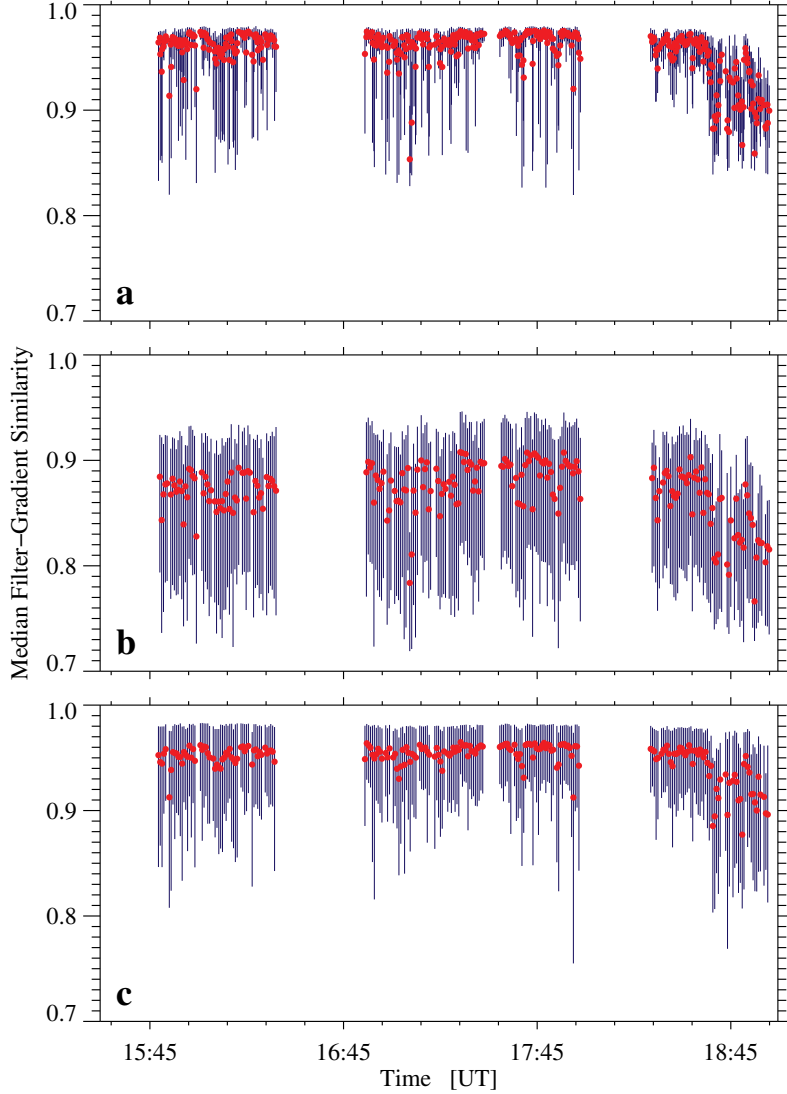


Figure 3.8: Image quality derived with the Median Filter-Gradient Similarity method by (Deng *et al.*, 2015) for the data of the IBIS instrument: (a) broad-band time-series, (b) $H\alpha$ observations, and (c) $\text{Ca II } \lambda 8542 \text{ \AA}$ time-series. The red points are the mean MFGS values for each time loop. The blue stripes are plotted between the minimum and maximum value of the a image sequence. We see gaps in the time-series. At around 18:21 UT the science target is changed from the active region filament to the sunspot of the same active region. The observing log reports that during the sunspot observations there were bad seeing conditions, which is reflected in the MFGS values during this time period.

value of $\text{MFGS}_{\text{max},H\alpha} = 0.946$. At around the same time also the ROSA data showed a maximum in their MFGS values. For the $\text{Ca II } \lambda 8542 \text{ \AA}$ data the maximum value for each time scan is quite uniform at around 0.98 (see Fig. 3.8c). However, the minimum value is varying much more. The mean MFGS value of all observations is for $\text{Ca II } \lambda 8542 \text{ \AA}$ $\text{MFGS}_{\text{mean,Ca}} = 0.95$. The maximum MFGS value is reached at 16:01:38 UT with $\text{MFGS}_{\text{max,Ca}} = 0.983$. The high values can be explained with the high contrast in the infrared Calcium observations. At 17:23:24 UT, where a good image quality for ROSA and $H\alpha$ data was achieved, the $\text{Ca II } \lambda 8542 \text{ \AA}$ data has a local maximum with a value of 0.982, which barely differs from the global maximum at 16:01:38 UT.

Based on the MFGS-values, we selected the best images for each filter, and we have chosen for the narrow-band images the best image in the line-core and present them in Figure 3.9. The best broad-band image (Figure 3.9a) has a value of $\text{MFGS}_{\text{max,bb}} = 0.98$ and it was taken at 16:18 UT. All images are resized in order to cut out a rectangular frame with the same size. The broad-band image has a size of 370×900 pixels, which corresponds to a size of $29''.6 \times 72''.0$. In the broad-band images we see the granulation and some darker pore-like structures, which may indicate strong magnetic fields at those locations. The narrow-band images show the line-core of the scanned line. Figure 3.9b displays the $H\alpha$ line-core image with the filament in the middle of the FOV. As for the ROSA $H\beta$ data, we see that the filament is broader than for typical filaments. The MFGS value of this image is $\text{MFGS}_{\text{max},H\alpha,\text{core}} = 0.917$ at 17:53:44 UT, which is the best line-core image. We can see the filamentary structure of the fibrils in the chromosphere, which is typical for this line. At the extreme ends of the filament we see bright regions, which may refer to footpoints at approximately the coordinates $(10'', 55'')$ and $(4'', 5'')$. By comparison with magnetic field data, we have to proof our assumption, that the bright regions belong

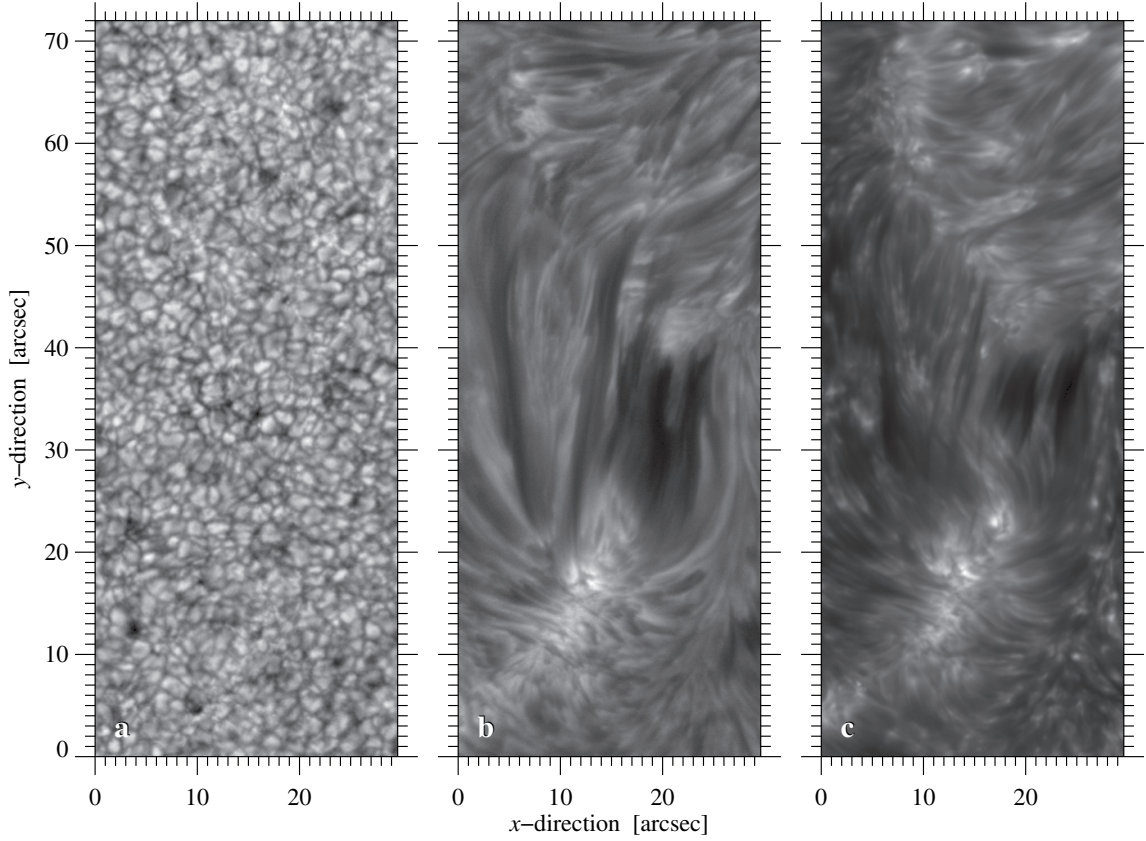


Figure 3.9: (a) Best broad-band image at 16:18:16 UT, (b) best line-core $H\alpha$ images at 17:53:44 UT, and (c) best line-core $\text{Ca II } \lambda 8542 \text{ \AA}$ image at 17:57:13 UT. The images are resized to $29''6 \times 72''0$.

to footpoints. The second narrow-band image presents the best line-core image of $\text{Ca II } \lambda 8542 \text{ \AA}$ -line with a $\text{MFGS}_{\text{max,Ca,core}} = 0.972$ at 17:57:13 UT. Again we see traces of the filament as dark structures in the middle of the image. As mentioned before, the infrared Ca II -line is sensitive to the magnetic field and appears bright at dense magnetic-field concentrations. At the same locations, where we expect the footpoints in $H\alpha$, the brightenings appear in this line. This line shows a different structure as the ROSA Ca II K line at $\lambda 3934 \text{ \AA}$, where we see similar filamentary structures as in the $H\alpha$ line. This could be explained, by assuming that the infrared Ca II line is located higher in the chromosphere as the blue Ca II K line.

3.2.3 Prefilter Curve for $H\alpha$ and Calcium

Before we can work with the spectral profiles recorded in the spectroscopic data set, we have to inspect the prefilter curve. Each filter has a certain transmission curve, which influence the spectral profile of the data set. We first have to extract this curve from the data, in order to correct the spectra with the prefilter curve. To extract the prefilter curve from the data we start with an average spectrum derived from the flat-field frames. The spectrum for the flat-field frames as well as for the science data is not on an equidistant grid. Furthermore, we compare the DST spectrum with a theoretical spectrum from the Kitt Peak Fourier Transform Spectral (FTS, [Brault, 1985](#)) atlas. The FTS spectrum is selected for the observed wavelength range of the DST spectrum, but with a dispersion $d_{\text{FTS}} = 0.02 \text{ \AA}$. In order to calculate the exact minimum position of the curve, we fit a second order polynomial for $\pm 0.2 \text{ \AA}$ around the line core. Afterwards, we interpolate the DST spectrum to an equidistant grid with the same dispersion as the FTS spectrum. For this spectrum we also calculate the minimum of the spectral line by fitting a second order polynomial. In the following, we shift the FTS spectrum by the difference of the two minima. To derive now the prefilter curve, we divide the two spectra from FTS and DST and fit to this ratio a Gaussian function. The fit result is our prefilter curve. Each spectrum has to be divided by the prefilter curve.

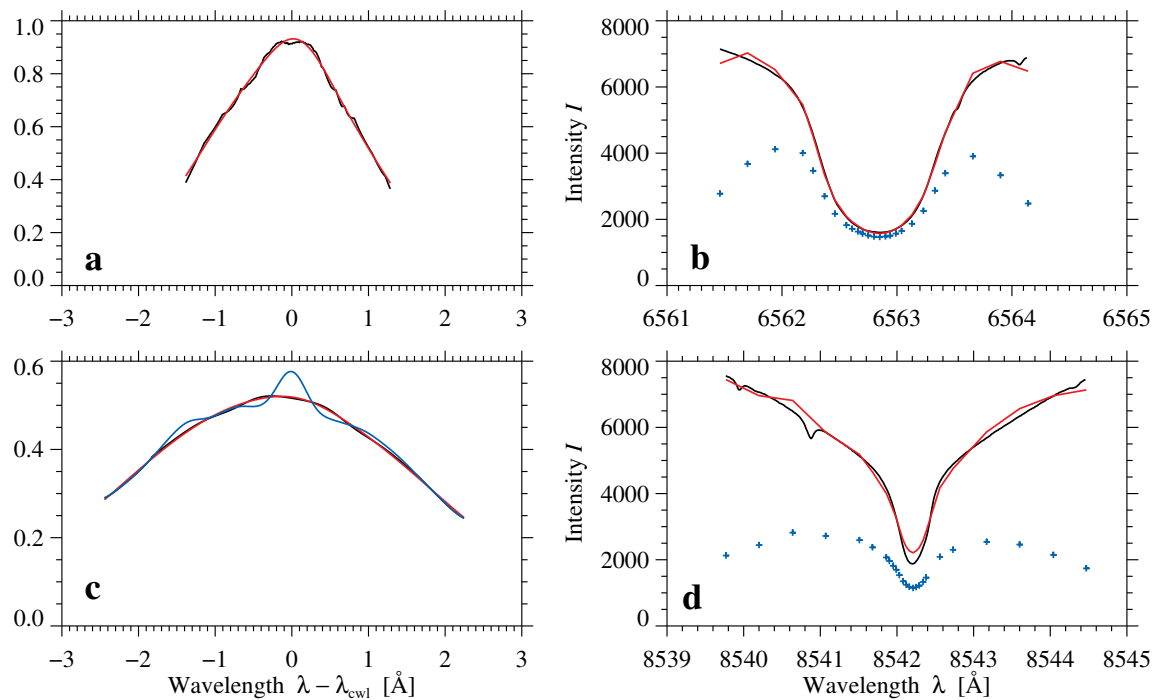


Figure 3.10: (a) Prefilter curve y for H α calculated by dividing the FTS spectrum by the DST spectrum (black line) as well as a Gaussian fit (red line). The abscissa is given with respect to the central wavelength $\lambda_{cwl} = 6561.46$ Å. (b) FTS spectrum (black line), original DST spectrum (blue crosses), and corrected DST spectrum after division by the prefilter curve (red line). (c) Prefilter curve y for Ca II $\lambda 8542$ Å calculated from dividing the FTS spectrum by the DST spectrum (blue line) as well as a smoothed version (black line) and the Gaussian fit (red line). (d) FTS spectrum over the wavelength (black line), original DST spectrum (blue crosses), and corrected DST spectrum after division by the prefilter curve (red line).

The ratio of DST and FTS spectra is shown for H α in Fig. 3.10a (black line) as well as the Gaussian fit (red line). The fit represents the ratio well and is a good approximation of the H α prefilter curve. In Fig. 3.10b, we see the FTS spectrum for H α (black line), the original DST spectrum (blue crosses) as well as the corrected spectrum by dividing the DST spectrum by the prefilter curve (red line). The original DST spectrum has a different shape compared to the FTS spectrum, because of the transmission curve of the prefilter. Therefore, we correct the spectrum by exactly this prefilter curve and obtain a corrected curve comparable to the theoretical FTS spectrum. The correction for the Ca II $\lambda 8542$ Å line is a bit more complex, because this line is narrower than the broad H α line. As evident in Fig. 3.10c, the ratio of the DST and FTS spectra does not have the typical shape of a prefilter curve as seen for H α . Therefore, we have to smooth the ratio (Fig. 3.10c, black line). The Gaussian fit to the smoothed ratio yields the prefilter curve (red line) for Ca II $\lambda 8542$ Å. The comparison of FTS spectrum (black line), original DST spectrum (blue crosses), and corrected spectrum (red line) is shown in Fig. 3.10d. Again, we see the influence of the transmission curve of the prefilter on the shape of the original DST spectrum. After correcting the DST spectrum with the prefilter curve, the shape is comparable to that of the theoretical FTS spectrum. In the following analysis, we will divide the spectral profile for each pixel by the prefilter curve.

3.3 Measuring Flows in Filaments

By analyzing the dynamics of solar structures, it is necessary to measure the velocities within and around a filament. Several methods can be used for this purpose. We will introduce briefly three common methods in the following sections, which can be divided into techniques measuring horizontal (plane-of-sky) and line-of-sight (LOS) velocities.

3.3.1 Horizontal Flows

One way of obtaining horizontal proper motions is feature tracking, where the locations of certain features are followed in consecutive images. Limiting factors of this method is their dependence on the resolution of the images. Features of fine structures, not resolved in the images, cannot be tracked by this method (Kucera, 2015). Furthermore, the variation of intensity is not only provoked by the tracked features, but can also result from different causes, as variations in temperature or density of the plasma, which makes it difficult to interpret the data correctly. High spatial and temporal resolution is needed to precisely track horizontal flows in images. Furthermore, in limb observations, it is often difficult to distinguish between curved horizontal motions or actual vertical motions (Kucera, 2015).

Time-Slice Method

The time-slice method is an easy method to visualize the temporal evolution of a certain region of the Sun and to determine the horizontal flows within this region. A linear one-dimensional slice is selected in the data. The data values within the slice are plotted as a function of time for consecutive data frames in the time-series. The horizontal motions of features passing the slice can be tracked, and visualize the merging and splitting of features. It is an easy method, well suited for high spatial and temporal resolution images. It is not necessary to have a linear slice but also a curve can be used to follow the trajectory of particular features (Kucera, 2015).

Local Correlation Tracking

Local correlation tracking (LCT, November and Simon, 1988; Verma and Denker, 2011) calculates the localized cross-correlation between two images of a time-series and yields a displacement vector. It was first developed to track clouds in Earth's atmosphere by Leese, Novak, and Clark (1971). November and Simon (1988) implemented the technique for solar physics to track features in the photosphere. The LCT algorithm was adapted by Verma and Denker (2011) to use it on G-band images of the Solar Optical Telescope (SOT, Tsuneta *et al.*, 2008) on board Hinode (Kosugi *et al.*, 2007). We will apply the LCT algorithm to ROSA images to determine the horizontal flow velocities in the photosphere and chromosphere. The following description of the LCT method is based on the work of Verma and Denker (2011) and November and Simon (1988). First, a high-pass filter is applied to suppress gradients related to structures smaller than granules. Therefore, we define a Gaussian kernel:

$$g(x', y') = \frac{1}{2\pi\sigma^2} e^{-\frac{r(x', y')^2}{2\sigma^2}}, \quad (3.4)$$

where the standard deviation $\sigma = \text{FWHM}/2\sqrt{2\ln 2}$ and $r(x', y') = \sqrt{(x'^2 + y'^2)}$. The FWHM has a value of 1200 km (≈ 24 pixels). We use the LCT algorithm on a sub-image $i(x', y')$ with 48×48 pixels, which corresponds to a size of 2364 km \times 2364 km. The coordinates x' and y' are related to the sub-image. To compute the high-pass filter we create a background image with a low-pass filter

$$i_{\text{low}} = i(x, y) \otimes g(x', y'), \quad (3.5)$$

where \otimes denotes a convolution of the Gaussian g and the original image i . The low-pass filter is then subtracted from the image to get the high-pass filter:

$$i_{\text{high}} = i(x, y) - i_{\text{low}}. \quad (3.6)$$

This high-pass filter is computed for the image $i_l(x, y)$ and its previous image $i_{l-1}(x, y)$. Afterwards, each image pair is multiplied with the weighting function $g(x', y')$ centered on the coordinates (x, y) of each pixel:

$$a = i_{l-1}(x, y, x', y') g(x', y') \quad \text{and} \quad (3.7)$$

$$b = i_l(x, y, x', y') g(x', y'). \quad (3.8)$$

The main part of the LCT algorithm is computing the cross-correlation function $c_l(x, y, x', y')$

$$c_l(x, y, x', y') = \Re\{\mathcal{F}^{-1}[\mathcal{F}(a) \cdot \mathcal{F}^*(b)]\} d(x', y'), \quad (3.9)$$

where \mathcal{F} denotes the FFT, \mathcal{F}^{-1} the inverse of it, and \mathcal{F}^* refers to the complex conjugate of \mathcal{F} . Additionally, we define the mask $d(x', y')$, which restricts the maximum of the cross-correlation to a distance of $c_{s, \text{lim}} = 22$ pixels from its center. This corresponds to a maximum flow speed of 18 km s^{-1} which is still reasonable.

We divide the positional shifts by the time difference between the images and scale them to obtain velocities in kilometers per second. In order to yield the persistent flow field, the velocities are averaged over the whole time-series. Thus, contributions by atmospheric seeing are reduced (November and Simon, 1988) but more importantly the evolution of individual fine structures is filtered out. In the end, we obtain a good approximation of the horizontal velocities in and around the filament.

3.3.2 Line-of-Sight Velocities

Line-of-sight velocities are calculated from spectral data, whereby the wavelength shift $\Delta\lambda_i$ of each pixel i in the image to a reference wavelength λ_0 is measured. The velocity v_i of each pixel is then obtained, by using the Doppler law

$$\frac{\lambda_i - \lambda_0}{\lambda_0} = \frac{\Delta\lambda_i}{\lambda_0} = \frac{v_i}{c} \quad (3.10)$$

$$\Rightarrow v_i = \frac{\Delta\lambda_i}{\lambda_0} \cdot c, \quad (3.11)$$

where c is the speed of light in vacuum. The shift is calculated by fitting a function, i.e., Gaussian function to the spectral line profile in each pixel of the image and finding the minimum position of the Gaussian. The LOS velocities give reliable values for flows by using high-spectral resolution spectra. A potential problem of this method is to define a reference wavelength. Therefore, we have to select an area, which we assume to be at rest (Kucera, 2015). Averaging the spectra of this area gives a reference wavelength λ_0 . It is appropriate to use the quiet-Sun at disk center as reference (Kucera, 2015) taking into consideration convective blue-shift and thus the formation height of the spectral line. However, the Doppler velocities are always relative to this reference wavelength. Many factors can influence the accuracy of the values, such as the temperature of the instrument, changes in the refractive index of Earth's atmosphere, or changes in the density or temperature in the observed solar atmospheric layer (Kucera, 2015).

Having access to both horizontal and LOS velocities makes it possible to combine the observations to obtain a three dimensional view of the filament. We have ROSA images, which allows us to use LCT on the data set in different atmospheric layers. For the spectral data of IBIS, we will calculate the Doppler velocities in the chromosphere. Combining the different velocity measurements is difficult, because the data originates from different spectral lines and layers. Furthermore, the LOS velocities depend on the reference wavelength λ_0 , and for the LCT velocities we only yield the persistent horizontal proper motions over the entire time-series of two hours. Still we can compare the locations in the filament, where high velocities are tracked, which helps us to improve our understanding of the physical processes in filaments.

3.4 Error Estimation

By analyzing experimental or observational data, it is important to estimate the uncertainties of the results. Basically, there are two main types of uncertainties: random and systematic errors (Gregory, 2005). The random errors in observational astrophysics are mainly caused by the photons measured on a detector. For a CCD we divide between photon noise and readout noise. Photon noise is proportional to n^{-2} , where n is the number of detected photons. The readout noise is a specific value of the CCD camera, which is in the case of the ROSA and IBIS cameras in the order of $15 \text{ e}^- \text{ s}^{-1} \text{ pixel}^{-1}$. In solar physics the random error is rather small because of the large amount of photons which are collected. Reducing random noise requires an averaging a large amount of data but averaging the data may eliminate signals, which may occur random but may later be discovered as a real signal (Gregory, 2005). The systematic errors are related to the instrumental setup or to the model used for the data. In the telescope and instrument setup each optical surface such as mirrors or lenses can cause systematic errors, which influence the quality of the data. They are predictable and usually constant if the setup and model is not changed. Included in the group of systematic errors are the numerical errors. They depend on the accuracy of the algorithm and the accuracy of variables such as floating points. We will see that the choice of a certain model has a significant influence on the resulting properties. Therefore, the analysis of the χ^2 -statistics of the model can be used to evaluate if a model is sufficient or not.

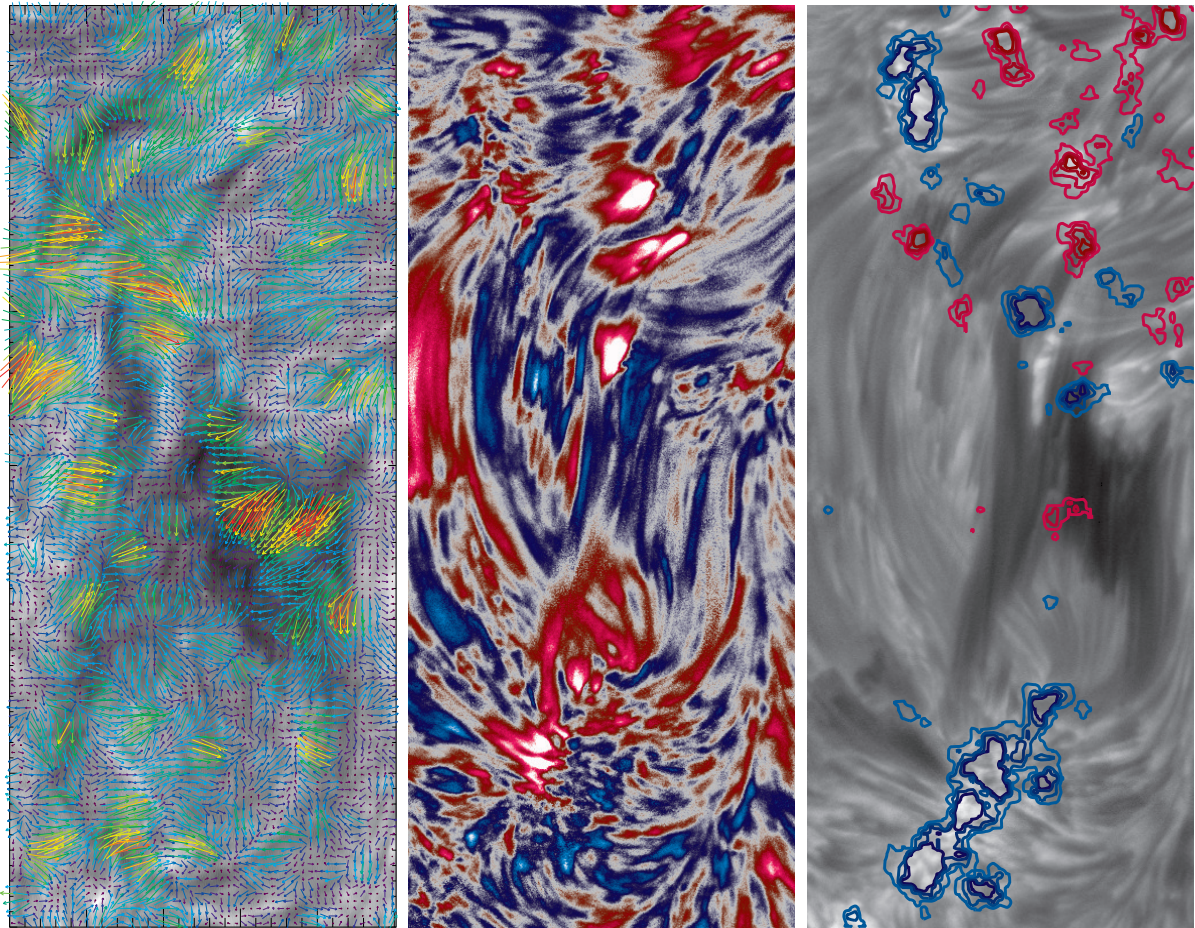
Furthermore, the statistical analysis of data is sufficient summarizes the main properties of the data. Therefore, we will introduce the terms variance S and standard deviation σ of the sample. The spread of the data points or variance S of the sample is defined as

$$S = \frac{1}{n-1} \sum_{j=0}^{n-1} (X_j - \bar{X})^2, \quad (3.12)$$

where n is the number of elements, X_j are the points in the sample, and \bar{X} is the mean value of the sample (Ludwig, 1969; Gregory, 2005). The variance describes the width of the sample distribution. The standard deviation is the positive square root of the variance: $\sigma = \sqrt{S}$. In the following sections, we will provide the maximum flow speeds as well as the average value for the flow speed for horizontal and LOS velocities. The average flow speed value will be given with the corresponding standard deviation σ of the FOV, which refers to the variation in the data and does not reflect an error estimate. The variance is a physical property of the data.

Chapter 4

Results



Front: (*left*) Local correlation tracking applied to $H\beta$ images. The averaged horizontal velocity vectors derived with LCT are plotted over the underlying best image of the time-series at 17:21 UT. (*middle*) Line-of-sight velocities for the $H\alpha$ image. The velocities are derived with line-core fitting and the determination of the central position λ_c of the spectral line, which is compared to a defined λ_0 . The redshifts belong to down-streaming flows and the blueshifts to up-streaming flows. (*right*) Best $H\alpha$ image at 17:22 UT with contours of the positive (red) and negative (blue) magnetic field between ± 50 and ± 200 G in steps of 50 G where the intensity increases with the strength of the magnetic field.

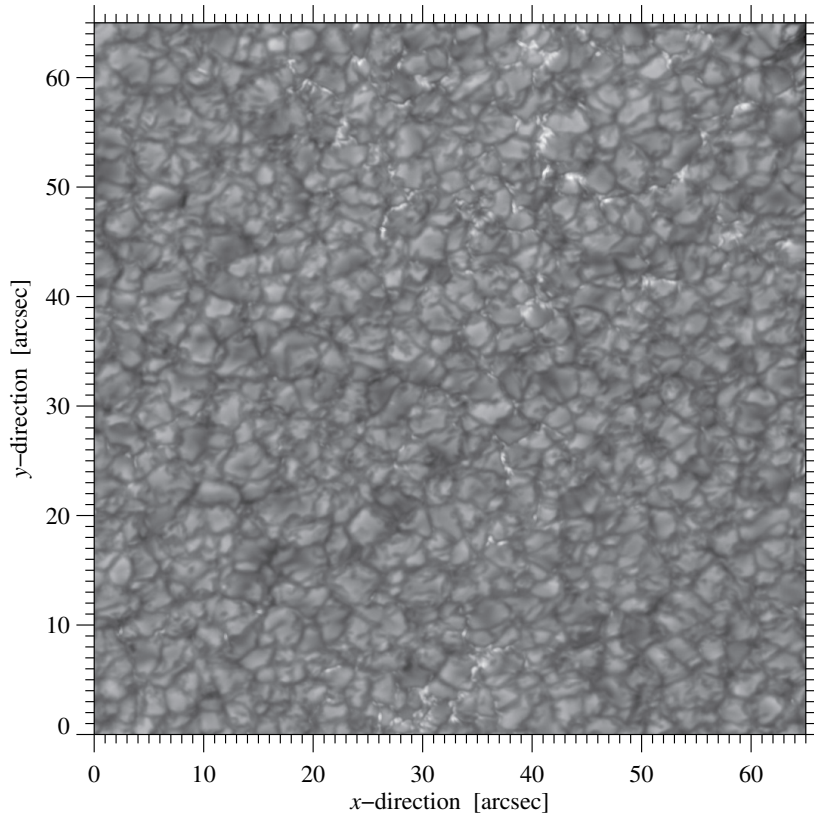


Figure 4.1: Best G-band image of the time-series at 17:21:39 UT on 2013 January 20 with a MFGS-value of 0.94. The image shows the photospheric granulation with some G-band bright points. At the upper right corner parts of the penumbra of the sunspot are visible.

4.1 Motivation

With the data from the DST we have a very complete and substantial data set in many different wavelength covering different layers of the solar atmosphere. The target of this observing campaign was an active region filament close to an axisymmetric sunspot. Within the scope of this thesis, we want to gain new knowledge concerning properties of filaments. We are especially interested in the process of plasma transportation and the stability of the filament. Furthermore, we will contribute to answer some open questions, such as how the cool plasma is maintained in the filament or how the filament is connected with the magnetic field.

4.2 Results from the ROSA Data Set

The first step to examine the active region filament is to analyze the dynamics of the filament. Therefore, we derive the horizontal velocities for the ROSA data set in photosphere and chromosphere. We apply LCT on the three data sets in different wavelength ranges and present the results in the form of vector maps of the horizontal velocities. Thus, we can explore the transport of plasma within the observed layer of the solar atmosphere. With this data set we have the possibility to see the upper photosphere in the G-band data, the upper photosphere and lower chromosphere with the Ca II K data, and the chromosphere in the $H\beta$ data.

4.2.1 Local Correlation Tracking on G-Band images

We use the G-band images as an example to explain how the data is prepared for LCT and how it is applied to the data set. Furthermore, we will show the vector velocity maps and discuss the results for the G-band. The G-band data set is already reconstructed with the MFBD method (see Fig. 4.1 for best image of time-series). Note, the detail-rich granulation with bright points and parts of the penumbra of the nearby sunspot in the upper right corner of the image. Still, some preparation of the data is needed. Some images show strong fluctuations in intensity or contain artifacts from the image restoration process. We removed these image manually from the data set, which amounts for the G-band data set to 10 images. For

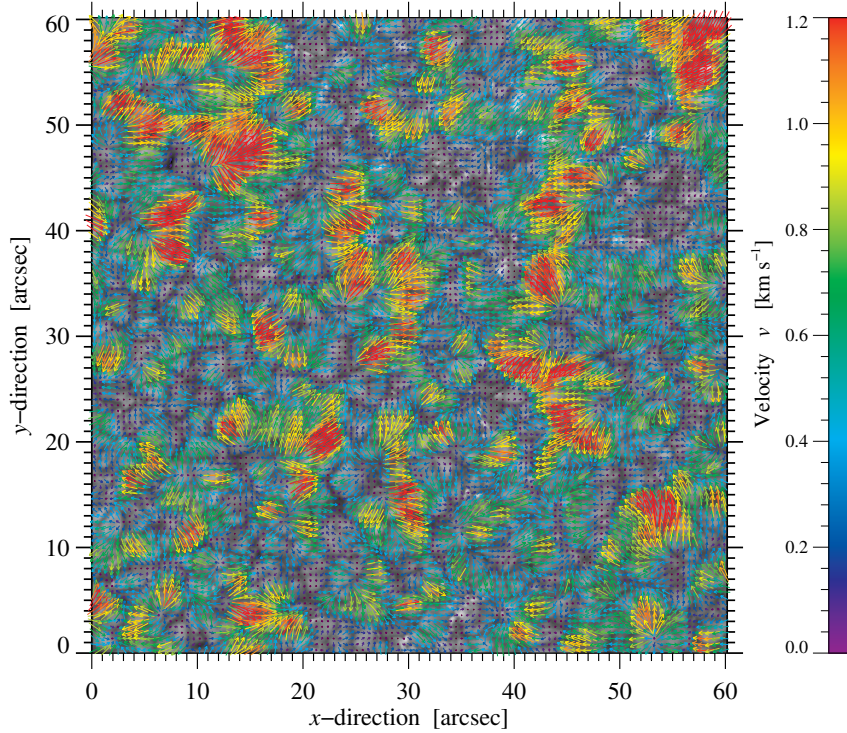


Figure 4.2: Results for LCT applied to the G-band images. The best G-band image of the time-series with overlying displacement vectors averaged over the whole time-series. The horizontal flow speed is color-coded, where the velocities are clipped at $v = 1.2 \text{ km s}^{-1}$. The FOV is $60'' \times 60''$.

the LCT algorithm we need a more or less coherent time-series without larger gaps. Therefore, we select the time-series between 16:52 UT and 17:58 UT. Unfortunately, this time-series still contains smaller gaps (cf. Fig. 3.4). In total, it contains 264 images, which includes also the images with the best MFGS values of the whole observation run. By watching the time-lapse movies we recognize strong image displacements between the images, maybe caused by the AO system not locking correctly on granulation. Thus, the first step preparing the image sequence for the LCT is to align the images. Therefore, we determine the global image motion vector. If the displacement vector of the image in one direction is greater than five pixels, the image is sorted out from the time-series. In addition, we calculate the standard deviation of the intensity in each image. Due to the granulation in the G-band images, we can assume that a standard deviation larger than 0.15 belongs to images which are over-reconstructed with MFBD and these images are sorted out as well. With this conditions we select 248 images for the further processing. These images are aligned taking into account the displacement vectors. We have border effects in the images, because of the alignment process and we have to extract the common of the image. The images shrink to 926×955 pixels. To remove the signal from the 5-minute oscillation (Ulrich, 1970) from the images, we apply a subsonic filter to the image sequence. Furthermore, we rotate the image by 180° and transpose the images in order to bring the images in the heliospheric coordinate system. Now, the upper right corner of the images are showing towards North (cf. Fig. 2.6). Most of the images in the time-series are separated in time by 11.8 s, but there are bigger gaps in between. For the LCT routine, we have to find image pairs of about the same separation, which is in our case 60 s. Therefore, we write a routine which selects the next image with a separation of about 60 s. If such a pair does not exist, other pairs separated in time between 20 s and 100 s are allowed but as close to 60 s as possible. In most cases we obtain image pairs with a separation of 58.9 s. These pairs of images as well as their temporal separation are the input parameters in the LCT algorithm. As described in Sect. 3.3 we have a kernel with the dimension of 48×48 pixels because of the small image-scale of $0''.069$. The LCT routine and the determined time interval between the images gives us the velocity vectors v_x and v_y in x - and y -direction, which are used to calculate the horizontal velocity vector

$$v = \sqrt{v_x^2 + v_y^2}. \quad (4.1)$$

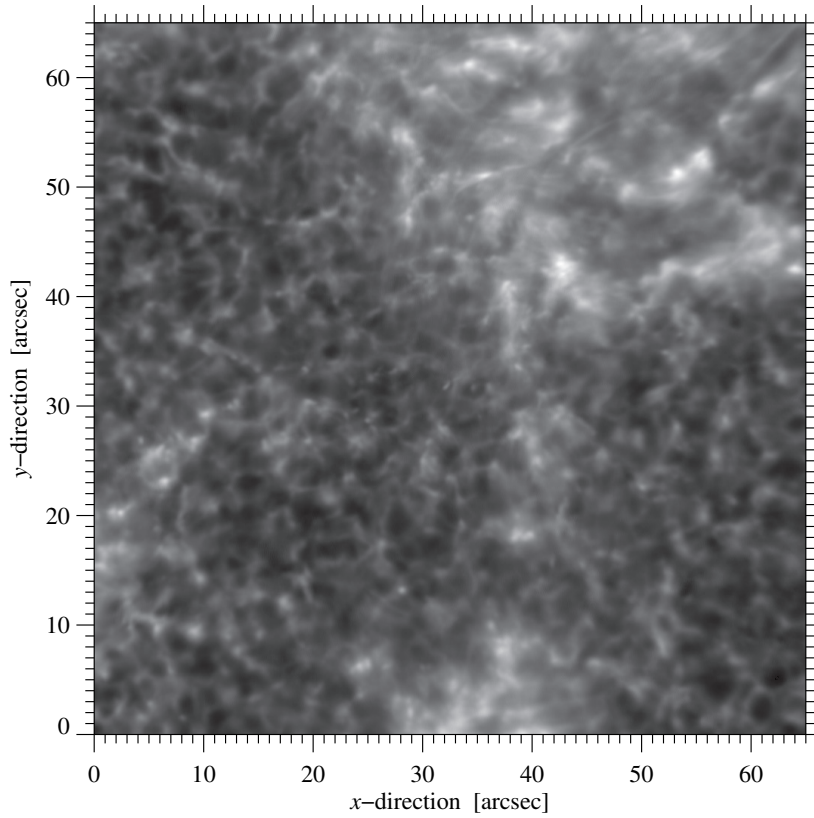


Figure 4.3: Best Ca II K image of the time-series at 17:21:34 UT on 2013 January 20 with a MFGS-value of 0.89. The image shows the upper photosphere and lower chromosphere of the Sun.

For the G-band images, we obtain a maximum horizontal flow speed of $v_{\max,g} = 1.80 \text{ km s}^{-1}$ and a mean flow speed of $v_{\text{mean},g} = 0.61 \text{ km s}^{-1}$ with a standard deviation $\sigma_v = 0.30 \text{ km s}^{-1}$, averaged over the time-series of 66 min.

Figure 4.2 contains the horizontal displacement vectors derived from LCT plotted over the best image of the time-series. The horizontal proper motions were averaged over the whole time-series of 66 min. For clarity the velocities are clipped at $v = 1.2 \text{ km s}^{-1}$. The photospheric mesogranulation with a diameter of $\sim 6 \text{ Mm}$ is reproduced by the horizontal velocity vectors in the map. The vectors originate in the diverging centers and are directed towards the border of the mesogranular cell. Some flows in the mesogranules reach relatively high flow speeds of over 1.2 km s^{-1} . Furthermore, in the upper part of the image at coordinates $(50''\text{--}60'', 30''\text{--}40'')$, there is a region containing bright points (see Fig. 4.1). At the location of these bright points, the LCT algorithm yields very low horizontal velocities. Bright points originate from strong magnetic field concentrations due to magnetic flux tubes anchored at that point and reaching in higher atmospheric layers. In Sect. 4.2.4 we discuss the relation of the bright points to the higher layers. In comparison to the low horizontal velocities at the location of the bright points, very high horizontal velocities are located in the upper right corner of the map, reaching the maximum value of up to 1.8 km s^{-1} . In the image parts of the penumbra are recognizable. The flows are connected with the moat flow of the sunspot, which is a divergent flow away from the sunspot (Stix, 2004). Such flows are reported around stable H spots, which we have also in this study.

4.2.2 Local Correlation Tracking on Ca II K Data

The target region seen in the Ca II K line (see Fig. 4.3) appears different compared to the photosphere in the G-band images. The Ca II K line shows the upper photosphere and chromosphere. The image contains an inverse granular pattern, but appearing with a dark core and a surrounding bright structure. Furthermore, the Ca II K line is sensitive to the magnetic field. The regions with a strong magnetic field appear as bright regions but without information about the polarity of the magnetic field. The upper part of the image between coordinates $(30''\text{--}64'', 40''\text{--}64'')$ is much brighter compared to the surrounding inverse granulation. In the upper right corner, where the sunspot is located, the strong magnetic field may be the cause for the brightenings. The bright region extends towards the lower part in a narrow strip at about the

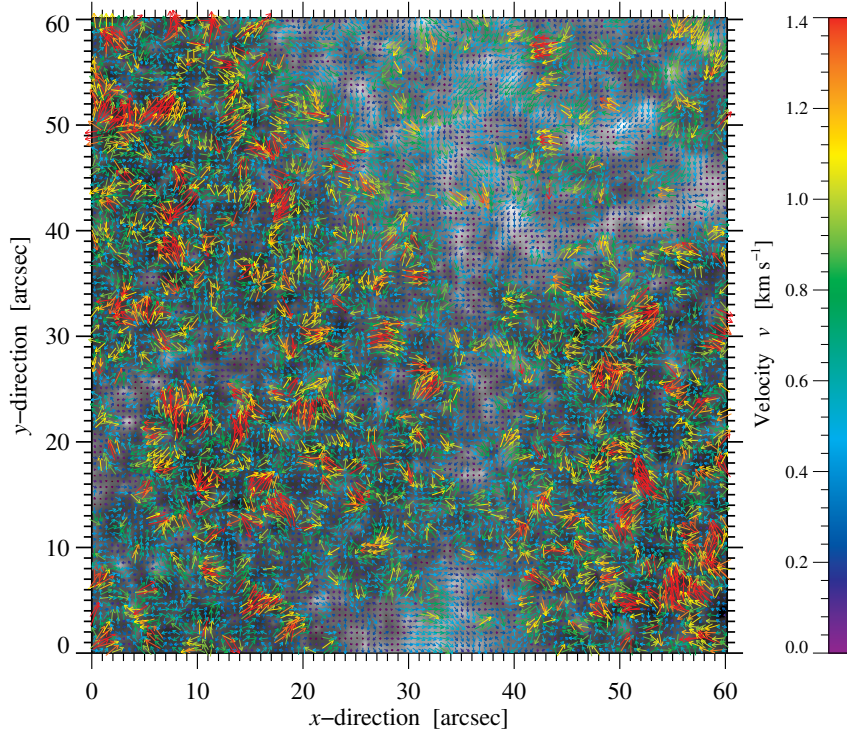


Figure 4.4: Results of local correlation tracking on the Ca II K line images. Best Ca II K image of the time-series with overlying displacement vectors averaged over the whole time-series. The horizontal velocity vectors are color-coded and clipped at a velocity of $v = 1.4 \text{ km s}^{-1}$. The image has a FOV of $60''2 \times 60''2$.

middle axis of the image. In the lower part between ($30''\text{--}45''$, $0''\text{--}10''$) we again have an extended bright region, showing a region of strong magnetic field.

For the analysis of horizontal proper motions in the Ca II K line images, we implemented the LCT algorithm in the same way as described for the G-band data. We had to start with some preparations of the time-series of Ca II K. We selected roughly the same time-series as for the G-band images on 2013 January 20 between 16:52 UT and 17:58 UT. The time sequence contains 107 images, where already eight images were discarded because of strong intensity fluctuations from the image restoration. For the remaining images we calculated the displacement vector. We sorted out images with a displacement of more than 10 pixels, which corresponds to images where the AO was not locking correctly. Furthermore, we sorted out images with a lower MFGS value than 0.77 and a standard deviation of more than 0.28, because here we have seen images, where the reconstruction of the image failed. The remaining 86 images have a FOV of 938×961 pixels after alignment. After applying the subsonic filter, we rotated and transposed the image to get the same orientation as the G-band images. Most of the images are separated in time by 26.5 s. This time-series also contains small gaps. Again we have to find image pairs with a temporal separation close to 60 s. We selected 79 pairs with roughly a cadence of 53.0 s. We obtain for the Ca II K time-series averaged over 66 min a maximum horizontal flow speed of $v_{\text{max,g}} = 3.28 \text{ km s}^{-1}$ and a mean flow speed of $v_{\text{mean,g}} = 0.71 \text{ km s}^{-1}$ with a standard deviation of $\sigma_v = 0.40 \text{ km s}^{-1}$.

We present the results of LCT in Fig. 4.4, where the derived horizontal velocity vectors are plotted over the best image of the time-series. In parts of the inverse granulation patterns divergent flows are encountered leaving a central point towards the borders of the structure, similar to the G-band images (Fig. 4.2). Furthermore, in the bright regions, where the magnetic field is strong the tracked horizontal flow speeds are nearly zero or very small. These regions have approximately the same location as the G-band bright points. The relation of the G-band bright points to the other atmospheric layers will be discussed in Sect. 4.2.4. In the upper right corner, we again see strong horizontal velocities coming from the direction of the sunspot towards the FOV. These horizontal flows are following the bright structures in that part of the image. If these horizontal flows are supporting the filament with plasma, it has to be discussed in the flowing sections.

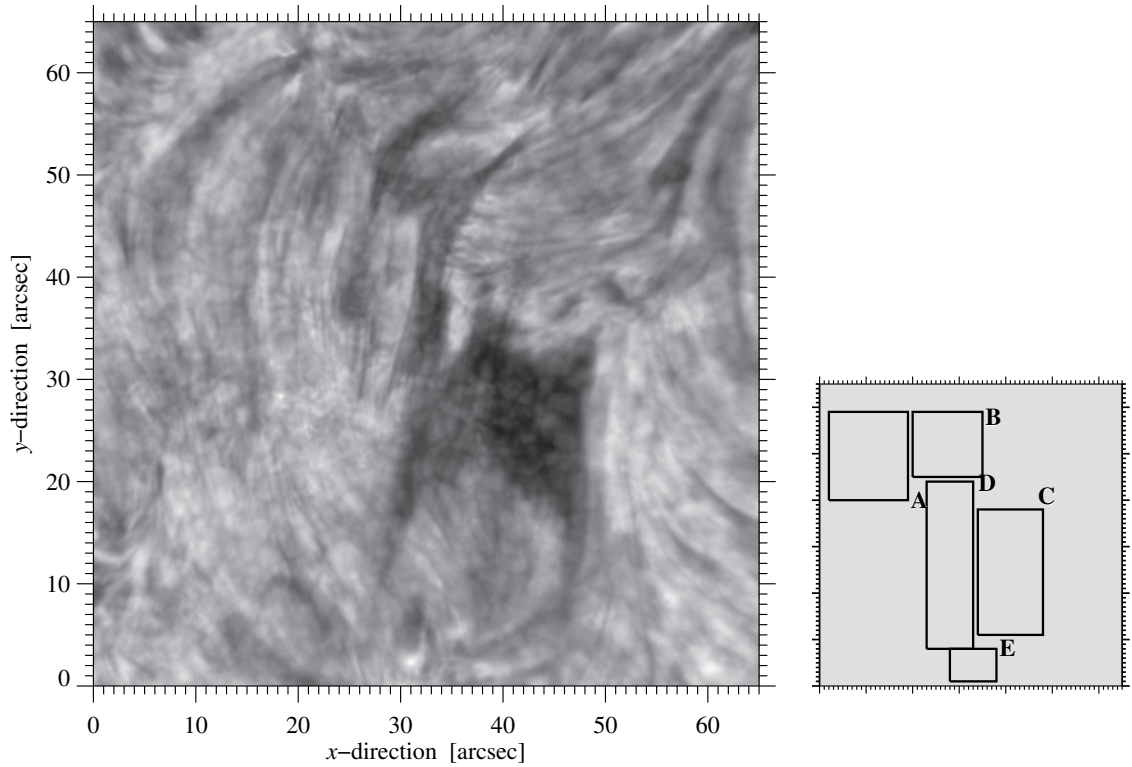


Figure 4.5: Best $H\beta$ image of the time-series at 17:21:22 UT on 2013 January 20 with a MFGS-value of 0.74. The $H\beta$ image shows the chromosphere containing the patchy filament. In the small image the regions of the $H\beta$ image are marked, which will be mentioned in more detail.

4.2.3 Local Correlation Tracking on $H\beta$ Data

Finally, the $H\beta$ images show the chromosphere (see Fig. 4.5), where the plasma of the active region filament is located. The whole image shows filamentary structures belonging to the surrounding fibrils. In the middle of the image in region C (Fig. 4.5) a dark structure is located, i.e., the active region filament. This filament has not the classical elongated appearance but possesses a more clumpy structure. At the left side of the filament in region C, there is a more elongated structure (region D), which may also be connected with the dark structures coming from the upper right corner, the extended superpenumbra (Peter, 1996; Stix, 2004) of the sunspot. Watching the time-lapse movie of the $H\beta$ images, we get the impression that the filament is filled with plasma supplied by the superpenumbra of the sunspot. The filamentary structures in regions C and D separate during observations. Both filaments in regions C and D are connected with the parts of the superpenumbra and region E. Furthermore, the images exhibit signatures of the granulation, which may result because of a too broad interference filter mixing photospheric with chromospheric structures. In the upper left corner we identify in the time-lapse movies a region with a swaying motion (region A). This swaying motions have a period of roughly 30 min. The exact period is difficult to measure, because of the gaps in the time-series. Region B contains a dark structure, which is moving bodily down towards the main body of the filament. The time-lapse movies show that this structure connects towards the end of the time-series with the brighter parts in region E. In the end we have three clearly separated filaments in regions B, C, and D, all connected with region E and the superpenumbra of the sunspot. The connection with the superpenumbra still has to be verified by determining both, horizontal and LOS velocities. The LOS velocities are later determined in Sect. 4.3.1 for the $H\alpha$ data set.

We validate the motions in the time-lapse movie with the horizontal velocity vector map derived with LCT. Therefore, we have to prepare the images of the time-series. We select images from the same time range between 16:52 UT and 17:58 UT. These are 122 images, where 20 images are dropped because of strong intensity fluctuations resulting from the MFBD image reconstruction. From the image sequence we select 106 images with displacement vectors smaller than 10 pixels, corresponding to a working AO.

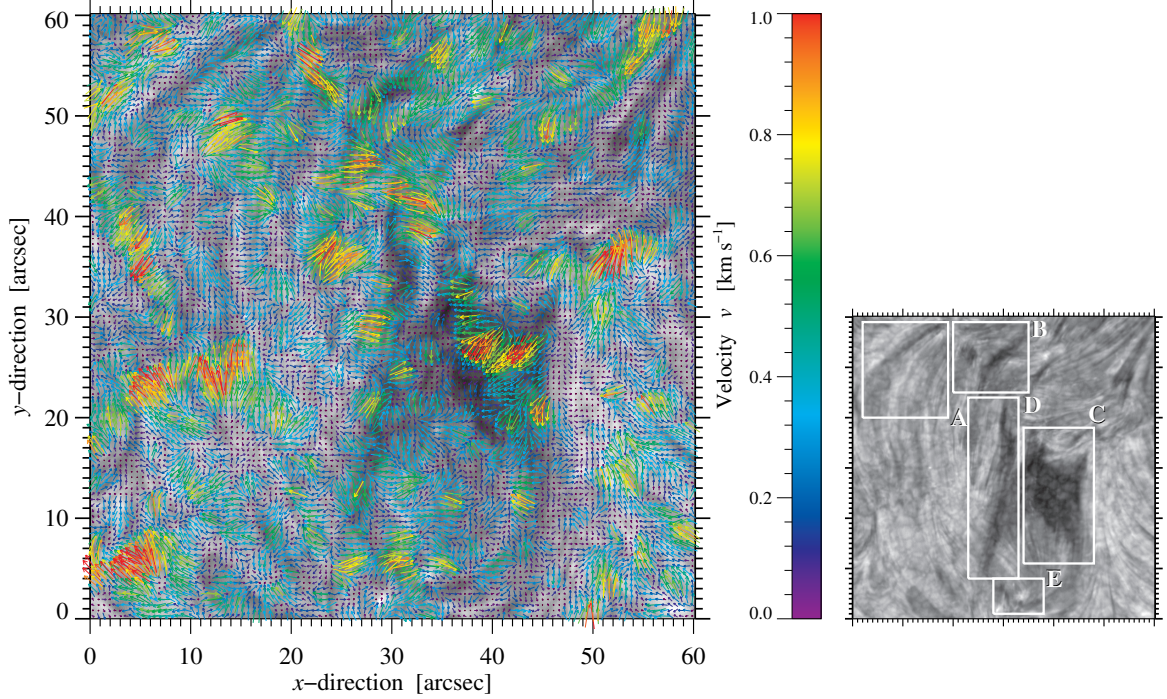


Figure 4.6: Results of LCT applied to $H\beta$ images. Best $H\beta$ image of the time-series with overlying displacement vectors averaged over the whole time-series of 66 min. The velocities are color-coded and clipped at a horizontal flow speed of $v = 1.0 \text{ km s}^{-1}$. The image has a FOV of $60'' \times 60''$. In the small image the regions of the $H\beta$ image are marked, which will be mentioned in more detail.

By aligning the images the FOV reduces to 922×960 pixels. After applying the subsonic filter, we rotate and transpose the images so that we have in the end 106 images. We find 104 pairs with most of the pairs separated by 58.9 s. Afterwards, we start the LCT algorithm. The LCT algorithm averaged over the whole time sequence of 66 min in $H\beta$ gives a maximum flow speed of $v_{\text{max,g}} = 2.24 \text{ km s}^{-1}$ and a mean flow speed of $v_{\text{mean,g}} = 0.39 \text{ km s}^{-1}$ with a standard deviation $\sigma_v = 0.21 \text{ km s}^{-1}$.

In Fig. 4.6 we present the resulting horizontal velocity vectors plotted over the underlying best image of the time-series. The vectors are color-coded and the velocities are clipped at $v = 1.0 \text{ km s}^{-1}$. The tracked horizontal flows are located along the filamentary structures in the chromosphere. In the upper right corner there are strong velocities along the structures of the superpenumbra of the sunspot. These horizontal flows point towards the dark structures of the filament and could show how the filament is filled with plasma supplied by the sunspot. This assumption has to be proofed with the corresponding LOS velocities in this region. In region C there is the clumpy filament, which contains a region of strong horizontal flows directed towards the lower left corner of the region. Beneath the location of strong flow speeds in region C there is a region of very small horizontal flow speeds. Comparing this region with the other layers shows that at this location in all three layers the flow speed is very low. Maybe the LOS velocity maps can resolve the reasons for the low flow speeds. Furthermore, the right branch of the filament structure contains flows directed to the region E. Also the structure in region D shows horizontal flows ending in region E as already seen in the time-lapse movies. In the Ca II K image, at that location there is a bright structure, which is related to stronger magnetic field. As mentioned before, the three distinguished filaments in the end of the time-series are all ending at that point. If region E is related to a footpoint region, has to be verified with magnetic field data of IBIS or HMI. We will discuss this region in more detail in Sects. 4.2.4 and 4.3.3. Furthermore, in the time-lapse movies the dark structure in region B moved towards the main filament structure, which is also tracked in the velocity maps of LCT. The flow speeds in this region reach values of up to $v = 1.0 \text{ km s}^{-1}$ towards the elongated filament structures in region D. In the region A, the region of the swaying motions, nearly no horizontal flow speeds are measured. This result is expected because of the averaging of flows over the time-series. The individual

Table 4.1: Comparison of velocities in different wavelength: the maximum velocity v_{\max} and the mean velocity v_{mean} with its standard deviation σ_v .

Wavelength	maximum velocity	mean velocity	standard deviation
	v_{\max} in km s^{-1}	v_{mean} in km s^{-1}	σ_v in km s^{-1}
G-Band	1.80	0.61	0.30
H β	2.24	0.39	0.21
Ca II K line core	3.28	0.71	0.40

velocities of the oscillating structure are averaged and not any longer trackable. Furthermore, there are strong flow speeds along the upper border of the dark structure in region A. The source of this flows lies outside of the FOV.

To understand the horizontal flows tracked in the different atmospheric layers we have to compare the results among each other. Furthermore, we will need information about the LOS velocities the connection between the superpenumbra and the filament. The LOS velocities will be extracted from spectroscopic IBIS data. In addition, IBIS data contain magnetic field information of the chromosphere from the polarimetric measurements. The magnetograms from IBIS will help to identify the locations of footpoints, where filament feet terminate, even though this might be difficult for this type of active region filament with a clumpy appearance. The footpoints help to understand the connection between the filament's plasma in the chromosphere and how the filament is connected with the lower atmospheric layers.

4.2.4 Comparison and Discussion of ROSA Results

We applied LCT to the images of the different atmospheric layers and reproduced typical structures of these layers. In the G-band images, the expected granulation is visible in the horizontal velocity maps, and in the H β images the flows are tracked along the filamentary structure of the chromosphere. Comparing the overall horizontal proper motions in the different atmospheric layers we find that the highest values are detected in the Ca II K line images with a maximum velocity for the averaged LCT map of $v_{\max, \text{Ca}} = 3.28 \text{ km s}^{-1}$. In addition, the mean value is higher than for the other two lines with $v_{\text{mean, Ca}} = 0.71 \text{ km s}^{-1}$ and $\sigma_v = 0.45 \text{ km s}^{-1}$. In H β high horizontal velocities reach values of up to $v_{\max, \text{H}\beta} = 2.24 \text{ km s}^{-1}$. The mean velocities are lower compared to the other two lines with $v_{\text{mean, H}\beta} = 0.39 \text{ km s}^{-1}$ and $\sigma_v = 0.23 \text{ km s}^{-1}$. In the Fraunhofer G-band the lowest values for the maximum velocity is tracked with $v_{\max, \text{G-band}} = 1.80 \text{ km s}^{-1}$ and a mean velocity of $v_{\text{mean, G-band}} = 0.61 \text{ km s}^{-1}$ and $\sigma_v = 0.34 \text{ km s}^{-1}$, which is slightly higher than for H β . The higher velocities in H β belong to structures of the filament. In all three layers, different matter is tracked. Whereas we track in G-band the photospheric plasma moved around in the form of granules, we track in H β the cool plasma directly related to the filament, which is suspended by the magnetic field above the photosphere. In the LCT maps the influence of the sunspot on the region of the filament is seen, caused by the strong flow field originating from the sunspot, which is directed towards the location of the filament. In the H β images, conspicuous flows are tracked along the filamentary structures connecting the filament and the sunspot. We suppose, that the filament is supplied with plasma from the sunspot via this connection.

We will now present a detailed view of the regions with bright points in the G-band and the same regions in the other layers. Comparing these regions, we investigate if certain bright points in the G-band are connected to footpoints of the filament. At the location of the bright points in the G-band images only low horizontal flow speeds or no horizontal flows at all were tracked by LCT. The Ca II K line images contain regions with very low horizontal velocities, which appear bright in the images and where we know, that they are connected with strong magnetic field concentrations. To visualize possible connections of the bright points with higher atmospheric layers, we create a mask in which the bright points are separated and plot the location of the bright points in the images of all three layers (see Fig. 4.7). Thereby, we matched the FOVs of ROSA and IBIS images concentrating on the region of the filament. Comparing the locations of bright points in the G-band with strong magnetic field concentrations in the Ca II K line

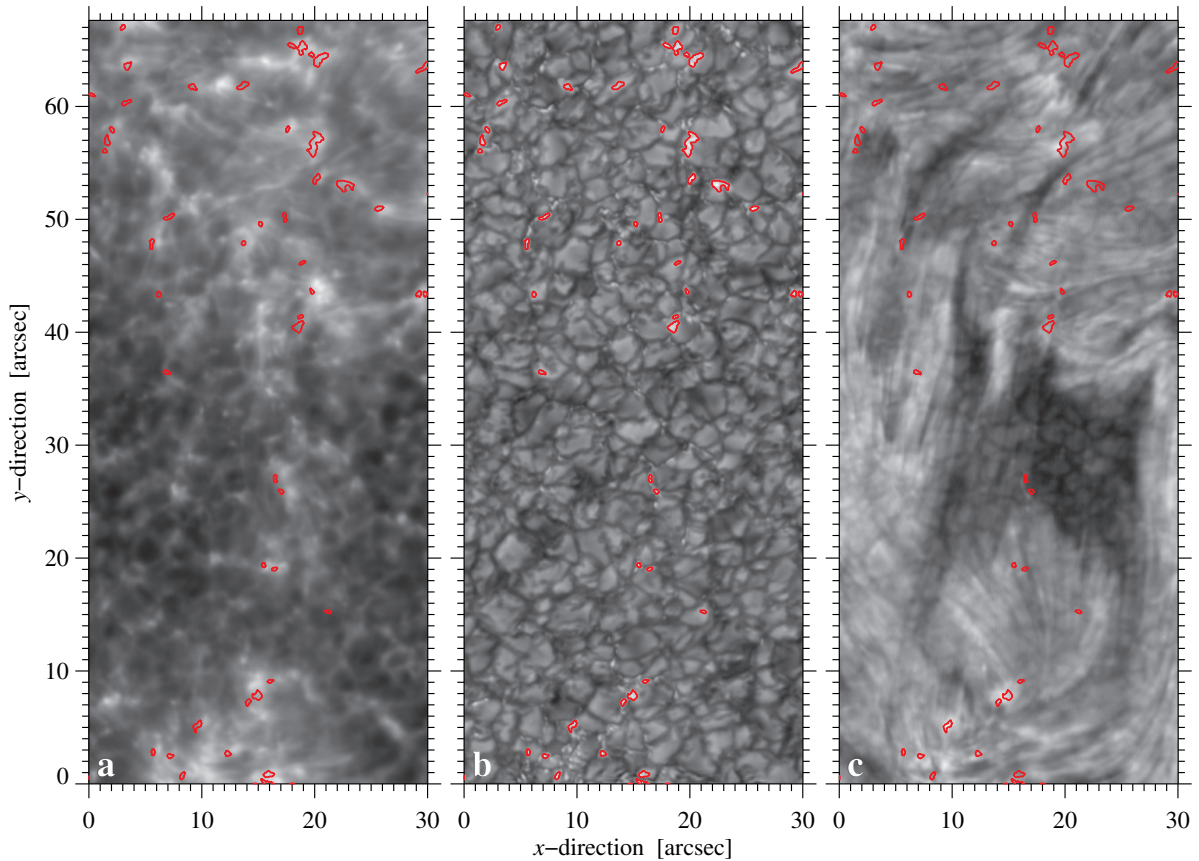


Figure 4.7: Identification and visualizing G-band bright points in ROSA data. We select the region containing the filament in the $H\beta$ images at 17:21 UT on 2013 January 20. The locations of the bright points are shown as red contour in (a) Ca II K, (b) G-band, and (c) $H\beta$ images. The FOV matches the IBIS observations.

(Fig. 4.7a), we recognize that they are well matched, which confirms that bright points also appear at locations of strong magnetic flux as described in Sect. 1.2.1. They are thought to be the footpoints of magnetic loops reaching up into the corona (Rimmele, 2004). In order to proof this, we inspect higher atmospheric layers and also investigate possible connections to the filament. Therefore, we examine Fig. 4.7c, in which the $H\beta$ image with the overlying G-band bright points is presented. The upper part of the image at coordinates ($15''$ – $25''$, $60''$ – $67''$) reveals a brighter region in $H\beta$. The dark structures of the filament seem to end at this bright area, which presumably are the footpoints. At the same location G-band bright points and strong magnetic flux concentrations in the Ca II K images are present (Fig. 4.7a). This would indicate, that this bright region in $H\beta$ is related to footpoints. Furthermore, in the lower part of the image, we have the same condition at coordinates ($5''$ – $20''$, $0''$ – $10''$). The dark structures of the filament end in this region and also the bright points in G-band and strong magnetic field concentration in the Ca II K line are present. To finally proof this assumption, we need magnetograms, which show the polarity of the magnetic flux concentration. If the mixed polarities at this location are present, then footpoints of filamentary structures are the most likely explanation (Kuckein, Verma, and Denker, 2016). We will continue the discussion of the footpoints with the IBIS data, where we obtain information about LOS velocities and from the spectropolarimetric data about the polarity of the magnetic field.

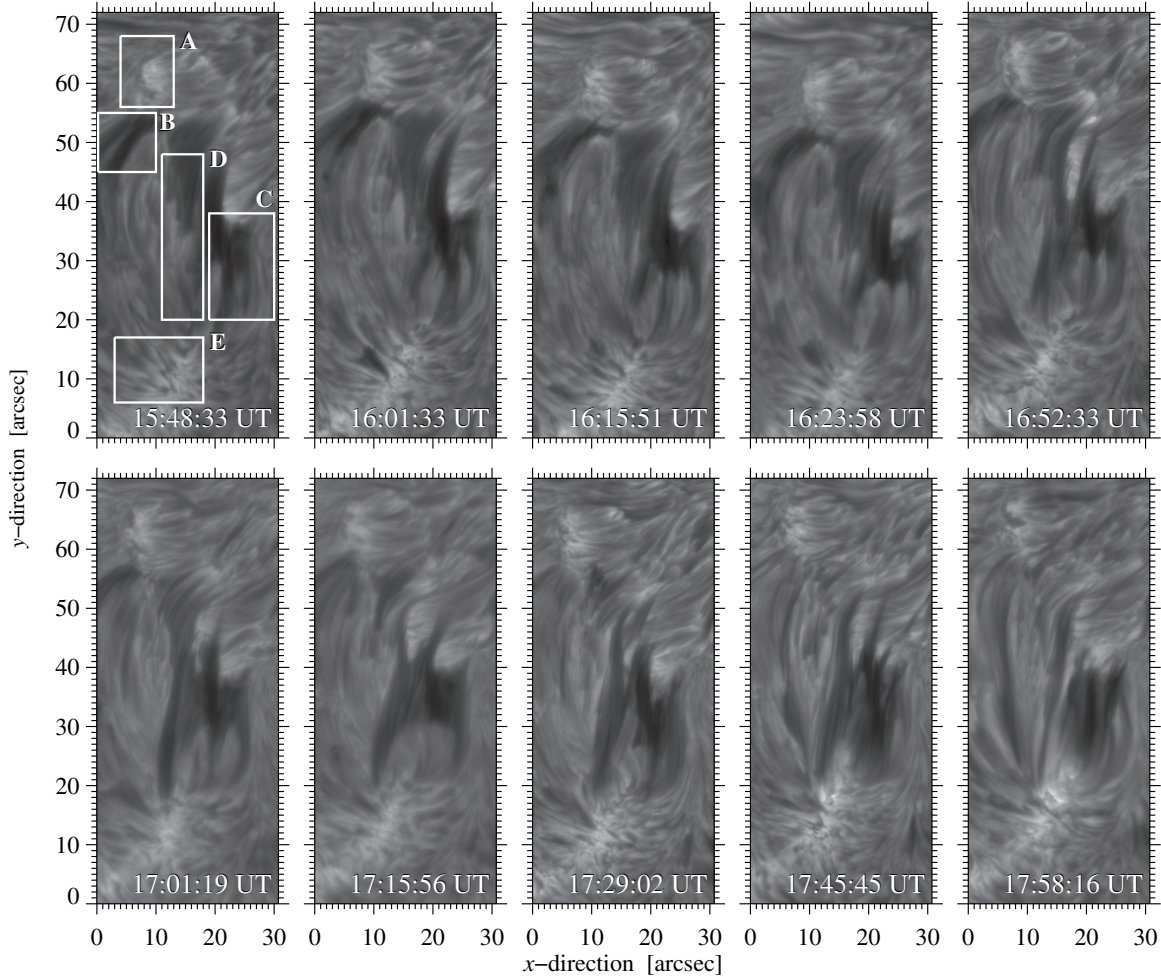


Figure 4.8: Temporal evolution of the filament in the chromosphere seen in selected $H\alpha$ line-core images for a two hour time-series starting at 15:48 UT on 2013 January 20.

4.3 Results from the IBIS Data Set

By analyzing the IBIS data we concentrated on narrow-band data, which contains spectroscopic $H\alpha$ and spectropolarimetric $\text{Ca II } \lambda 8542 \text{ \AA}$ observations. We will first examine the temporal evolution of the time-series before we analyze spectroscopic observations of both spectral lines determining LOS velocities, line-core intensities, and the contrast distribution in the images. In the end, we will briefly introduce IBIS magnetograms and compare them with HMI data.

4.3.1 Spectroscopic Data of the $H\alpha$ Line

We start with the analysis of the spectroscopic $H\alpha$ data set, which shows the chromosphere with the active region filament. First of all, we examine the temporal evolution of the filament during the observations from 15:48 – 17:58 UT. For this purpose, we create time-lapse movies for the whole time series of two hours for the $H\alpha$ line-core image ($\lambda_0 = 6562.81 \text{ \AA}$). Thereby, we aligned the images to remove differential image motion. In Fig. 4.8 we show ten selected points in time (approximately 15 min apart) to get an impression of the evolution of the filament. In the first image at 15:48:33 UT we labeled five regions, which we inspect concerning their temporal evolution. First of all, we examine the two regions with bright features labeled with A and E. Comparing these regions with the ROSA data, these are the same regions, where the bright points in the G-band data are located and which are candidates for the location of the filament’s footpoints. Later, we will discuss these footpoints in detail. Furthermore, in region C there is the dominant dark structure of the clumpy filament, which is also present in the $H\beta$ images of ROSA. At the beginning of the time-series the clumpy structure extends into the neighboring region D.

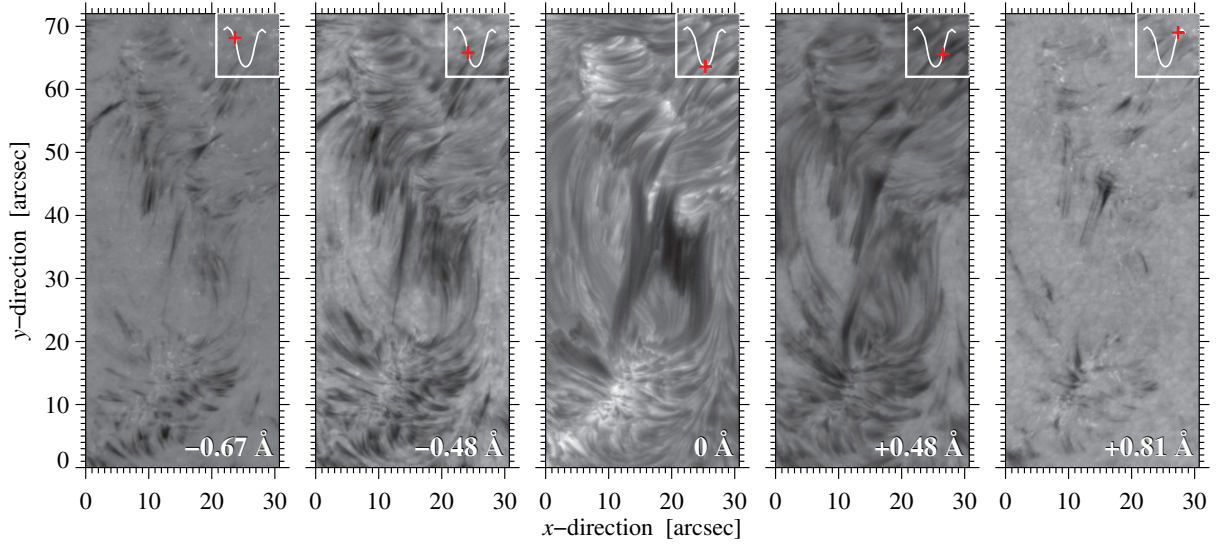


Figure 4.9: Line scan of best $H\alpha$ image-series at 17:22:08 UT with a size of $30''.7 \times 72''.0$. The scans include the line-wing positions $H\alpha - 0.67 \text{ \AA}$, $H\alpha \pm 0.48 \text{ \AA}$, and $H\alpha + 0.81 \text{ \AA}$ apart and the line-core image ($\lambda_{\text{cwl}} = 6562.85 \text{ \AA}$).

Furthermore, in region B there is a dark structure, which likely belongs to a filament. Furthermore, the rest of the image contains fibrils, the most conspicuous structure in $H\alpha$ images. In the time-lapse movies plasma in region A moves towards region E, passing both, region C and D, where we suppose a second loop from region B to region E going out of the image's FOV. In the movies, the structures of region D and E are more and more separated and another loop builds up from region D to region E (visible between 16:15:51 UT to 17:45:45 UT in Fig. 4.8). Thereby the clumpy structure first extends in size until it reaches a maximum at around 17:15:56 UT. Then the separation is visible in Fig. 4.8 until the filaments in regions C and D are completely separated as seen at 17:58:16 UT. Furthermore, the bright structures at the upper border of region C shimmer through from atmospheric layers of the clumpy filament (see Fig. 4.8 at 17:29:02 UT). In the end, it appears as if the main filament from region C is connected to these bright features instead to the bright features in region A. However, all filament structures are connected to region E. Likewise, region B evolves during the two-hour time-series. Here, the structure moves towards the visible part of the FOV. These motions were tracked with LCT in ROSA $H\beta$ data. Here, a filament structure builds up which connects regions A and E. Towards the end of the time-series three clearly defined and separated filaments formed, where one of them is the dominant clumpy structure and the other two have an elongated, more classical shape of a filament. The time-lapse movies show that the evolution of the active region filament is extremely fast and only within the short period of two hours the appearance of the filament changed significantly.

The spectroscopic data set contains series of scans through the spectral line of $H\alpha$ reaching from $6561.46 \text{ \AA} - 6564.14 \text{ \AA}$. The steps between the scans are non-equidistant; the step size towards the line core is decreasing with the smallest step size of 0.04 \AA around the line core. In Fig. 4.9 we present images of the best time-series based on the MFGS values for $H\alpha$ data at 17:22:08 UT. We show the scan through the $H\alpha$ line with images at $H\alpha - 0.67 \text{ \AA}$, $H\alpha \pm 0.48 \text{ \AA}$, and $H\alpha + 0.81 \text{ \AA}$ relative to the line core of $H\alpha$ ($\lambda_{\text{cwl}} = 6562.85 \text{ \AA}$). The images are extracted from the original FOV to get rectangular images. These images have 384×900 pixels, which corresponds to a FOV of $30''.7 \times 72''.0$. Historically, it is common to present scans through the $H\alpha$ line at positions $H\alpha \pm 0.5 \text{ \AA}$ and $H\alpha \pm 0.75 \text{ \AA}$. We tried to find positions in the scan close to these values, but unfortunately due to the non-equidistant grid, we have scans at the positions $H\alpha - 0.67 \text{ \AA}$ and $H\alpha + 0.81 \text{ \AA}$, as well as at $H\alpha \pm 0.48 \text{ \AA}$. At the location $H\alpha \pm 0.75 \text{ \AA}$, chromospheric features such as mottles were discovered. By having a look into our data set the structures in $H\alpha - 0.67 \text{ \AA}$ could be related to mottles (Fig. 4.9). In $H\alpha + 0.81 \text{ \AA}$ the structures are too faint to associate them with mottles. Furthermore, there are brightenings in both images at the locations of the footpoint candidates (regions A and E in Fig. 4.8). These images show the atmospheric layer located lower than the $H\alpha$ core, i.e., closer to the photosphere. In the images at $H\alpha \pm 0.48 \text{ \AA}$ more and more filamentary structure becomes visible (Fig. 4.9). Especially, the elongated dark structure is conspicuous, which is

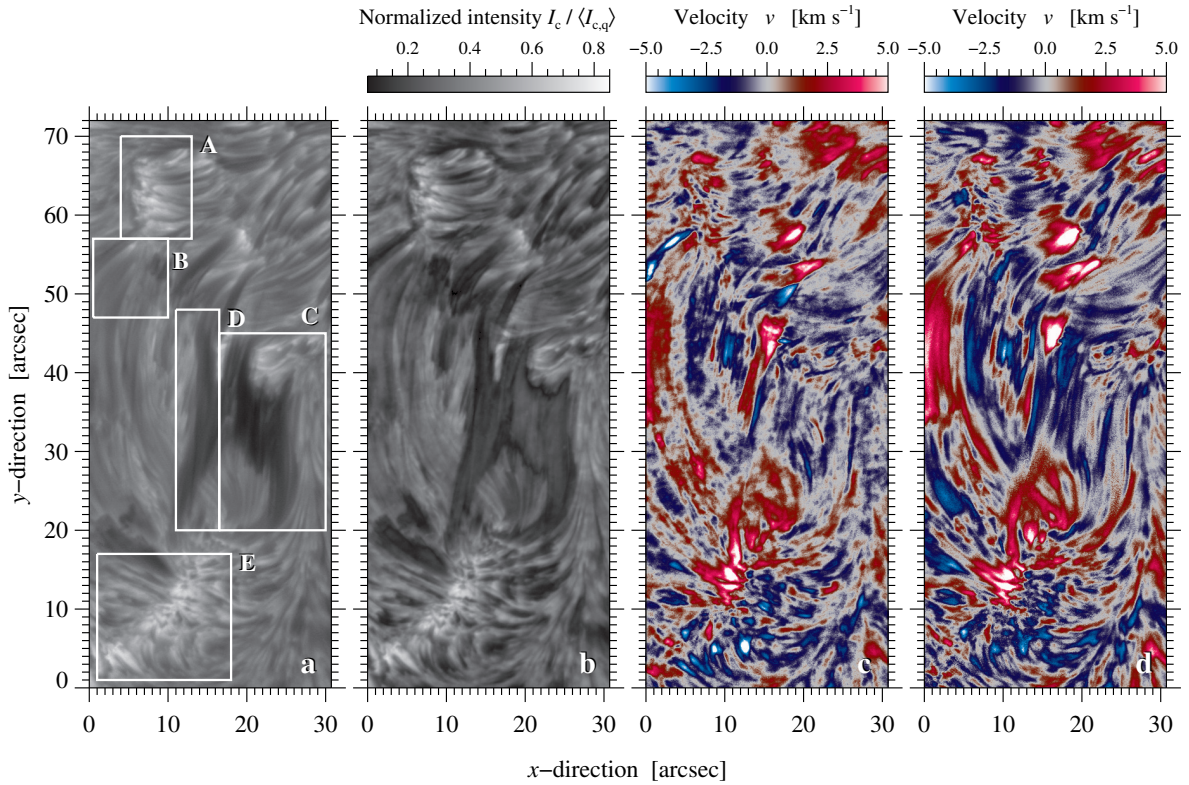


Figure 4.10: Physical maps for $H\alpha$ data at 17:22:08 UT: (a) line-core intensity and five labeled regions, (b) contrast map, (c) Doppler velocity derived from Fourier phase method, and (d) Doppler velocity derived with line-core fitting. Both velocity maps are clipped at $\pm 5 \text{ km s}^{-1}$ and the white regions denote saturated values.

likely related to the filament of region D in Fig. 4.8. In Fig. 4.9, this structure is better visible than the main clumpy filament. However, this scan shows an atmospheric layer lower than the formation height of the $H\alpha$ line core. In the regions $H\alpha + 0.48 \text{ \AA}$ and $H\alpha - 0.48 \text{ \AA}$ this structure appears different, which indicates that they are not showing the same atmospheric layer.

The next step in the analysis is to use the spectral data we have for each pixel in the image. Therefore, we create several maps, which will be analyzed concerning their physical properties. We create maps for each image of the time-series and produce the corresponding time-lapse movies. In Fig. 4.10 we show the maps derived from the best time-series at 17:22:08 UT. In the following, we will introduce each map in detail and compare them with the other physical maps of the time-series. Note, that all spectral profiles in the data cube are divided by the prefilter curve, which is introduced in Sect. 3.2.3.

We start with the line-core intensity, which is derived from the minimum of each spectral profile. In comparison, the line-core image contains the profiles at the same position of the spectrum at λ_{cwl} (cf. Fig. 4.8). A parabolic fit to the line core yields both the line-core intensity and position, which in turn corresponds to a Doppler velocity. Beforehand, the spectrum was interpolated to an equidistant grid with a step size corresponding to the smallest interval of the grid of 0.04 \AA , which has the effect, that we obtain 68 wavelength points instead of the original 25 of the non-equidistant grid. This equidistant grid simplifies the calculation of the LOS velocity. Figure 4.10a contains the line-core intensity map for the time-series. The overall visual impression of the image is very similar to the line-core image but differs in some regions, for example, in the upper part of region D, where dark loop structures connect with bright regions. The differences are caused by different positions of the minimum of the spectral line compared to the line-core image.

The next physical map is based on the contrast profile. In the contrast profile, we compare each pixel of the image with the profile of the quiet Sun. Therefore, we have to calculate first the profile of the quiet Sun. All bright and dark structures are discarded in the image, such as the dark filament structures and the bright structures of regions A and E. Furthermore, we neglect all parts with LOS velocities larger than $\pm 2 \text{ km s}^{-1}$. How to calculate the LOS velocities is described in the next paragraph. In the following, we average all pixels of the quiet-Sun mask in order to gain the quiet-Sun profile I_0 . We calculate the contrast

profile I_c for each pixel by first subtracting and then dividing by the quiet-Sun profile

$$I_c = \frac{1}{\lambda_k} \sum_{\lambda_k} \left| \frac{I(\lambda_k) - I_0}{I_0} \right|. \quad (4.2)$$

After subtracting the quiet-Sun profile, the norm is taken to ensure positive values. The mean value over the k wavelength points of the resulting profile is selected for the contrast map. The resulting map for the contrast profile is shown in Fig. 4.10b. This map reveals the most prominent absorption features. The filament in regions B, C, and D is much more distinct compared to the quiet-Sun background with its fibrils. Also the bright regions A and E are much clearer in the contrast map. The contrast profile is used for the Cloud Model (Beckers, 1964; Mein and Mein, 1988; Chae, 2014; González Manrique, Bello González, and Denker, 2016). The basic concept of the cloud model is to assume the filament as a cloud hanging in the chromosphere and blocking the emitted radiation of the underlying photospheric plasma. Applying the cloud model to the data yields four parameters, i.e., the LOS velocity, the Doppler width, the source function, and the optical thickness, whereby we have to assume, that these parameter are constant along the LOS. Using the cloud model on the IBIS data is beyond the scope of this thesis and will be applied later in a forthcoming peer-reviewed publication.

Finally, we will calculate the LOS velocities in the IBIS images in two different ways. The first method, we are using to calculate the LOS velocities is the Fourier phase method in which the phase angle of the Fourier transform is calculated to get the position of the minimum of the spectral line

$$\Phi(I) = \arctan \left[\frac{\Im\{\mathcal{F}(I)\}}{\Re\{\mathcal{F}(I)\}} \right], \quad (4.3)$$

where I is the spectral profiles and $\Im\{\mathcal{F}(I)\}$ and $\Re\{\mathcal{F}(I)\}$ denote the imaginary and real part of the Fourier transform $\mathcal{F}(I)$ (Gonzalez, Woods, and Eddins, 2009). This method is very fast and insensitive to noise. The angle is translated into a position on the wavelength grid. From the position on the grid p_c for each pixel of the image, we calculate the Doppler velocity. To determine the reference wavelength λ_0 we fit for each image a second-order polynomial to the line core of the quiet-Sun profile. For the sample image $\lambda_0 = 6562.86 \text{ \AA}$. In comparison, the line-core image is at the wavelength position $\lambda_{\text{core}} = 6562.85 \text{ \AA}$. In literature, the line-core position of the quiet-Sun H α line is $\lambda_{0,\text{ref}} = 6562.81 \text{ \AA}$ (Moore *et al.*, 1966). The central position p_c is first shifted by the mean value of the array to get the shift compared to the line center. Afterwards, we multiply the position with the step size or dispersion d : $p_c \cdot d \hat{=} \Delta\lambda$. The velocity is then calculated concerning the Doppler law in Eq. (3.11):

$$v = p_c \cdot \frac{d}{\lambda_0} \cdot c, \quad (4.4)$$

where c is the speed of light. As we have seen in Sect. 3.3.2, the LOS velocity is strongly depending on the definition of the reference wavelength λ_0 . The result of the LOS velocities, calculated for each pixel of the image is shown in the map in Fig. 4.10c. The decreasing wavelength positions, a blue-shift, indicate up-flows, which result into negative Doppler velocities (Mein, 1992). Redshifted positions correspond to down-flows. on the disk flow] The map is clipped between $\pm 5 \text{ km s}^{-1}$ to improve the clarity. Saturated values on both sides are indicated in white. Inspecting the Doppler velocity map at 17:22:08 UT, strong down-flows occur in the upper right corner from the direction of the sunspot, where the superpenumbra is located. Furthermore, we have down-flows in region A, where we tentatively locate the footpoints of the filament. In region B on the other hand, there is a strong up-flow, followed by strong down-flows towards region E. In addition to the strong down-flows in region E, a strong up-flow appears on the lower right part of this region. At the location, where we suspect, that loop B has its footpoints in region E, there are also strong down-flows located. Furthermore, in the upper half of region D, there are strong down-flows, but parallel to this there are also down-flows. At the location of region C, where the clumpy filament part is located, there are no strong up- or down-flows, but weaker flows, mainly up-flows. In general up-flows dominate, which reach LOS velocities of $v_{\text{up}} = -7.5 \text{ km s}^{-1}$, but down-flows of the same order exist as well. The mean LOS velocity in the FOV is close to zero. By inspecting the time-laps movies of the Doppler velocity maps for the entire two hours time-series, we see a continuous down-flows from the sunspot in the upper right corner and in region A. The strong down-flow in region B just developed at

around the 17:20 UT, i.e., after a period of were much weaker up-flows. In region D we encounter an interplay of both, up- and down-flows over the whole time-series, mainly parallel to each other. In the end the down-flows are more dominant in this region. On the other side, between region B and D, where a new filament is developing, we see both strong up- and down-flows, where in the end the up-flows are dominating. The most interesting region is region E, where the strong down-flows are located. At the end of the time-series, starting at around 17:30 UT, the down-flows are clearly dominating the whole region with down-flows of up to 18 km s^{-1} . The region extends to coordinates of ($9''-23''$, $17''-35''$). In region C there are strong up-flows. In the end, when the structures of region D and C appear to separate, strong up-flows develop in this region.

The second method to calculate LOS velocities relies on fits to the line core of the spectrum, thus calculating the minimum position in the spectrum. For this purpose, we fit a second-order polynomial to a region of $\pm 0.36 \text{ \AA}$ around the line core: $I(\lambda) = a_0 + a_1 \cdot \lambda + a_2 \cdot \lambda^2$, where a_i are constant values resulting from the least-squares. The vertex of the fitted parabolic curve is then defined with $\lambda_c = -0.5a_1/a_2$. With the central wavelength position λ_c of this spectral line we calculate the shift with respect to the central wavelength λ_0 of the quiet-Sun profile and derive the velocity as described in Eq. (4.4). The resulting map is shown in Fig. 4.10d. The map is clipped between $\pm 5 \text{ km s}^{-1}$. The general shape is similar to the LOS velocity map derived from the Fourier method (Fig. 4.10c) but both maps differ in detail. The overall impression is that the map is much smoother, compared to the velocity map from the Fourier method. Comparing both maps, the strong up-flow in region B is only faintly visible in Fig. 4.10d. Furthermore, above region D the down-flow regions are more extended with higher velocities, which we see in the more saturated appearance of the regions. In total, the down-flows reach values in this map of up to $v_{\text{down}} = 9.9 \text{ km s}^{-1}$ and the up-flows of $v_{\text{up}} = -5.2 \text{ km s}^{-1}$, where the mean velocity is again close to zero. The temporal evolution during the two-hour time-lapse movies exhibits the same characteristic processes as for the Fourier method but with differences in the details.

4.3.2 Spectropolarimetric Data of the Infrared Calcium Line

The infrared Ca II $\lambda 8542 \text{ \AA}$ is, as well as the Ca II K line, sensitive to the magnetic field. This means, that strong magnetic-field concentrations appear in the images as bright regions. In Fig. 4.11 we present the temporal evolution of the filament in the line core of Ca II line at $\lambda 8542 \text{ \AA}$ within the two hours of observations for selected points separated in time by approximately 15 min. The time-lapse movies are corrected concerning motions between the images. Initially, we describe the first image of the time-series at 15:48:04 UT. The appearance of the Ca II $\lambda 8542 \text{ \AA}$ differs from the image in H α . We labeled the region, which we will discuss in more detail. Regions A and E appear as bright regions, which means in this line that the magnetic-field in these regions is strong compared to the dark surroundings. The surroundings has similar to the H α line a filamentary appearance, which is typical for the chromosphere. In region C the prominent dark clumpy structure of the main part of the filament is located. In region B there is a dark region originating from region A. At that time there is in region D only a faint dark structure, which will evolve later. The time-lapse movie of the time-series shows that the brightness in regions A and E is changing over time, thus also the related magnetic field strength. Especially, in region E the intensity is first increasing until 16:15:22 UT (Fig. 4.11) and then decreases until 17:28:33 UT (Fig. 4.11). Thereafter, the intensity increases again. At the end of the time-series in H α the LOS velocities increased to very high values, likely due to a strengthening of the magnetic field concentration seen in Ca II $\lambda 8542 \text{ \AA}$. Region A shows only an increasing of intensity until 16:14:22 UT (Fig. 4.11). Afterwards, the intensity remains more or less stable. In regions C and D two dark structures separate into two filaments, as we have seen it in the H α time-lapse movies before. Consequently, the filament in region C is reduced in size at the end of the time-series (Fig. 4.11 at 17:58:21 UT). In region B a filament develops between regions A and E (visible in Fig. 4.11 at 17:38:33 UT). We conclude that the overall behavior of the filament in both lines, H α and near-infrared (NIR) Ca II is the same with differences in details, like in the size of the filament.

In Fig. 4.12 we present the scan through the Ca II $\lambda 8542 \text{ \AA}$ line for the best time-series concerning the MFGS values at around 16:01:38 UT. We show different positions in the wings of the line, as well as the line core itself. The wing positions are selected at around Ca II $\pm 0.75 \text{ \AA}$. Due to the irregular grid, we can show the positions at Ca II -0.70 \AA and Ca II $+0.96 \text{ \AA}$. Furthermore, we show the images at the

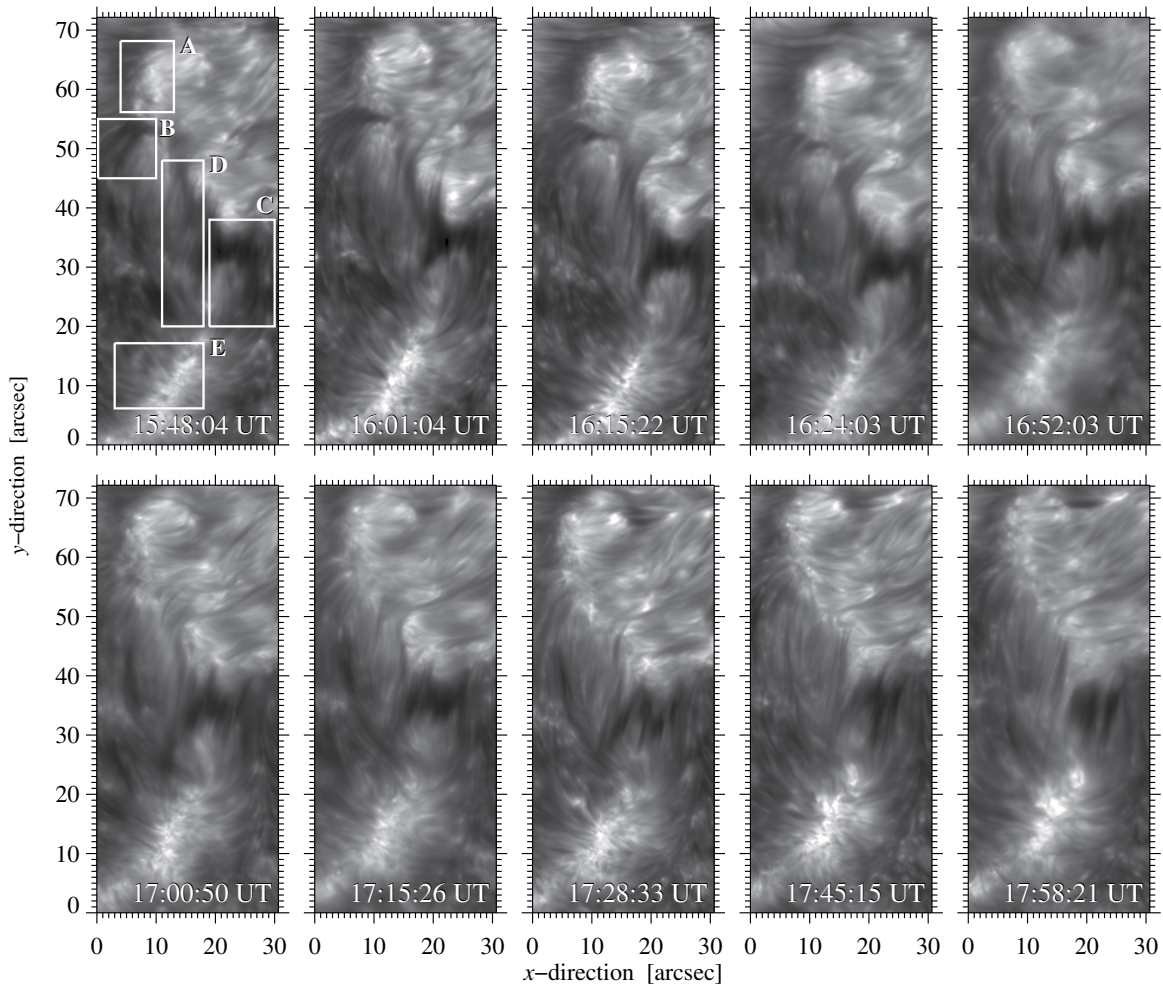


Figure 4.11: Temporal evolution of the filament in the chromosphere with the magnetically sensitive infrared Ca II $\lambda 8542$ Å line. The line-core image ($\lambda_{\text{cwl}} = 8542.12$ Å) is shown for the two hour time-series starting at 15:48 UT on 2013 January 20.

positions $\text{Ca II} \pm 0.35$ Å. The images are extracted from the original format to get rectangular images. The resized images have 383×902 pixels, which corresponds to a size of $30''.6 \times 72''.2$. With the scan between $\lambda_{\text{min}} = 8539.77$ Å and $\lambda_{\text{max}} = 8544.47$ Å we can observe different atmospheric heights in the solar atmosphere. The positions in the wing farthest away from line core show the regions closer to the photosphere. Thus, the scan through the line is also a scan through the atmospheric layers of the Sun. The line core of Ca II itself is located in the chromosphere. As in Fig. 4.11, the filamentary structure of the chromosphere is present as the clumpy filament in the center of the FOV (Fig. 4.12 0 Å). Only ± 0.35 Å away from the line core the morphology of the lower layers changes significantly. Here, the structures resemble the photospheric granulation. The bright features are related to strong magnetic field concentrations. Furthermore, dark thin structures, similar to mottles originate in the bright regions, which may be related to the filament in the higher atmospheric layers. Both images slightly differ from each other, which would imply that we see not the same atmospheric layer. At $\text{Ca II} - 0.70$ Å and $\text{Ca II} + 0.96$ Å the images show the inverted granulation and the bright regions associated with magnetic field similar to the Ca II K line, as in the ROSA data (Fig. 4.3). The Ca II K line originates from the upper photosphere and lower chromosphere, and lies deeper than the infrared Ca II $\lambda 8542$ Å line. Anyway, the spectral lines are formed in a large zone in the atmosphere (Stix, 2004) and structures overlap. Furthermore, the line wings originate from lower atmospheric layers than the line core.

For the infrared calcium line we created physical maps as described at Sect. 4.3.1 for roughly the same time as for H α observations. In Fig. 4.13a we show the map of the line core intensity. By comparing the line-core intensity map with the line-core image in Fig. 4.11, no differences are apparent between the image, but in detail, some minor differences are recognized. The next physical map is the contrast profile of the image. As described in Sect. 4.3.1, we first calculate the quiet-Sun profile analogously to

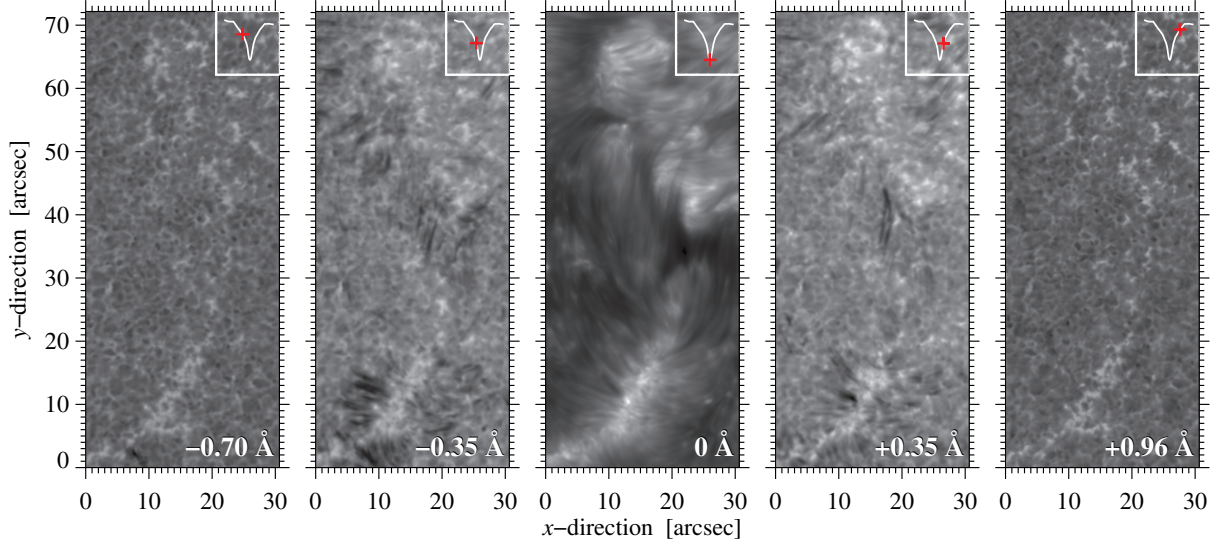


Figure 4.12: Line scan of best Ca II image-series for at 16:01:38 UT with a size of $30''6 \times 72''2$. The scans show images at the wavelength positions Ca II -0.7 \AA , Ca II $\pm 0.35 \text{ \AA}$, Ca II $+0.96 \text{ \AA}$ and the line-core image ($\lambda_{\text{cwl}} = 8542.21 \text{ \AA}$). The line core is located in the chromosphere, where the images further away from the core are showing lower atmospheric regions.

$H\alpha$ profile. Afterwards, we subtract and divide for each pixel the profile and yield the contrast profile shown in Fig. 4.13b. The highest contrast we have in the bright, magnetically sensitive structures, which are dominant in this map. But also the clumpy region of the filament is seen as more faint bright structure. Interestingly, parts of quiet-Sun in the image exhibit more granular structures than in the line-core image. In $H\alpha$, there are still the filamentary structures of the chromosphere, but maybe because of the broad spectral line. The Ca II $\lambda 8542 \text{ \AA}$ spectral line is much more narrow. Also this contrast profile will be used in a later publication as a basis for the cloud model.

In addition, we calculated the LOS velocities with two different methods: the Fourier method (Fig. 4.13c), and a second-order polynomial fit to the line core (Fig. 4.13d). To calculate the Doppler shift, we use as a reference wavelength the line-core position of the quiet-Sun profile, which is in this case $\lambda_0 = 8542.21 \text{ \AA}$, which is also the wavelength position of the line-core image. In literature, we find for a quiet-Sun profile the value $\lambda_{0,\text{ref}} = 8542.14 \text{ \AA}$ (Moore *et al.*, 1966). By inspecting the LOS velocity map derived with the Fourier method, the typical filamentary structure is missing in the line-core intensity map (Fig. 4.13a) but the map exhibits structures visible in the line wings of Ca II $\lambda 8542 \text{ \AA}$ (see Fig. 4.12). The most prominent structure in the image is the strong down-streaming flow in region D with a smaller up-streaming flow parallel to it. In the line-core intensity map, we find the dark structure of the filament, which is rooted in the bright region above region D. Furthermore, a strong down-streaming flow is located in the upper half of region E. The lower half is more dominated by up-streaming flows. In region C, the up- and down-streaming flows are mixed so that we cannot recognize structures related to the filament. Region B is instead dominated by down-streaming flows, whereas region A shows both, down-streaming flows in the lower left part of the region and up-streaming flows in the upper right part. In addition, in the upper right corner of the map, down-streaming flows are present which originate from the sunspot. The strongest up-streaming flows have a LOS velocity of -4.8 km s^{-1} and down-streaming velocities of up to 6.1 km s^{-1} . The mean velocity is close to zero. In the time-lapse movies the development of region D starts at around 16:55 UT with the separation of the filament structures. Furthermore, we see in the upper part of region E that the velocities increase for a large area with down-flow velocities of up to 33.6 km s^{-1} .

For the next map of LOS velocities we are fitting a second order polynomial between $\pm 0.12 \text{ \AA}$ around the line-core position, to determine accurately the central position of the line. The small region is sufficient, because this spectral line is much narrower than the $H\alpha$ line. The reference wavelength λ_0 is calculated from the quiet-Sun profile. The result for the velocities is shown in Fig. 4.13d. The overall shape containing the filamentary structures is similar to the appearance of the line-core intensity map and resembles also the results for the velocities in $H\alpha$. In the upper right corner, a strong down-streaming flow is located coming from the direction of the sunspot. The possible footpoint regions A and E are showing

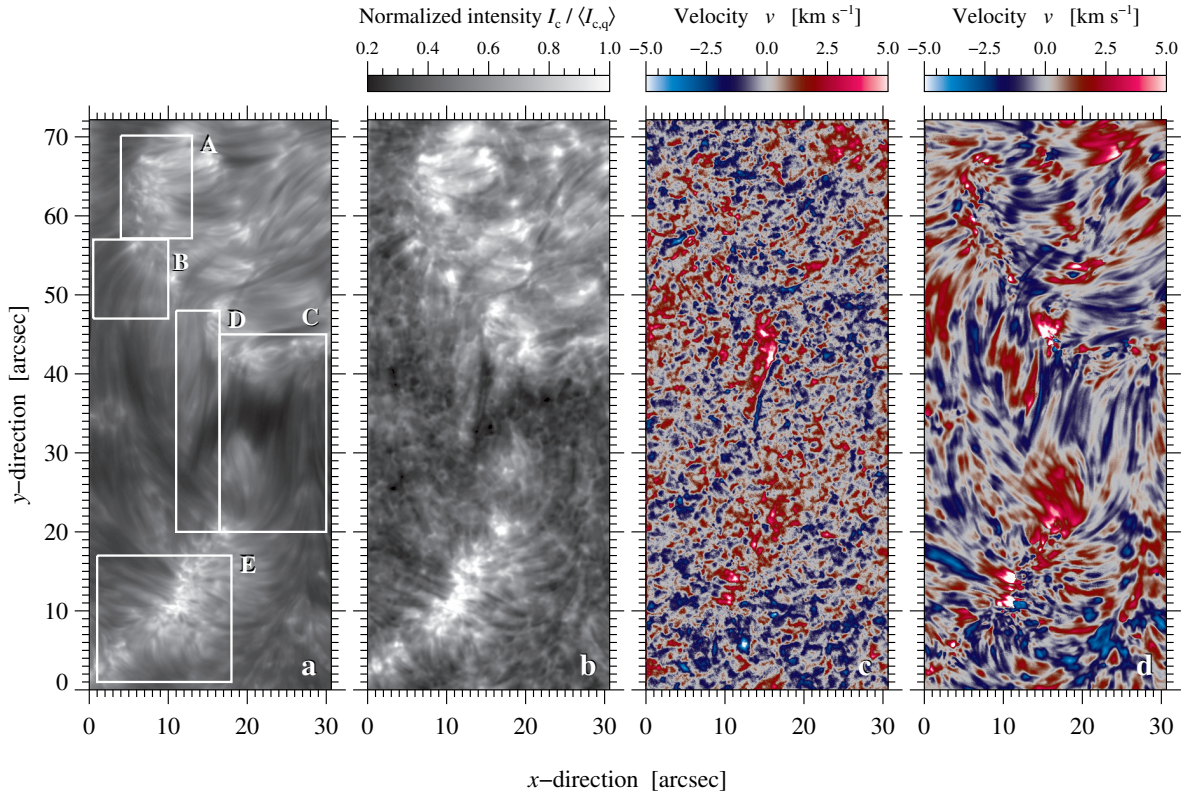


Figure 4.13: Physical maps of NIR Ca II data at 17:21:42 UT: (a) line-core intensity, (b) contrast profile, (c) Doppler velocity based on Fourier method, and (d) Doppler velocity with fitting the line core. Both Doppler maps are clipped at velocities $\pm 5 \text{ km s}^{-1}$ and the white regions denote saturated values.

mixed up- and down-streaming flows, where in the upper part of region E a strong down-streaming flow is present. Region B contains a strong down-streaming flow but on the other end of this loop structure close to region E there is a strong up-streaming flow. Region D shows an interplay of strong up- and down-flow velocities as seen for H α . Close to the possible footpoints we see down-streaming flows. Region C is dominated by up-streaming flows, which have values of around -2.0 km s^{-1} . In the whole image, we track LOS velocities between -4.6 km s^{-1} and $+12.6 \text{ km s}^{-1}$. The mean velocity is close to zero. In the time-lapse movies the previously described behavior of the flows is seen as well in the evolution of the structures in regions B and D. In region B the formation of an up-streaming structure between regions A and E can be seen, whereas in region D the interplay of up- and down-streaming flows is present during the time-series. In regions E and D we see the rise of a strong down-streaming structure. Furthermore, the time-lapse movies display the rise and decay of a strong up-flowing structure in the direct neighborhood of the strong down-streaming structure in the upper part of region D in the beginning of the time-series. We see in the maps that the line-core fitting only takes into account the intensities in a narrow range, which belong to higher atmospheric layers. In contrast, the Fourier method samples the full spectral line, i.e., with strong contributions from the line wings, which are formed in lower layers of the atmosphere. This is visible in the velocity map (see Fig. 4.13c)

In the end, we discuss to additional fitting methods to determine the line-core position of the spectral line, whereby we fit the spectral line with a Gaussian and a Lorentzian. In general, a good approximation for a spectral line is a Gauß function. Due to broadening effects this approximation is not sufficient and a Lorentzian function could be more appropriate. Still, these two functions may not represent the real spectral line. In the chromosphere the lines are much broader and deeper and the Fabry-Pérot-interferometer has just scanned a part of the spectral line, as in the case of the H α and the NIR Ca II line. With both methods it makes no sense to derive the equivalent width from these fits, but the methods can be still used to determine the position of the line core and calculate from this position the LOS velocities.

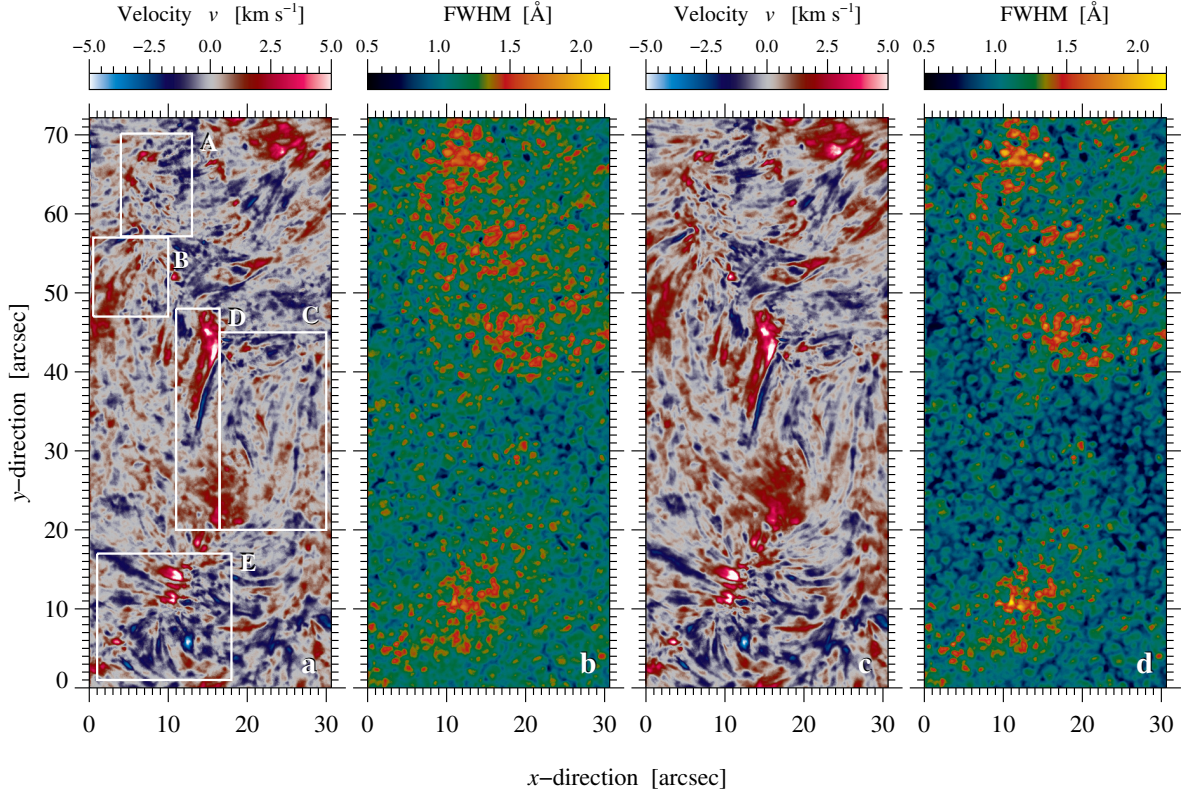


Figure 4.14: Physical maps of NIR Ca II data obtained by fitting a Gaussian to the spectral line: (a) Gaussian: LOS velocity clipped between $\pm 5 \text{ km s}^{-1}$, where the white regions denote saturated values, and (b) FWHM of the Gaussian fit. (c) Lorentzian: LOS velocity clipped between $\pm 5 \text{ km s}^{-1}$ and (d) FWHM of the Lorentzian fit.

We are assuming a general Gauß function:

$$G(x) = \frac{1}{\sqrt{2\pi}\sigma} \cdot \exp\left[-\frac{1}{2} \left(\frac{x-\mu}{\sigma}\right)^2\right] + c, \quad (4.5)$$

with σ as the standard deviation and μ as the mean value of the Gaussian. The Gaussian fitted to the interpolated profile of the spectral line has four free variables c_0, \dots, c_3 :

$$G_4(\lambda) = c_0 \cdot e^{-0.5 \cdot z^2} + c_3, \quad (4.6)$$

$$\text{with } z = \frac{\lambda - c_1}{c_2}. \quad (4.7)$$

We see that the coefficient c_1 is equal to μ , and the central position λ_c in Eq. (3.11) is given by the coefficient c_1 . From this coefficient we calculate the Doppler shift as described in the other cases with Eq. (3.11), because the central position is already given as a wavelength and thus we gain the LOS velocities presented in Fig. 4.14a. Comparing this map with the maps derived with the two previous methods (Fig. 4.13c and d) the behavior is similar in the described regions. Still, strong down-streaming flows are located in the upper part of region E, in region B, and in the upper and lower part of region D. Furthermore, in region D we find a strong up-streaming flow next to the strong down-streaming flow in region D. In addition, in the upper right corner the strong down-streaming flows coming from the sunspot are still present. In region A, we see both up- and down-streaming flows. The maximum value for the up-streaming flow is -5.1 km s^{-1} , for the down-streaming flow the maximum value is 6.6 km s^{-1} , and the mean flow speed is slightly redshifted with a value of 0.04 km s^{-1} .

The saturation of the Gaussian is given by the coefficient c_3 . In a narrow line, where the continuum is reached by the spectral line, this coefficient is used to calculate the equivalent width $W_{i,j}$ of the Gaussian

$$W_{i,j} = \frac{I_{\text{tot},i,j}}{I_0}, \quad (4.8)$$

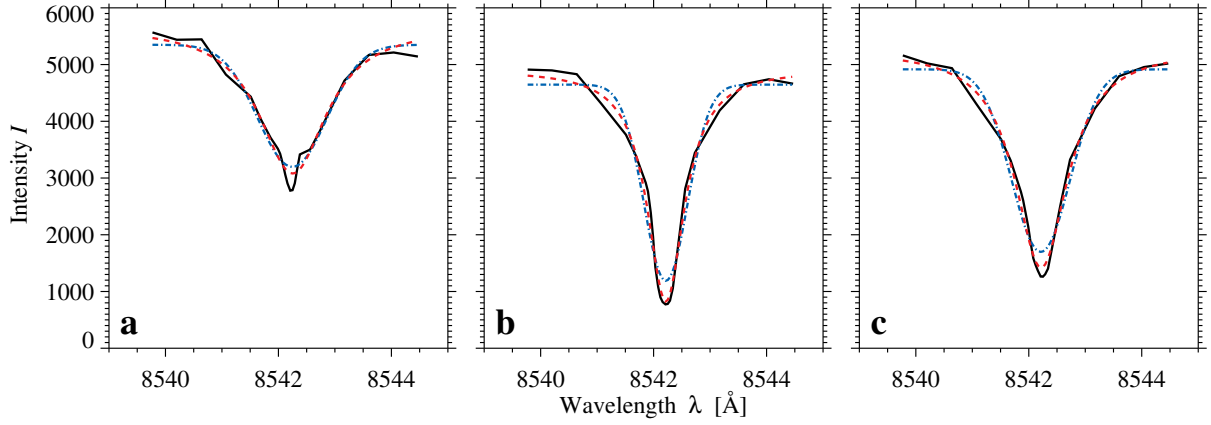


Figure 4.15: Comparison of the fits with Gaussian (blue dash-dot-line) and Lorentzian (red dashed line) to the spectral line (black solid line) in (a) a bright region, (b) the filament, and (c) quiet Sun.

where $I_0 = c_3$ and I_{tot} is the area of the spectral line. In the case of the NIR Ca II line the equivalent width would be underestimated compared to the real value and is not presented here.

Furthermore, we calculate the FWHM, which is the width of the Gaussian, when the intensity between minimum and maximum of the Gaussian is at half of the value. The FWHM is defined as

$$\text{FWHM} = 2\sqrt{2\ln 2} \cdot \sigma \approx 2.35482 \cdot \sigma = 2.35482 \cdot c_2, \quad (4.9)$$

where $\sigma = c_2$. In the case of the NIR Ca II line, where the continuum level is not included in the scan, we get the full width not exactly at half minimum of the spectral line but at roughly 60% of the minimum. The resulting map is shown in Fig. 4.14b. The total wavelength range of the scanned spectral line has a length of 4.7 Å. The FWHM derived by fitting the Gaussian has a minimum value of 0.55 Å, a maximum value of 1.91 Å, and a mean value of 1.15 Å.

The Lorentzian fitted to the spectral line is defined as

$$L(x) = \frac{c_0}{u^2 + 1} + c_3, \quad (4.10)$$

$$\text{with } u = \frac{\lambda - c_1}{c_2}. \quad (4.11)$$

The coefficient c_3 is the saturation value of the the Lorentzian fit to the line, but this coefficient does not represent the continuum level of the spectral line. The coefficient c_0 is the intensity value of the peak of the Lorentzian. Similar to the Gaussian, the coefficient c_1 is the central position λ_c , which is used for the calculation of the Doppler shift of the line in the same way as described before. The resulting map is shown in Fig. 4.14c. Comparing the appearance of both maps for Gaussian and Lorentzian, they are very similar, and differ only in details. The maximum up-streaming flow speed of the map is -4.9 km s^{-1} and the maximum down-streaming flow speed is 8.0 km s^{-1} . The map has a higher number of redshifted components, which is visible in the mean value of the map with 0.22 km s^{-1} .

The Half-width-at-Half-Minimum (HWHM) of the fitted Lorentzian is encoded in the coefficient c_2 . The full width is then the double value of the HWHM. Also here, the FWHM is not representing the FWHM of the spectral line but 60% of it. The resulting map is shown in Fig. 4.14d. The maximum value for the FWHM is 2.34 Å and the minimum value is 0.49 Å. The mean value is 1.05 Å. The Lorentzian fit gives values in a broader range but with a similar mean value compared to the Gaussian. Both maps (Figs. 4.14b and d) show similar behavior, where the high values for the FWHM are found in the bright regions and the smaller values in regions associated with quiet Sun.

In the end, we have a more detailed look on how good the spectral line is represented by a fit of a Gaussian or a Lorentzian. For this purpose, we selected three regions at different locations of the map. The first sample is located in a bright region (Fig. 4.15a), the second is located in the dark structures of the

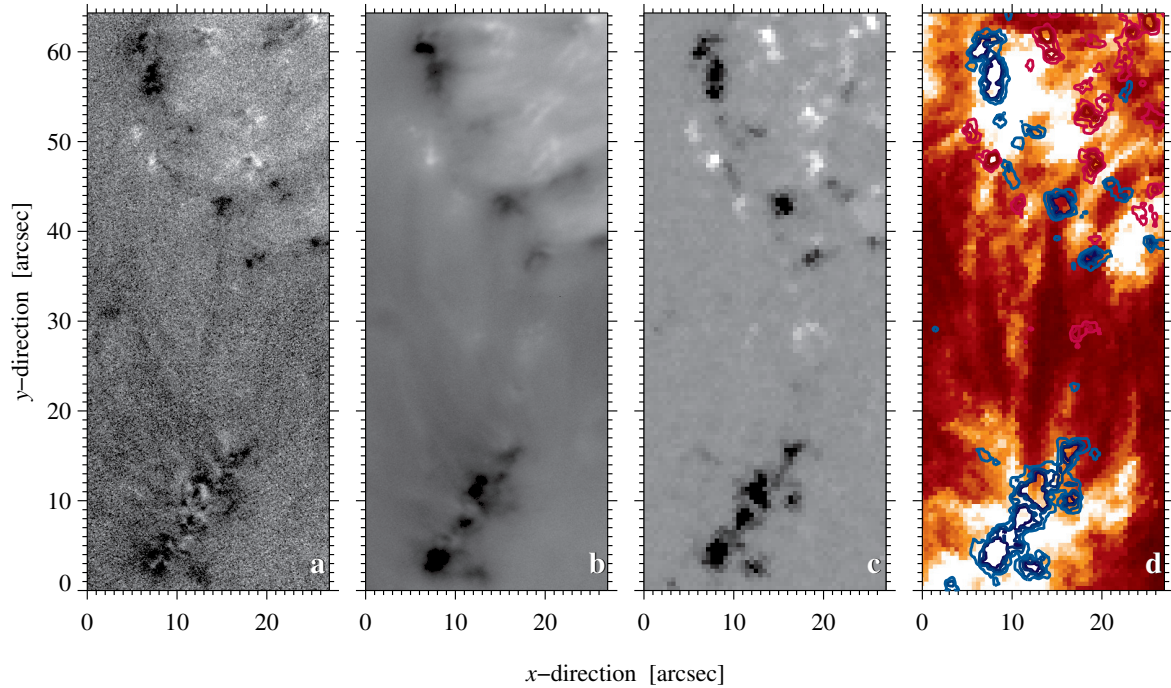


Figure 4.16: (a) Single IBIS Stokes V map of Ca II $\lambda 8542 \text{ \AA}$ and (b) two-hour average of IBIS Stokes V maps scaled between the same values. (c) HMI magnetogram clipped between $\pm 250 \text{ G}$, showing the positive (white) and negative (black) magnetic polarities. (d) AIA $\lambda 304 \text{ \AA}$ with contours of the positive (red) and negative (blue) magnetic fields between $\pm 50 \text{ G}$ and $\pm 200 \text{ G}$ in steps of 50 G , where the intensity of the color increases with the strength of the magnetic field.

filament (Fig. 4.15b), and the third sample is in the quiet Sun (Fig. 4.15c). The spectral line (black solid line) itself as well as the fits with a Gaussian (blue dashed-dotted line) and the Lorentzian (red dashed line). The spectral line in the bright region has less intensity and is broader. Furthermore, the line core of the line is shaped irregular. As a result, the Gaussian and the Lorentzian do not represent the line very well. The intensity value of the line core is in both cases not represented and also the ends of the spectral line are not fitted well. The spectral profile of the filament reaches smaller intensity values and is also narrower in the region around the line core compared to the spectral profile in the bright region. The Lorentzian fits the line-core very well, but the wings are not fully represented. The Gaussian fails to represent both the line core and the wings. In the third sample, the spectral profile of quiet Sun is shown. In this case, both fits do not represent the line-core intensity very well, but the wings are fitted better, where the Lorentzian represents the wings better. For all cases we can conclude, that the spectral line is not fully represented with neither of the functions, but for estimating the line-core position and the FWHM the fits are sufficient.

4.3.3 Magnetic Field Information with IBIS Data

During the data reduction process the polarization states were separated into the four Stokes vectors I, Q, U, and V. The Stokes V component contains information about the circular polarization of the electromagnetic radiation. The polarimetric images of the IBIS NIR Ca II line contain for each pixel Stokes profiles, which are summarized into maps. Each Stokes V map of IBIS is aligned to each other by determining the displacement vector corresponding to the previous image and shifting the image by this value. The Stokes V profiles are very noisy (Fig. 4.16a). Averaging the single maps of the two-hour time-series the noise decreases in the profiles by \sqrt{n} , where n is the number of maps. This is justified because no big changes occur in the magnetic field during this short time period. The resulting Stokes V map is shown in Fig. 4.16b. The corresponding HMI magnetogram is aligned with respect to the FOV of IBIS and clipped between $\pm 250 \text{ G}$ (Fig. 4.16c). The AIA $\lambda 304 \text{ \AA}$ image is aligned in the same way and presented in the typical color table of this wavelength (Fig. 4.16d). In addition, the contours of the

Table 4.2: Comparison of LOS velocities in H α and Ca II IR from different methods. The methods are the Fourier method (I), the line-core fitting with an parabolic function (II). Additionally, we derived for Ca II IR velocities by fitting the spectral line with a Gaussian (III) and Lorentzian (IV). We present the maximum velocity v_{\max} for up- and down-streaming flows.

Wavelength	Method	v_{\max} in km s $^{-1}$	
		up	down
H α	I	-7.5	7.5
	II	-5.2	9.9
Ca II λ 8542 Å	I	-4.8	6.1
	II	-4.6	12.6
	III	-5.1	6.6
	IV	-4.9	8.0

magnetic field at different strengths from HMI are plotted on top of the image. At this state of the analysis of the Stokes V map, we have no information about the strength of the chromospheric magnetic field. We just compare the quantitative appearance of the Stokes V map with the magnetogram from HMI and the AIA λ 304 Å image. The HMI magnetogram shows the magnetic field in the photosphere, where instead the IBIS NIR Ca II line contains the magnetic field information in the chromosphere. Comparing both maps, the appearance is very similar. The lower part of the map is dominated by negative polarized magnetic field and the upper part has mixed polarities, where the stronger regions are still negative polarized. In the single IBIS magnetograms we see in the lower negative polarized magnetic field traces of positive polarized magnetic field, which refers to flux cancellation in this region. Also in the upper part of the image in the positive polarized magnetic field, we have small negative polarized features referring to flux cancellation. The flux cancellation in that regions is also visible in the time-lapse movies of the IBIS magnetograms. In the single IBIS magnetogram as well as in the averaged map (Fig. 4.16a and b), we recognize more positive polarized magnetic flux in the upper right corner. Furthermore, we see in both maps a negative polarity haze at the location of the filaments, which are probably related to the weak magnetic field of the filaments in the chromosphere. In the upper right corner this haze for the positive polarities is also visible which may be connected to the magnetic field of the sunspot. The relation of the haze with the filament has to be verified with the other Stokes profiles Q and U. Even though referring to different layers in the atmosphere the two magnetic field maps appear very similar. The AIA image reveals that at the location of the strong magnetic field high intensities are located. Comparing these regions with the IBIS images, we identify them with region A and E in Figs. 4.10 and 4.13, which are the candidates for footpoints. In Chap. 5 we will revisit this topic. Between the two regions, we see the dark elongated structure of a filament, which corresponds to the dark structure in region D of the IBIS images. The clumpy structure of region C is not recognizable in the AIA images.

4.3.4 Comparison and Discussion of IBIS Results

We have examined the results of the IBIS data for the H α and Ca II λ 8542 Å lines and have seen that the structures in the line-core images of both lines look similar. For both data sets we have used the same analysis methods. We created the line-core intensity maps, we derived the contrast map for later analysis with the cloud model, and we calculated LOS velocities with two different methods. In addition, we used Gaussian and Lorentzian fitting for the infrared Ca II data to derive LOS velocities, and to estimate the FWHM. The first two methods applied to the H α data show very similar results, which differed only in details. In contrast, the three methods applied to the infrared Ca II data yield different results for the velocities. With the Fourier method we obtain a velocity map, which shows the velocities in granular clusters and with the line-core fitting method we get a smoother map, which reproduces the filamentary structures of the line core. Anyway, both show the same behavior of the main up- and down-flows. Furthermore, the LOS map from the Gaussian and Lorentzian method show similar results as the line-core fitting but with more flow speeds close to zero. In Table 4.2 we present the maximum flow speeds for

both, up- and down-flows for the different wavelength and the different methods. All flow speeds are of the same order of magnitude. For the Fourier method (I) in $H\alpha$ we get symmetric values for both up- and down-streaming flows of velocities with $\pm 7.5 \text{ km s}^{-1}$. The results for the same method in $\text{Ca II } \lambda 8542 \text{ \AA}$ gives slightly lower values, where the down-streaming flows reach higher values of up to 6.1 km s^{-1} . The line-core fitting method (II) in $H\alpha$ derives more asymmetric values with -5.2 km s^{-1} and 9.9 km s^{-1} , where the difference in $\text{Ca II } \lambda 8542 \text{ \AA}$ is much higher with the up-streaming flow speeds of -4.6 km s^{-1} , and down-streaming flow speeds of up to -12.6 km s^{-1} are present in the map. The Gaussian (III) and the Lorentzian (IV) fitting methods was only used for the Ca II data. Compared to the other methods, we get similar results as for the Fourier method, also the maximum flow speed with the Lorentzian is higher.

Chapter 5

Discussion

Finally, we will discuss the results that we derived for the active region filament. This filament is not a classical filament with an elongated spine but has a clumpy appearance. In the evolution of the filament we have seen the separation of the clumpy filament and the elongated fibrils next to it. Furthermore, the development of a third filament was visible during observations. All these phenomena show that the chromosphere above the active region was very dynamic. The filament is rooted with its two extreme ends in the photosphere but we detect none of the classical barbs. The absence of barbs in active region filaments is not unusual and was reported in the literature (Joshi *et al.*, 2013).

We detected motions in the FOV for different layers in and around the active region filament. In G-band images we tracked horizontal velocities related to the granulation reaching values of up to 1.80 km s^{-1} . Note that the velocities were averaged over a time interval of 66 min. Verma and Denker (2011) report similar results in Hinode quiet-Sun G-band images with maximum values of up to 1.86 km s^{-1} averaging over a time interval of one hour. The mean value of these observations yield flow speeds of 0.43 km s^{-1} , which is slightly lower compared to the present study with a mean flow speed value of 0.61 km s^{-1} . The higher mean values in the ROSA images can be explained with the moat flow of the nearby sunspot, which contributes to the horizontal velocity measurements. Furthermore, Verma and Denker (2011) derived low velocities for G-band bright points with maximal flow speeds of 0.7 km s^{-1} and mean values of $0.22 \pm 0.10 \text{ km s}^{-1}$. In this study, we find slightly higher values for the flow speed of the G-band bright points. The maximum velocity in these regions is 0.8 km s^{-1} and the mean value is 0.45 km s^{-1} with a standard deviation of 0.19 km s^{-1} , which are small flow speeds compared to the velocities at the borders of mesogranular cells.

In the chromosphere, we measure velocities related to the filament itself. Here, the flow speeds reach higher values of up to 2.24 km s^{-1} in $H\beta$, which is comparable with velocities along the spine of a quiet-Sun filament observed with SDO/AIA in $\lambda 304 \text{ \AA}$ EUV images, where we encounter values of up to 2.37 km s^{-1} but averaged over a time range of two hours (Diercke *et al.*, 2016). The $\lambda 304 \text{ \AA}$ images show higher atmospheric layers (upper chromosphere – transition region) than the atmospheric layer of $H\beta$ (chromosphere). Lin *et al.* (2005) reports an average horizontal velocities of $15 \pm 10 \text{ km s}^{-1}$ along the spine for a quiet-Sun filament in $H\alpha$. These authors remark that these velocities are higher than typical flow speeds of around 8 km s^{-1} (Lin, Engvold, and Wiik, 2003). Not many studies of motions in active region filaments are reported, which makes it difficult to compare results to others.

The comparison is even more complicated for LOS velocities, because they depend on the position on the solar disk and are strongly affected by the chosen λ_0 for calibration (Kuckein, Martínez Pillet, and Centeno, 2012). We derived LOS velocities only for the chromospheric lines $H\alpha$ and Ca II IR. The maximum flow speeds reach values between -7.5 km s^{-1} and -5.0 km s^{-1} for the blueshifted $H\alpha$ profiles and between 7.5 km s^{-1} and 10 km s^{-1} for the redshifted profiles. The blueshifted Ca II IR profiles reach values of around -5 km s^{-1} , whereas the redshifted profiles reach maximum values between 6 km s^{-1} and 12.6 km s^{-1} , which are supersonic flow speeds. By studying flows in a quiet-Sun filament in $H\alpha$, Lin, Engvold, and Wiik (2003) found average LOS flow speed values of only $\pm 1.9 \text{ km s}^{-1}$. Furthermore, we find the high velocities in regions with high brightness, which was also found for a quiet-Sun filament by Martres *et al.* (1981). These authors further concluded that slow motions smaller than 4 km s^{-1} are associated with blueshifts which last for several hours, whereas fast motions of around 7 km s^{-1} have

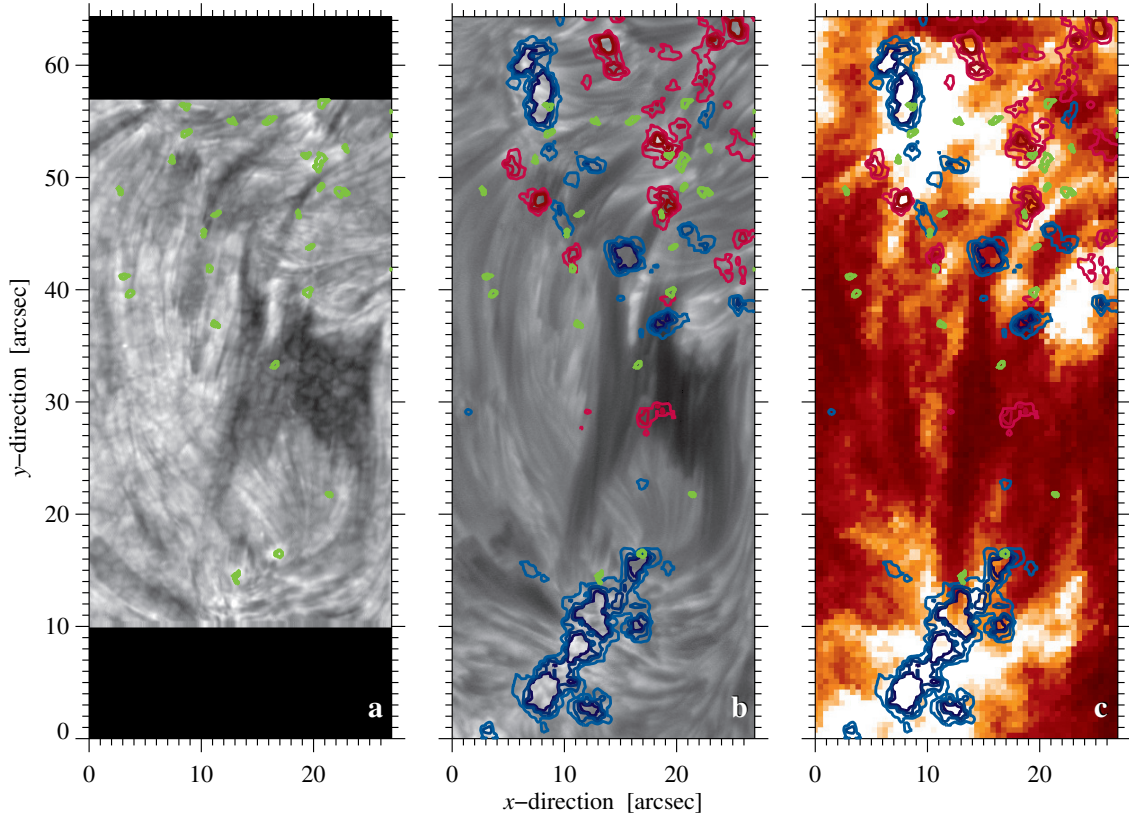


Figure 5.1: (a) ROSA $H\beta$ image with contours of G-band bright points (green). (b) IBIS $H\alpha$ image with contours of G-band bright points and the positive (red) and negative (blue) magnetic field between ± 50 G and ± 200 G in steps of 50 G, where the saturation of the color increases with the strength of the magnetic fields. (c) AIA $\lambda 304 \text{ \AA}$ image with contours of HMI magnetic field strength and the G-band bright points

life-times of a few minutes. In the case of the active region filament in this study, we found predominantly up-streaming flows in the clumpy spine of the main filament. The separated elongated filament contains both up- and down-streaming flows in the filaments over the entire time-series in approximately the same strength. Only towards the end of the time-series the down-streaming flows increase in region E (see Fig. 4.10). Examining other chromospheric lines, i.e., He I 10830 \AA , Kuckein, Martínez Pillet, and Centeno (2012) found much smaller velocities of around $0.2 - 0.6 \text{ km s}^{-1}$ for the redshifted profiles, but using two-component inversions of the Stokes V profiles provide supersonic speeds of $6 - 12 \text{ km s}^{-1}$, which is in agreement with the results of this study for the Ca II $\lambda 8542 \text{ \AA}$ line.

Different assumptions were made how filaments are rooted in the magnetic field of the photosphere. López Ariste *et al.* (2006) refers to two models explaining the appearance of feet or barbs. In the first model the feet are part of arcades, which are anchored in the magnetic field, which is supported by the injection model of filament formation, where plasma is transported by upward jets or up-flows into the filament due to reconnection (Karpen, 2015). The second model favors condensation as the origin of filament formation considering upward curved field lines, i.e., magnetic dips. These photospheric dips connect the filament with the photosphere. Thus, the barbs are connected to regions, where the minor polarity opposite to the dominant polarity in this region is appearing (Martin, 1998a). The ends of the spine, the largest extension of the filament in $H\alpha$, are rooted in opposite magnetic fields crossing the PIL (Martin *et al.*, 2012). Towards the end of the time-series, the active region filament in this study is built-up of three separated filamentary structures. We aligned the images of ROSA and IBIS with HMI magnetograms and AIA images. By inspecting aligned images (see Fig. 5.1), we conclude that the ends of the two elongated structures are rooted in the positive magnetic field in the upper half of the FOV and in the negative polarity in the lower half. The clumpy filament instead is rooted between the positive polarity in the middle of the FOV at coordinates $(18'', 29'')$ and the negative polarity at coordinates $(18'',$

37"). This structure appears darker in the $H\alpha$ images but is not visible in the AIA images (see Fig. 5.1c), which leads us to the conclusion that the clumpy filament lies below the other two structures. Furthermore, we expect down-flows at the location of the filament ends, which is seen in the negative polarities of region E and at the location of the negative polarity belonging to the clumpy filament in region C. In the time-lapse movies of the IBIS magnetograms, we see in the lower negative polarity part as well as in the upper positive polarity part flux cancellation, where the opposite polarity rises and decays. [Martin \(2015\)](#) characterize this flux cancellation as a property of a PIL at that location. A further property is the alignment of local magnetic field along the PIL visible in chromospheric fibrils, which is present in the this study as well (see Fig. 5.1a and b).

Furthermore, we compare the photospheric G-band bright points with the magnetic field in the photosphere (see Fig. 5.1). In this study, the location of the G-band bright points is close to one polarity but not in particular between them as one would expect for the footpoints. The location of the bright points coincide with the endpoints of the dark filamentary structures in most cases. In the study of [Ishikawa et al. \(2007\)](#), they discovered that G-band bright points are located at the border of strong small scale flux elements, which is confirm with our observations. Furthermore, the authors point out that the strong small scale flux elements surrounded by bright points shows down-flows, which is true for the present data set as well. We conclude that the bright points are related to strong magnetic flux but not necessarily to the footpoints of the filament. Further investigation is needed to clarify the location of the filament's footpoints. [Chae, Moon, and Park \(2005\)](#) point out that a careful study of the history of the magnetic field is important for the understanding of the relationship between the photospheric magnetic field region and endpoints of the filament. Therefore, it is necessary to carefully align the magnetograms with the high-resolution $H\alpha$ images. Nevertheless, we only have high-resolution $H\alpha$ images for a two-hour time-series. Longer data sets are provided by ChroTel ([Kentischer et al., 2008](#); [Bethge et al., 2011](#)) with $H\alpha$ full-disk images every three minutes between 8:36 UT and 17:18 UT, however with a much lower spatial resolution of 2".

The magnetic field strength in active region filaments is much larger compared to quiet-Sun filaments. [Kuckein et al. \(2009\)](#) found for this kind of filaments values of around 600–700 G. In this study, the magnetic field in the active region filament reach values of more than 200 G, where the negative polarity reaches even values of up to 600 G based on photospheric HMI data. Exact values for the chromosphere have to be derived from inversions of the Stokes V profiles, which are planed for an upcoming peer-reviewed publication. However, the S/N is low for single Ca II IR magnetic field maps so that average have to be taken, which results in lower spatial and temporal resolution and potentially affects the magnetic field measurements.

Chapter 6

Conclusion and Outlook

With the instruments at the DST we obtained an overview about the filament in different atmospheric layers from the photosphere into the chromosphere. We presented a detailed study about the temporal evolution over the two hours of observations of the active region filament in all atmospheric layer. The spectroscopic data sets of IBIS provided information of the spectral lines in $H\alpha$ and $\text{Ca II } \lambda 8542 \text{ \AA}$. Here, we examined other aspects of the filament such as the line-core intensity or the contrast profiles. However, the main part of the thesis was the investigation of the dynamics of the filament, which we directly derived from both horizontal and LOS velocities. Thus, we identified the strong flows from the direction of the sunspot. In the photosphere they are likely related with the moat flow of the sunspot. In the time-lapse movie, we have seen likely a separation of the filamentary structures from the clumpy part and the formation of a new filamentary structure. Furthermore, we have started to analyze the spectropolarimetric data of the $\text{Ca II } \lambda 8542 \text{ \AA}$ line. We compared quantitatively the Stokes V map with HMI magnetograms matching the IBIS FOV. Comparing the HMI magnetograms with $H\alpha$ data, we determined the location of the extreme ends of the elongated filament structures in the positive polarity in the upper half of the FOV and in the negative polarity in the lower half. The clumpy filament instead was rooted in the opposite polarities in the middle of the FOV. The comparison with AIA images showed that the clumpy part most likely is located in lower atmospheric heights compared to the elongated filament structures. The G-band bright points are located at the border of strong small scale flux elements.

Nonetheless, a much deeper analysis is possible, if given time, with this interesting data set of the DST. A qualitative study of the magnetic field information in the IBIS maps is planned for a forthcoming peer-reviewed article. To achieve more reliable vector magnetic field information in the non-local thermodynamic equilibrium (NLTE), we will use inversion codes, i.e., the NLTE Stokes Synthesis/Inversion Code (NICOLE, [Socas-Navarro, 2015](#)). Furthermore, we will use the cloud model on the $H\alpha$ data, and we already prepared the contrast profiles. With the cloud model, we have access to another method to obtain parameters such as the equivalent width, the FWHM, and the LOS velocity, and compare them to the parameters derived from the Gaussian and Lorentzian fitting. In addition, we can calculate the source function. The cloud model is especially important for the $H\alpha$ data set, where Gaussian fit are problematic considering the extended line wing of this strong chromospheric absorption line.

Furthermore, we will analyze the data set of the third instrument FIRS. Here, we have spectroscopic data of the $\text{He I } 10830 \text{ \AA}$ line. In this line the location of the filament channel can be deduced. With the help of space missions we are able examine the temporal evolution of the active region for a longer period of time. Towards the end of the observations we determined strong increasing down-flows, where the cause is still unclear and further investigation would be interesting. Unfortunately, the target changed and also the seeing decreased. [Zirker \(2002, p. 233\)](#) wrote: “Everything really interesting on the Sun either happens during the night or on the back side of the Sun.” We conclude that this statement is adaptable for bad seeing as well. Concerning the temporal evolution of the region, it would also be interesting to see the decay of the filament as well as of the active region.

To determine the actual location of the footpoints, we have the possibility to extrapolated the magnetic field topology from the magnetograms to approximate the location of the magnetic field lines in the corona. In the case of IBIS, we have magnetograms of the chromosphere. In principle, an extrapolation from chromospheric data is possible but not often done ([Wiegelmann and Sakurai, 2012](#)). The requirement would be, that the magnetograms are of high quality, which is not the case for the IBIS polarimetric data because they contain at least for single magnetograms a significant amount of noise. More reliable results from extrapolations can be derived with photospheric magnetic field data, e.g., we can use HMI vector magnetic field data.

Finally, a second peer-reviewed publication is planned with the data set of the sunspot, which is already analyzed for the ROSA data. Here, we will concentrate on the connection between the sunspot and the filament. In the photospheric data of the filament we already have seen the moat flow from the sunspot.

Bibliography

- Alexander, C.E., Walsh, R.W., Régnier, S., Cirtain, J., Winebarger, A.R., Golub, L., Kobayashi, K., Platt, S., Mitchell, N., Korreck, K., DePontieu, B., DeForest, C., Weber, M., Title, A., Kuzin, S.: 2013, Anti-parallel EUV Flows Observed along Active Region Filament Threads with Hi-C. *Astrophys. J., Lett.* **775**, L32–L37. doi:[10.1088/2041-8205/775/1/L32](https://doi.org/10.1088/2041-8205/775/1/L32).
- Asensio Ramos, A., Janssen, K., Cauzzi, G., Reardon, K.: 2006, High-Resolution IBIS Observations and Comparison with 3D Simulations. *Mem. Soc. Astron. Ital. Suppl.* **9**, 59–62.
- Beckers, J.M.: 1964, A Study of the Fine Structures in the Solar Chromosphere. PhD Thesis, Sacramento Peak Observatory, Air Force Cambridge Research Laboratories, Massachusetts, USA.
- Beckers, J.M., Dickson, L., Joyce, R.S.: 1975, A Fully Tunable Lyot-Öhman Filter. Technical Report, Bedford, Massachusetts, USA.
- Bely, P.Y.: 2003, *The Design and Construction of Large Optical Telescopes*, Springer, New York, USA.
- Bendlin, C.: 1993, Hochauflösende zweidimensionale Spektroskopie der solaren Granulation mit einem Fabry-Pérot-Interferometer. PhD Thesis, Universität Göttingen, Germany.
- Berger, T., Testa, P., Hillier, A., Boerner, P., Low, B.C., Shibata, K., Schrijver, C., Tarbell, T., Title, A.: 2011, Magneto-Thermal Convection in Solar Prominences. *Nature* **472**, 197–200. doi:[10.1038/nature09925](https://doi.org/10.1038/nature09925).
- Bethge, C., Peter, H., Kentischer, T.J., Halbgewachs, C., Elmore, D.F., Beck, C.: 2011, The Chromospheric Telescope. *Astron. Astrophys.* **534**, A105. doi:[10.1051/0004-6361/201117456](https://doi.org/10.1051/0004-6361/201117456).
- Bhatnagar, A., Livingston, W.: 2005, *Fundamentals of Solar Astronomy, World Scientific Series in Astronomy and Astrophysics*, World Scientific, Singapore.
- Bonaccini, D., Righini, A., Cavallini, F., Ceppatelli, G.: 1989, High Resolution Solar Bidimensional Spectroscopy with a Universal Birefringent Filter in Tandem with a Fabry-Pérot Interferometer. *Astron. Astrophys.* **217**, 368–374.
- Brandt, P.: 2001, Solar Photosphere: Granulation. In: Murdin, P. (ed.) *Encyclopedia of Astronomy and Astrophysics*. doi:[10.1888/0333750888/2008](https://doi.org/10.1888/0333750888/2008).
- Brault, J.W.: 1985, Fourier Transform Spectroscopy. In: *High Resolution in Astronomy, Fifteenth Advanced Course of the Swiss Society of Astronomy and Astrophysics. Edited by A.O. Benz, M. Huber, and M. Mayer. Geneva Observatory, Sauverny, Switzerland*, 3–61.
- Bray, R.J., Loughhead, R.E.: 1974, *The Solar Chromosphere*, Chapman and Hall, London, UK.
- Cavallini, F.: 2006, IBIS: A New Post-Focus Instrument for Solar Imaging Spectroscopy. *Sol. Phys.* **236**, 415–439. doi:[10.1007/s11207-006-0103-8](https://doi.org/10.1007/s11207-006-0103-8).
- Chae, J.: 2003, The Formation of a Prominence in NOAA Active Region 8668. II. TRACE Observations of Jets and Eruptions Associated with Canceling Magnetic Features. *Astrophys. J.* **584**, 1084–1094. doi:[10.1086/345739](https://doi.org/10.1086/345739).

- Chae, J.: 2014, Spectral Inversion of the H α Line for a Plasma Feature in the Upper Chromosphere of the Quiet Sun. *Astrophys. J.* **780**, 109. doi:[10.1088/0004-637X/780/1/109](https://doi.org/10.1088/0004-637X/780/1/109).
- Chae, J., Moon, Y.J., Park, Y.D.: 2005, The Magnetic Structure of Filament Barbs. *Astrophys. J.* **626**, 574–578. doi:[10.1086/429797](https://doi.org/10.1086/429797).
- Chapman, G.: 2001, Solar Photosphere: Faculae. In: Murdin, P. (ed.) *Encyclopedia of Astronomy and Astrophysics*. doi:[10.1888/0333750888/2253](https://doi.org/10.1888/0333750888/2253).
- Cliver, E.W.: 2014, The Extended Cycle of Solar Activity and the Sun's 22-Year Magnetic Cycle. *Space Sci. Rev.* **186**, 169–189. doi:[10.1007/s11214-014-0093-z](https://doi.org/10.1007/s11214-014-0093-z).
- Collados, M., López, R., Páez, E., Hernández, E., Reyes, M., Calcines, A., Ballesteros, E., Díaz, J.J., Denker, C., Lagg, A., Schlichenmaier, R., Schmidt, W., Solanki, S.K., Strassmeier, K.G., von der Lühe, O., Volkmer, R.: 2012, GRIS: The GREGOR Infrared Spectrograph. *Astron. Nachr.* **333**, 872–879. doi:[10.1002/asna.201211738](https://doi.org/10.1002/asna.201211738).
- Criscuoli, S., Tritschler, A.: 2014, *IBIS Data Reduction Notes*. National Solar Observatory (NSO), New Mexico, USA.
- de la Cruz Rodríguez, J., Löfdahl, M.G., Sütterlin, P., Hillberg, T., Rouppe van der Voort, L.: 2015, CRISPRED: A Data Pipeline for the CRISP Imaging Spectropolarimeter. *Astron. Astrophys.* **573**, A40. doi:[10.1051/0004-6361/201424319](https://doi.org/10.1051/0004-6361/201424319).
- Demtröder, W.: 2013, *Laserspektroskopie: Grundlagen und Techniken*, Springer, Berlin, Germany.
- Deng, H., Zhang, D., Wang, T., Ji, K., Wang, F., Liu, Z., Xiang, Y., Jin, Z., Cao, W.: 2015, Objective Image-Quality Assessment for High-Resolution Photospheric Images by Median Filter-Gradient Similarity. *Sol. Phys.* **290**, 1479–1489. doi:[10.1007/s11207-015-0676-1](https://doi.org/10.1007/s11207-015-0676-1).
- Denker, C., Balthasar, H., Hofmann, A., Bello González, N., Volkmer, R.: 2010, The GREGOR Fabry-Perot Interferometer: A New Instrument for High-Resolution Solar Observations. In: McLean, I.S., Ramsay, S.K., Takami, H. (eds.) *Proc. SPIE, Ground-Based and Airborne Instrumentation for Astronomy III*. **7735**, 77356M. doi:[10.1117/12.856830](https://doi.org/10.1117/12.856830).
- Diercke, A.: 2014, Dynamics and Evolution of a Giant Solar Filament as Observed by the Solar Dynamics Observatory. Bachelor's Thesis, Universität Potsdam, Germany.
- Diercke, A., Arlt, R., Denker, C.: 2015, Digitization of Sunspot Drawings by Spörer made in 1861–1894. *Astronomische Nachrichten* **336**, 53–62. doi:[10.1002/asna.201412138](https://doi.org/10.1002/asna.201412138).
- Diercke, A., Kuckein, C., Verma, M., Denker, C.: 2016, Counter-Streaming Flows in a Giant Quiet-Sun Filament Observed in EUV Images by SDO/AIA. *Astron. Astrophys.* in prep.
- Domingo, V., Fleck, B., Poland, A.I.: 1995, The SOHO Mission: An Overview. *Sol. Phys.* **162**, 1–37. doi:[10.1007/BF00733425](https://doi.org/10.1007/BF00733425).
- Engvold, O.: 1998, Observations of Filament Structure and Dynamics. In: Webb, D.F., Schmieder, B., Rust, D.M. (eds.) *New Perspectives on Solar Prominences, ASP Conf. Ser.* **150**, 23–31.
- Engvold, O.: 2015, Description and Classification of Prominences. In: Vial, J.C., Engvold, O. (eds.) *Solar Prominences, Astrophys. Space. Sci. Libr.* **415**, Cham, Switzerland, 31–60. doi:[10.1007/978-3-319-10416-4_2](https://doi.org/10.1007/978-3-319-10416-4_2).
- Gaizauskas, V.: 2001, Solar Filament Channels. In: Murdin, P. (ed.) *Encyclopedia of Astronomy and Astrophysics*, 2509–2515. doi:[10.1888/0333750888/2278](https://doi.org/10.1888/0333750888/2278).
- Gonzalez, R.C., Woods, R.E.: 2002, *Digital Image Processing*, Prentice-Hall, Upper Saddle River, New Jersey, USA.

- Gonzalez, R.C., Woods, R.E., Eddins, S.: 2009, *Digital Image Processing using MATLAB*, Gatesmark Publishing, Konxville, USA.
- González Manrique, S.J., Bello González, N., Denker, C.: 2016, High-Resolution Imaging Spectroscopy of Two Micro-Pores and an Arch Filament System in a Small Emerging Flux Region. *Astron. Astrophys.* submitted.
- Gregory, P.: 2005, *Bayesian Logical Data Analysis for the Physical Sciences: A Comparative Approach with Mathematica Support*, Cambridge University Press, Cambridge, UK. doi:[10.1017/CBO9780511791277](https://doi.org/10.1017/CBO9780511791277).
- Hanisch, R.J., Farris, A., Greisen, E.W., Pence, W.D., Schlesinger, B.M., Teuben, P.J., Thompson, R.W., Warnock, A.: 2001, Definition of the Flexible Image Transport System (FITS). *Astron. Astrophys.* **376**, 359–380. doi:[10.1051/0004-6361:20010923](https://doi.org/10.1051/0004-6361:20010923).
- Hecht, E.: 1998, *Optics, Addison-Wesley World Student Series*, Addison-Wesley, Massachusetts, USA.
- Herschel, W.: 1801, Observations Tending to Investigate the Nature of the Sun, in Order to Find the Causes or Symptoms of its Variable Emission of Light and Heat; with Remarks on the Use that May Possibly be Drawn from Solar Observations. *Phil. Trans. R. Soc. London Ser. I* **91**, 265–318.
- Howell, S.B.: 2006, *Handbook of CCD Astronomy*, Cambridge University Press, Cambridge, UK.
- Ishikawa, R., Tsuneta, S., Kitakoshi, Y., Katsukawa, Y., Bonet, J.A., Vargas Domínguez, S., Rouppe van der Voort, L.H.M., Sakamoto, Y., Ebisuzaki, T.: 2007, Relationships between Magnetic Foot Points and G-band Bright Structures. *Astron. Astrophys.* **472**, 911–918. doi:[10.1051/0004-6361:20066942](https://doi.org/10.1051/0004-6361:20066942).
- Jaeggli, S.A., Lin, H., Mickey, D.L., Kuhn, J.R., Hegwer, S.L., Rimmele, T.R., Penn, M.J.: 2010, FIRS: A New Instrument for Photospheric and Chromospheric Studies at the DST. *Mem. Soc. Astron. Ital.* **81**, 763–768.
- Janesick, J.: 2001, *Scientific Charge-Coupled Devices, Press Monographs*, The International Society for Optical Engineering, Bellingham, Washington, USA.
- Jess, D.B., Mathioudakis, M., Christian, D.J., Keenan, F.P., Ryans, R.S.I., Crockett, P.J.: 2010, ROSA: A High-Cadence, Synchronized Multi-Camera Solar Imaging System. *Sol. Phys.* **261**, 363–373. doi:[10.1007/s11207-009-9500-0](https://doi.org/10.1007/s11207-009-9500-0).
- Joshi, A.D., Srivastava, N., Mathew, S.K., Martin, S.F.: 2013, Rapid Formation and Disappearance of a Filament Barb. *Sol. Phys.* **288**, 191–203. doi:[10.1007/s11207-013-0295-7](https://doi.org/10.1007/s11207-013-0295-7).
- Karpen, J.T.: 2015, Plasma Structure and Dynamics. In: Vial, J.C., Engvold, O. (eds.) *Solar Prominences, Astrophys. Space. Sci. Libr.* **415**, 237–257. doi:[10.1007/978-3-319-10416-4_10](https://doi.org/10.1007/978-3-319-10416-4_10).
- Kentischer, T.J., Bethge, C., Elmore, D.F., Friedlein, R., Halbgewachs, C., Knölker, M., Peter, H., Schmidt, W., Sigwarth, M., Streander, K.: 2008, ChroTel: A Robotic Telescope to Observe the Chromosphere of the Sun. In: McLean, C.M.M. I. S. (ed.) *Ground-Based and Airborne Instrumentation for Astronomy II, Proc. SPIE* **7014**, 701413. doi:[10.1117/12.789044](https://doi.org/10.1117/12.789044).
- Kosugi, T., Matsuzaki, K., Sakao, T., Shimizu, T., Sone, Y., Tachikawa, S., Hashimoto, T., Minesugi, K., Ohnishi, A., Yamada, T., Tsuneta, S., Hara, H., Ichimoto, K., Suematsu, Y., Shimojo, M., Watanabe, T., Shimada, S., Davis, J.M., Hill, L.D., Owens, J.K., Title, A.M., Culhane, J.L., Harra, L.K., Doschek, G.A., Golub, L.: 2007, The Hinode (Solar-B) Mission: An Overview. *Sol. Phys.* **243**, 3–17. doi:[10.1007/s11207-007-9014-6](https://doi.org/10.1007/s11207-007-9014-6).
- Kucera, T.A.: 2015, Derivations and Observations of Prominence Bulk Motions and Mass. In: Vial, J.C., Engvold, O. (eds.) *Solar Prominences, Astrophys. Space. Sci. Libr.* **415**, 79–101. doi:[10.1007/978-3-319-10416-4_4](https://doi.org/10.1007/978-3-319-10416-4_4).

- Kuckein, C., Martínez Pillet, V., Centeno, R.: 2012, An Active Region Filament Studied Simultaneously in the Chromosphere and Photosphere. II. Doppler Velocities. *Astron. Astrophys.* **542**, A112. doi:[10.1051/0004-6361/201218887](https://doi.org/10.1051/0004-6361/201218887).
- Kuckein, C., Verma, M., Denker, C.: 2016, Giant Quiescent Solar Filament Observed with High-Resolution Spectroscopy. *Astron. Astrophys.* **589**, A84. doi:[10.1051/0004-6361/201526636](https://doi.org/10.1051/0004-6361/201526636).
- Kuckein, C., Centeno, R., Martínez Pillet, V., Casini, R., Manso Sainz, R., Shimizu, T.: 2009, Magnetic Field Strength of Active Region Filaments. *Astron. Astrophys.* **501**, 1113 – 1121. doi:[10.1051/0004-6361/200911800](https://doi.org/10.1051/0004-6361/200911800).
- Law, N.M., Mackay, C.D., Baldwin, J.E.: 2006, Lucky Imaging: High Angular Resolution Imaging in the Visible from the Ground. *Astron. Astrophys.* **446**, 739 – 745. doi:[10.1051/0004-6361:20053695](https://doi.org/10.1051/0004-6361:20053695).
- Leese, J.A., Novak, C.S., Clark, B.B.: 1971, An Automated Technique for Obtaining Cloud Motion from Geosynchronous Satellite Data Using Cross Correlation. *J. Appl. Meteorol.* **10**, 118 – 132.
- Lemen, J.R., Title, A.M., Akin, P.F. D. J. and Boerner, Chou, C., Drake, J.F., Duncan, D.W., Edwards, C.G., Friedlaender, F.M., Heyman, G.F., Hurlburt, N.E., Katz, N.L., Kushner, G.D., Levay, M., Lindgren, R.W., Mathur, D.P., McFeaters, E.L., Mitchell, S., Rehse, R.A., Schrijver, C.J., Springer, L.A., Stern, R.A., Tarbell, T.D., Wuelser, J.P., Wolfson, C.J., Yanari, C., Bookbinder, J.A., Cheimets, P.N., Caldwell, D., Deluca, E.E., Gates, R., Golub, L., Park, S., Podgorski, W.A., Bush, R.I., Scherrer, P.H., Gumm, M.A., Smith, P., Auken, G., Jerram, P., Pool, P., Soufli, R., Windt, D.L., Beardsley, S., Clapp, M., Lang, J., Waltham, N.: 2012, The Atmospheric Imaging Assembly (AIA) on the Solar Dynamics Observatory (SDO). *Sol. Phys.* **275**, 17 – 40. doi:[10.1007/s11207-011-9776-8](https://doi.org/10.1007/s11207-011-9776-8).
- Lin, Y., Engvold, O.R., Wiik, J.E.: 2003, Counterstreaming in a Large Polar Crown Filament. *Sol. Phys.* **216**, 109 – 120. doi:[10.1023/A:1026150809598](https://doi.org/10.1023/A:1026150809598).
- Lin, Y., Engvold, O., Rouppe van der Voort, L., Wiik, J.E., Berger, T.E.: 2005, Thin Threads of Solar Filaments. *Sol. Phys.* **226**, 239 – 254. doi:[10.1007/s11207-005-6876-3](https://doi.org/10.1007/s11207-005-6876-3).
- Löfdahl, M.G.: 2002, Multi-Frame Blind Deconvolution with Linear Equality Constraints. In: Bones, P.J., Fiddy, M.A., Millane, R.P. (eds.) *Image Reconstruction from Incomplete Data, Proc. SPIE* **4792**, 146 – 155. doi:[10.1117/12.451791](https://doi.org/10.1117/12.451791).
- López Ariste, A., Aulanier, G., Schmieder, B., Sainz Dalda, A.: 2006, First Observation of Bald Patches in a Filament Channel and at a Barb Endpoint. *Astron. Astrophys.* **456**, 725 – 735. doi:[10.1051/0004-6361:20064923](https://doi.org/10.1051/0004-6361:20064923).
- Low, B.C.: 1994, Magnetohydrodynamic Processes in the Solar Corona: Flares, Coronal Mass Ejections, and Magnetic Helicity. *Physics of Plasmas* **1**, 1684 – 1690. doi:[10.1063/1.870671](https://doi.org/10.1063/1.870671).
- Ludwig, R.: 1969, *Methoden der Fehler- und Ausgleichsrechnung*, VEB Deutscher Verlag der Wissenschaften, Berlin, Germany.
- Lugaz, N.: 2015, Eruptive Prominences and their Impact on the Earth and our Life. In: Vial, J.C., Engvold, O. (eds.) *Solar Prominences, Astrophys. Space. Sci. Libr.* **415**, 433 – 453. doi:[10.1007/978-3-319-10416-4_17](https://doi.org/10.1007/978-3-319-10416-4_17).
- Mackay, D.H.: 2015, Formation and Large-Scale Patterns of Filament Channels and Filaments. In: Vial, J.C., Engvold, O. (eds.) *Solar Prominences, Astrophys. Space. Sci. Libr.* **415**, 355 – 380. doi:[10.1007/978-3-319-10416-4_14](https://doi.org/10.1007/978-3-319-10416-4_14).
- Mackay, D.H., Gaizauskas, V., Yeates, A.R.: 2008, Where do Solar Filaments Form? Consequences for Theoretical Models. *Sol. Phys.* **248**, 51 – 65. doi:[10.1007/s11207-008-9127-6](https://doi.org/10.1007/s11207-008-9127-6).
- Mackay, D.H., Karpen, J.T., Ballester, J.L., Schmieder, B., Aulanier, G.: 2010, Physics of Solar Prominences. II. Magnetic Structure and Dynamics. *Space Sci. Rev.* **151**, 333 – 399. doi:[10.1007/s11214-010-9628-0](https://doi.org/10.1007/s11214-010-9628-0).

- Malherbe, J.M.: 1989, The Formation of Solar Prominences. In: Priest, E.R. (ed.) *Dynamics and Structure of Quiescent Solar Prominences*, *Astrophys. Space. Sci. Libr.* **150**, 115 – 141. doi:[10.1007/978-94-009-3077-3_16](https://doi.org/10.1007/978-94-009-3077-3_16).
- Martin, S.F.: 1998a, Conditions for the Formation and Maintenance of Filaments. *Sol. Phys.* **182**, 107 – 137. doi:[10.1023/A:1005026814076](https://doi.org/10.1023/A:1005026814076).
- Martin, S.F.: 1998b, Filament Chirality: A Link Between Fine-Scale and Global Patterns. In: Webb, D.F., Schmieder, B., Rust, D.M. (eds.) *New Perspectives on Solar Prominences*, *ASP Conf. Ser.* **150**, 419 – 429.
- Martin, S.F.: 2015, The Magnetic Field Structure of Prominences from Direct and Indirect Observations. In: Vial, J.C., Engvold, O. (eds.) *Solar Prominences, Astrophysics and Space Science Library* **415**, 205. doi:[10.1007/978-3-319-10416-4_9](https://doi.org/10.1007/978-3-319-10416-4_9).
- Martin, S.F., Panasenco, O., Berger, M.A., Engvold, O., Lin, Y., Pevtsov, A.A., Srivastava, N.: 2012, The Build-Up to Eruptive Solar Events Viewed as the Development of Chiral Systems. In: Rimmele, T.R., Tritschler, A., Wöger, F., Collados Vera, M., Socas-Navarro, H., Schlichenmaier, R., Carlsson, M., Berger, T., Cadavid, A., Gilbert, P.R., Goode, P.R., Knölker, M. (eds.) *Second ATST-EAST Meeting: Magnetic Fields from the Photosphere to the Corona*, *ASP Conf. Ser.* **463**, 157 – 173.
- Martres, M.J., Mein, P., Schmieder, B., Soru-Escout, I.: 1981, Structure and Evolution of Velocities in Quiescent Filaments. *Sol. Phys.* **69**, 301 – 312. doi:[10.1007/BF00149996](https://doi.org/10.1007/BF00149996).
- Mein, P.: 1992, Dynamics of the Solar Atmosphere. In: Sánchez, F., Collados, M., Vázquez, M. (eds.) *Solar Observations: Techniques and Interpretation*, Cambridge University Press, Cambridge, UK, 181 – 246.
- Mein, P., Mein, N.: 1988, Differential Cloud Models for Solar Velocity Field Measurements. *Astron. Astrophys.* **203**, 162 – 169.
- Moore, C.E., Minnaert, M.G.J., Houtgast, J., Rowland, H.A.: 1966, *The Solar Spectrum 2935 Å to 8770 Å: Second Revision of Rowland's Preliminary Table of Solar Spectrum Wavelengths* **61**, National Bureau of Standards, Washington, D.C., USA.
- Mullan, D.: 2001, Extended Atmospheres. In: Murdin, P. (ed.) *Encyclopedia of Astronomy and Astrophysics*. doi:[10.1888/0333750888/1846](https://doi.org/10.1888/0333750888/1846).
- Muller, C.: 2014, The Carrington Solar Flares of 1859: Consequences on Life. *Origins Life Evol. Biosphere* **44**, 185 – 195. doi:[10.1007/s11084-014-9368-3](https://doi.org/10.1007/s11084-014-9368-3).
- Müller, E.: 2000, Fluid Dynamics. In: Murdin, P. (ed.) *Encyclopedia of Astronomy and Astrophysics*. doi:[10.1888/0333750888/2089](https://doi.org/10.1888/0333750888/2089).
- Muller, R.: 2001, Solar Photosphere: Filigree. In: Murdin, P. (ed.) *Encyclopedia of Astronomy and Astrophysics*. doi:[10.1888/0333750888/2254](https://doi.org/10.1888/0333750888/2254).
- Norton, A.J., Cooper, W.A.: 2004, *Observing the Universe: A Guide to Observational Astronomy and Planetary Science*, Cambridge University Press, Cambridge, UK.
- November, L.J., Simon, G.W.: 1988, Precise Proper-Motion Measurement of Solar Granulation. *Astrophys. J.* **333**, 427 – 442. doi:[10.1086/166758](https://doi.org/10.1086/166758).
- Parenti, S.: 2014, Solar Prominences: Observations. *Living Rev. in Sol. Phys.* **11**. doi:[10.12942/lrsp-2014-1](https://doi.org/10.12942/lrsp-2014-1).
- Pesnell, W.D., Thompson, B.J., Chamberlin, P.C.: 2012, The Solar Dynamics Observatory (SDO). *Sol. Phys.* **275**, 3 – 15. doi:[10.1007/s11207-011-9841-3](https://doi.org/10.1007/s11207-011-9841-3).

- Peter, H.: 1996, Superpenumbral Vortices. *Mon. Not. R. Astron. Soc.* **278**, 821–828. doi:[10.1093/mnras/278.3.821](https://doi.org/10.1093/mnras/278.3.821).
- Priest, E.R., van Ballegoijen, A.A., Mackay, D.H.: 1996, A Model for Dextral and Sinistral Prominences. *Astrophys. J.* **460**, 530–543. doi:[10.1086/176990](https://doi.org/10.1086/176990).
- Puschmann, K.G., Denker, C., Kneer, F., Al Erdogan, N., Balthasar, H., Bauer, S.M., Beck, C., Bello González, N., Collados, M., Hahn, T., Hirzberger, J., Hofmann, A., Louis, R.E., Nicklas, H., Okunev, O., Martínez Pillet, V., Popow, E., Seelemann, T., Volkmer, R., Wittmann, A.D., Woche, M.: 2012, The GREGOR Fabry-Pérot Interferometer. *Astron. Nachr.* **333**, 880–893. doi:[10.1002/asna.201211734](https://doi.org/10.1002/asna.201211734).
- Reardon, K.P., Cavallini, F.: 2008, Characterization of Fabry-Pérot Interferometers and Multi-Etalon Transmission Profiles. The IBIS Instrumental Profile. *Astron. Astrophys.* **481**, 897–912. doi:[10.1051/0004-6361:20078473](https://doi.org/10.1051/0004-6361/20078473).
- Rimmele, T.R.: 2004, Recent Advances in Solar Adaptive Optics. In: Bonaccini Calia, D., Ellerbroek, B.L., Ragazzoni, R. (eds.) *Advancements in Adaptive Optics, Society of Photo-Optical Instrumentation Engineers (SPIE) Conference Series* **5490**, 34–46. doi:[10.1117/12.551764](https://doi.org/10.1117/12.551764).
- Rimmele, T.R., Marino, J.: 2011, Solar Adaptive Optics. *Living Rev. in Sol. Phys.* **8**, 2. doi:[10.12942/lrsp-2011-2](https://doi.org/10.12942/lrsp-2011-2).
- Rimmele, T.R., Richards, K., Hegwer, S.L., Ren, D., Fletcher, S., Gregory, S., Didkovsky, L.V., Denker, C.J., Marquette, W., Marino, J., Goode, P.R.: 2003, Solar Adaptive Optics: A Progress Report. In: Wizinowich, P.L., Bonaccini, D. (eds.) *Adaptive Optical System Technologies II, Proc. SPIE* **4839**, 635–646. doi:[10.1117/12.457018](https://doi.org/10.1117/12.457018).
- Rust, D.M., Kumar, A.: 1994, Helical Magnetic Fields in Filaments. *Sol. Phys.* **155**, 69–97. doi:[10.1007/BF00670732](https://doi.org/10.1007/BF00670732).
- Scharmer, G., Löfdahl, M.: 1991, Swedish Solar Telescope - Short Summary of Instrumentation and Observation Techniques. *Adv. Space Res.* **11**, 129–132. doi:[10.1016/0273-1177\(91\)90369-U](https://doi.org/10.1016/0273-1177(91)90369-U).
- Scharr, H.: 2007, Optimal Filters for Extended Optical Flow. In: Jähne, B., Mester, R., Barth, B., Scharr, H. (eds.) *Complex Motion Lecture Notes in Computer Sciences* **3417**, Springer, Berlin, Germany, 14–29. doi:[10.1007/978-3-540-69866-1_2](https://doi.org/10.1007/978-3-540-69866-1_2).
- Schmidt, W., von der Lühe, O., Volkmer, R., Denker, C., Solanki, S.K., Balthasar, H., Bello Gonzalez, N., Berkefeld, T., Collados, M., Fischer, A., Halbgewachs, C., Heidecke, F., Hofmann, A., Kneer, F., Lagg, A., Nicklas, H., Popow, E., Puschmann, K.G., Schmidt, D., Sigwarth, M., Sobotka, M., Soltau, D., Staude, J., Strassmeier, K.G., Waldmann, T.A.: 2012, The 1.5 Meter Solar Telescope GREGOR. *Astron. Nachr.* **333**, 796–809. doi:[10.1002/asna.201211725](https://doi.org/10.1002/asna.201211725).
- Schmieder, B.: 2001, Chromosphere. In: Murdin, P. (ed.) *Encyclopedia of Astronomy and Astrophysics*. doi:[10.1888/0333750888/1993](https://doi.org/10.1888/0333750888/1993).
- Schou, J., Scherrer, P.H., Bush, R.I., Wachter, R., Couvidat, S., Rabello-Soares, M.C., Bogart, R.S., Hoeksema, J.T., Liu, Y., Duvall, T.L., Akin, D.J., Allard, B.A., Miles, J.W., Rairden, R., Shine, R.A., Tarbell, T.D., Title, A.M., Wolfson, C.J., Elmore, D.F., Norton, A.A., Tomczyk, S.: 2012, Design and Ground Calibration of the Helioseismic and Magnetic Imager (HMI) Instrument on the Solar Dynamics Observatory (SDO). *Sol. Phys.* **275**, 229–259. doi:[10.1007/s11207-011-9842-2](https://doi.org/10.1007/s11207-011-9842-2).
- Schüssler, M., Shelyag, S., Berdyugina, S., Vögler, A., Solanki, S.K.: 2003, Why Solar Magnetic Flux Concentrations are Bright in Molecular Bands. *Astrophys. J., Lett.* **597**, L173–L176. doi:[10.1086/379869](https://doi.org/10.1086/379869).
- Seymour, P.A.H.: 1976, The 1919 Solar Eclipse Expedition. *Vistas Astron.* **20**, 207–209. doi:[10.1016/0083-6656\(76\)90036-2](https://doi.org/10.1016/0083-6656(76)90036-2).

- Simon, G.: 2001, Solar Photosphere: Supergranulation. In: Murdin, P. (ed.) *Encyclopedia of Astronomy and Astrophysics*. doi:[10.1888/0333750888/2258](https://doi.org/10.1888/0333750888/2258).
- Socas-Navarro, H.: 2015, *NICOLE: NLTE Stokes Synthesis/Inversion Code*, Astrophys. Source Code Lib..
- Spruit, H.: 2001, Solar Photosphere. In: Murdin, P. (ed.) *Encyclopedia of Astronomy and Astrophysics*. doi:[10.1888/0333750888/2015](https://doi.org/10.1888/0333750888/2015).
- Stein, R.: 2001, Solar Photosphere: Mesogranulation. In: Murdin, P. (ed.) *Encyclopedia of Astronomy and Astrophysics*. doi:[10.1888/0333750888/2014](https://doi.org/10.1888/0333750888/2014).
- Steiner, O., Hauschildt, P.H., Bruls, J.: 2001, Radiative Properties of Magnetic Elements. I. Why are vec G-Band Bright Points Bright? *Astron. Astrophys.* **372**, L13–L16. doi:[10.1051/0004-6361:20010540](https://doi.org/10.1051/0004-6361:20010540).
- Stix, M.: 2004, *The Sun: An Introduction*, Springer, Berlin, Germany.
- Tandberg-Hanssen, E.: 2001, Solar Prominences: Active. In: Murdin, P. (ed.) *Encyclopedia of Astronomy and Astrophysics*. doi:[10.1888/0333750888/2277](https://doi.org/10.1888/0333750888/2277).
- Tang, F.: 1987, Quiescent Prominences – Where are they Formed? *Sol. Phys.* **107**, 233–237. doi:[10.1007/BF00152021](https://doi.org/10.1007/BF00152021).
- Tsuneta, S., Ichimoto, K., Katsukawa, Y., Nagata, S., Otsubo, M., Shimizu, T., Suematsu, Y., Nakagiri, M., Noguchi, M., Tarbell, T., Title, A., Shine, R., Rosenberg, W., Hoffmann, C., Jurcevich, B., Kushner, G., Levay, M., Lites, B., Elmore, D., Matsushita, T., Kawaguchi, N., Saito, H., Mikami, I., Hill, L.D., Owens, J.K.: 2008, The Solar Optical Telescope for the Hinode Mission: An Overview. *Sol. Phys.* **249**, 167–196. doi:[10.1007/s11207-008-9174-z](https://doi.org/10.1007/s11207-008-9174-z).
- Ulrich, R.K.: 1970, The Five-Minute Oscillations on the Solar Surface. *Astrophys. J.* **162**, 993–1002. doi:[10.1086/150731](https://doi.org/10.1086/150731).
- van Ballegooijen, A.A., Martens, P.C.H.: 1989, Formation and Eruption of Solar Prominences. *Astrophys. J.* **343**, 971–984. doi:[10.1086/167766](https://doi.org/10.1086/167766).
- van Noort, M., Rouppe van der Voort, L., Löfdahl, M.G.: 2005, Solar Image Restoration by Use of Multi-Frame Blind De-Convolution with Multiple Objects and Phase Diversity. *Sol. Phys.* **228**, 191–215. doi:[10.1007/s11207-005-5782-z](https://doi.org/10.1007/s11207-005-5782-z).
- Verma, M., Denker, C.: 2011, Horizontal Flow Fields Observed in Hinode G-Band Images. I. Methods. *Astron. Astrophys.* **529**, A153. doi:[10.1051/0004-6361/201016358](https://doi.org/10.1051/0004-6361/201016358).
- Weiss, N.: 2001, Sunspots. In: Murdin, P. (ed.) *Encyclopedia of Astronomy and Astrophysics*. doi:[10.1888/0333750888/2050](https://doi.org/10.1888/0333750888/2050).
- Wells, D.C., Greisen, E.W., Harten, R.H.: 1981, FITS – A Flexible Image Transport System. *Astron. Astrophys. Suppl. Ser.* **44**, 363–370.
- Wiegelmann, T., Sakurai, T.: 2012, Solar Force-Free Magnetic Fields. *Living Rev. Sol. Phys.* **9**. doi:[10.12942/lrsp-2012-5](https://doi.org/10.12942/lrsp-2012-5).
- Zinth, W., Zinth, U.: 2011, *Optik: Lichtstrahlen – Wellen – Photonen*, Oldenbourg Wissenschaftsverlag, München, Germany.
- Zirker, J.B.: 2002, *Journey from the Center of the Sun*, Princeton, New Jersey, USA.
- Zirker, J.B., Engvold, O., Martin, S.F.: 1998, Counter-Streaming Gas Flows in Solar Prominences as Evidence for Vertical Magnetic Fields. *Nature* **396**, 440–441. doi:[10.1038/24798](https://doi.org/10.1038/24798).

Acknowledgments

I would like to express my special appreciation and thanks to my supervisor Prof. Dr. Carsten Denker. Without his support and friendly comments this thesis would not be the same. It was a pleasure to work under his supervision, and I hope to continue the work for many years. Furthermore, I want to thank my co-advisor Prof. Dr. Gottfried Mann.

A special thanks to all the members of the Optical Solar Physics group at AIP. It is a pleasure to work with you. In particular, I would like to thank Dr. Christoph Kuckein for his help and expertise in filaments – many thanks for your comments and suggestions. I would like to thank also Sergio J. González Manrique for many suggestions and help when I got stuck in the data analysis. Many thanks to Ekaterina Dineva for proof-reading the formulas in this thesis and Drs. Meetu Verma and Horst Balthasar for their support and encouragement.

A great thanks to all my friends, who supported me during the Master thesis, in particular to Stuff, Ulli, and Daniel for carefully reading the work. Furthermore, I want to thank my family for their support and their encouragement. Above all I want to thank my boyfriend Marco, who is always at my side, listens to me, cooking for me, and cheering me up when I was frustrated.

The data of this Master thesis was provided by the Dunn Solar Telescope operated by the National Solar Observatory (NSO) within the scope of service mode campaigns. NSO is operated by the Association of Universities for Research in Astronomy, Inc. (AURA), under cooperative agreement with the National Science Foundation. IBIS was constructed by INAF-Arcetri Astrophysical Observatory with contributions from the University of Florence, the University of Rome. ROSA was build by the Astrophysics Research Centre (ARC) of Queen's University in Belfast, UK. Both instruments are operated with support of the NSO. The Solar Dynamics Observatory is developed and launched by NASA. The SDO data are provided by the Joint Science Operations Center – Science Data Processing at Stanford University. This research has made use of NASA's Astrophysics Data System. SolarSoftWare is a public-domain software package for analysis of solar data written in the Interactive Data Language by Harris Geospatial Solutions. Only thanks to the easy access of data and software libraries, a fast analysis was possible in the short time period allotted to a Master thesis.

Appendix A – List of Acronyms

A/D	Analog-to-Digital
ADU	Analog-to-Digital Unit
AIA	Atmospheric Imaging Assembly
AIP	Leibniz-Institut für Astrophysik Potsdam
AO	Adaptive Optic
BB	Broad Band
BS	Beam Splitter
BST	Beam Steering System
CCD	Charge-Coupled Device
CME	Coronal Mass Ejection
CMOS	Complementary Metal-Oxid-Semiconductor
DBR	Diffuse Bipolar Region
DM	Deformable Mirror
DSP	Digital Signal Processor
DST	Dunn Solar Telescope
EBR	External Bipolar Region
EFR	Emerging Flux Region
EUV	Extrem Ultra-Violet
EUVI	Extrem Ultraviolet Imager
EVE	Extreme ultraviolet Variability Experiment
FFT	Fast Fourier Transform
FIRS	Facility Infrared Spectropolarimeter
FITS	Flexible Image Transport System
FOV	Field-of-View
FPI	Fabry-Pérot Interferometer
FS	Field Stop
FSR	Free Spectral Range
FT	Feature Tracking
FTS	Fourier Transform Spectroscopy
FWHM	Full-Width-at-Half-Maximum
GFPI	GREGOR Fabry-Pérot Interferometer
GPS	Global Positioning System
GRIS	GREGOR Infrared Spectrograph
HiFi	High-resolution Fast Imager
HL	Halogen Lamp
HMI	Helioseismic and Magnetic Imager
HOAO	High-order Adaptive Optic
HWHM	Half-width-at-Half-Minimum
IBIS	Interferometric BIdimensional Spectrometer
IBR	Internal Bipolar Region
IDL	Interactive Data Language
I/EBR	Internal/External Bipolar Region

JPEG	Joint Photospheric Experts Group
K	Kelvin
KSC	Kennedy Space Center
LMSAL	Lockheed Martin Solar and Astrophysics Laboratory
LCT	Local Correlation Tracking
LOS	Line-of-Sight
LTE	Local Thermodynamic Equilibrium
LWS	Living with a Star
MFBD	Multi-Frame Blind Deconvolution
MFGS	Median Filter-Gradient Similarity
MHD	Magnetohydrodynamics
MHz	Mega Hertz
MK	Million Kelvin
Mm	Megameter
NASA	National Aeronautics and Space Administration
NB	Narrow Band
NIR	Near-Infrared
NJIT	New Jersey Institute of Technology
NLTE	Non-LTE
NOAA	National Oceanic and Atmospheric Administration
NSO	National Solar Observatory
PI	Principle Investigator
PIL	Polarity-Inversion-Line
PSF	Point Spread Function
ROI	Region-of-Interest
ROSA	Rapid Oscillations in the Solar Atmosphere
RTI	Rayleigh-Taylor instabilities
SDO	Solar Dynamics Observatory
SHWFS	Shack-Hartmann Wavefront Sensor
SoHO	Solar and Heliospheric Observatory
SOT	Solar Optical Telescope
SSD	Sum-of-Squared Differences
SSM	Solar Maximum Mission
SSW	SolarSoft
STEREO	Solar TERrestrial RELations Observatory
SWAP	Sun Watcher using APS detectors and image Processing
TRACE	Transition Region and Coronal Explorer
UBF	Universal Birefringence Filter
USA	United States of America
UT	Universal Time
UV	Ultra-Violet
VTT	Vacuum Tower Telescope
WWW	World Wide Web

Selbstständigkeitserklärung

Hiermit erkläre ich, dass ich diese Arbeit selbständig verfasst und keine anderen als die von mir angegebenen Hilfsmittel und Quellen genutzt habe.

Andrea Diercke

Ort, Datum